CFD Methods in the Atmospheric Roughness Layer at Different Scales

Inauguraldissertation

zur
Erlangung der Würde eines Doktors der Philosophie
vorgelegt der
Philosophisch-Naturwissenschaftlichen Fakultät
der Universität Basel
von

Andres Gartmann
aus Valendas, GR (CH)

Basel, 2012

Genehmigt von der Philosophisch-Naturwissenschaftlichen Fakultät der Universität Basel auf Auftrag von

Prof. Dr. Eberhard Parlow
Institut für Meteorologie, Klimatologie und Fernerkundung
Departement Umweltwissenschaften
Universität Basel
Schweiz
und
Dr. Peter Moonen
Chair of Building Physics
Eidgenössische Technische Hochschule
Zürich
Schweiz

Basel, den 18.10.2011

Prof. Dr. Martin Spiess
Dekan

Namensnennung-Keine kommerzielle Nutzung-Keine Bearbeitung 2.5 Schweiz

---

Sie dürfen:

das Werk vervielfältigen, verbreiten und öffentlich zugänglich machen

Zu den folgenden Bedingungen:

Namensnennung. Sie müssen den Namen des Autors/Rechteinhabers in der von ihm festgelegten Weise nennen (wodurch aber nicht der Eindruck entstehen darf, Sie oder die Nutzung des Werkes durch Sie würden entlohnt).

Keine kommerzielle Nutzung. Dieses Werk darf nicht für kommerzielle Zwecke verwendet werden.

Keine Bearbeitung. Dieses Werk darf nicht bearbeitet oder in anderer Weise verändert werden.

- Im Falle einer Verbreitung müssen Sie anderen die Lizenzbedingungen, unter welche dieses Werk fällt, mitteilen. Am Einfachsten ist es, einen Link auf diese Seite einzubinden.

- Jede der vorgenannten Bedingungen kann aufgehoben werden, sofern Sie die Einwilligung des Rechteinhabers dazu erhalten.
- Diese Lizenz lässt die Urheberpersönlichkeitsrechte unberührt.

Die gesetzlichen Schranken des Urheberrechts bleiben hiervon unberührt.

Die Commons Deed ist eine Zusammenfassung des Lizenzvertrags in allgemeinverständlicher Sprache: http://creativecommons.org/licenses/by-nc-nd/2.5/ch/legalcode.de

Haftungsausschluss:
Die Commons Deed ist kein Lizenzvertrag. Sie ist lediglich ein Referenztext, der den zugrundeliegenden Lizenzvertrag übersichtlich und in allgemeinverständlicher Sprache wiedergibt. Die Deed selbst entfaltet keine juristische Wirkung und erscheint im eigentlichen Lizenzvertrag nicht. Creative Commons ist keine Rechtsanwaltsgesellschaft und leistet keine Rechtsberatung. Die Weitergabe und Verlinkung des Commons Deeds führt zu keinem Mandatsverhältnis.

Quelle: http://creativecommons.org/licenses/by-nc-nd/2.5/ch/ Datum: 3.4.2009

Acknowledgements

First of all I thank Prof. Dr. Eberhard Parlow for the opportunity to conduct this thesis in his team and to let me be a part of the motivating work environment in his institute. Secondly, I thank Dr. Mathias D. Müller for sharing his knowledge, his friendly support and all the exciting discussions in an office probably more turbulent than any known meteorological condition. Furthermore, I thank Dr. Peter Moonen for acting as a co-referee for this thesis.

A special thank dues to Dr. Roland Vogt for his help in the measurement world and guidance. At this point, I thank the entire management team of meteoblue AG, especially Dr. Karl G. Gutbrod for his continuing support.

Further, I would like to thank the current and former members of the Institute of Meteorology, Climatology and Remote Sensing at the University of Basel: Especially Günter Bing, without his computer support and provided resources, the computations would not have been possible, and Josette Pfefferli-Stocky for her administrative support. Also I thank Mathias Ritter, Patrick Koller, Dr. Irene Lehner, Dr. Corinne Frey and Dr. Christian Feigenwinter for many discussions and amicable hours; Dr. Wolfgang Schwanghart and Dr. Wolfang Fister who motivated and supported me for the project in the physio-geographic related research; Dominik Michel and Björn Lietzke who supported my work by providing essential data from their measurement campaigns and important knowledge of their research fields, as well as many entertaining discussions.

I thank Martin Jacquot and Dr. Patrick Vogt of the *Universitätsrechenzentrum* who supported me during the installation and work on the university clusters. The patient endorsement and gained friendship with Patrick Vogt during the intensive calculation work hours were indispensable. Markus Dutly (CADFEM Switzerland) for his support with the licenses and knowledge with the commercial software packages ANSYS.

I would like to express my special gratitude to Malcolm and Elizabeth Page for their valuable help in proof reading the manuscripts. Further, I thank my parents and my brother for their loving support in the last years and encouragement in hectic moments.

However, Rebecca's support and love were essential in many ways and I am committed to greatest thanks to her.

Abstract

The wind-related processes in the atmospheric roughness layer strongly affect our comfort and health and can have a significant influence on our lives, especially in urban areas. The flow patterns are the main drivers of dispersion and transport of pollutants and particles. However, their evolution in the roughness layer is complex because of disturbances introduced by topology or wind flows in the Atmospheric Boundary Layer (ABL). Experimental approaches, such as wind-tunnels can significantly improve the understanding of characteristics and be used for the improvement and validation of model approaches. Nevertheless, they are conducted under ideal conditions and do not represent the complex influences occurring in the atmospheric roughness layer. Field measurements are therefore a very practicable approach to study the chaotic behaviour of environmental flow patterns. The effort required to obtain field measurements and their small spatial significance however make it difficult to obtain large spatial monitoring of the phenomena. In the past, numerical studies often used simplified and idealized geometries or methods to model roughness elements and only few studies were conducted in real environments using field measurements to improve the knowledge of roughness layer flows, especially in urban areas. While the different approaches have frequently been used separately, their combination could lead to significant knowledge and new insights into the complex processes. This thesis introduces the theory and major steps taken to model the relevant roughness elements: sub-grid elements, such as surface texture, vegetation elements, such as trees, and impermeable obstacles, such as buildings. The numerical domains were based on real environments where either field or experimental studies had been conducted providing data with which the numerical methods could be validated, highlighting the advantages of a combined, multidisciplinary approach. The bridge between the engineering derived Computational Fluid Dynamics (CFD) methods and their application in environmental flow case-studies is introduced, as well as methods to model urban areas from a micro to a neighborhood scale. Ways in which to deal with problems, such as meshing complex geometrical data, as well as an alternative approach for obtaining approximate transient results are shown using examples from case studies in different environments. Four case studies, all validated with either experimental wind-tunnel or field measurements were conducted for the relevant roughness elements: sub-grid, porous (e.g. trees) and impermeable (e.g. buildings). The case studies also create a bridge between the engineering dominated CFD methods and today's applications in environmental flows. In each of the case studies, the application of dispersion or transport is studied for gaseous fluids or solid-particle detachment, dispersion and transport. Numerical problems occurring, especially in urban areas, where the topology is complex and heterogeneous, were addressed and the successful solution demonstrated. The implementation used commercial software and OpenFOAM, an open-source code that was found to be an ideal software package for research purposes because of its parallel capabilities and flexibility for future studies.

Contents

I. Introduction 17

Section numbering of published articles not included

List of Figures

Figure numbering of published articles not included

Figure numbering of published articles not included

List of Tables

Table numbering of published articles not included

Acronyms

ABL Atmospheric Boundary Layer
BUBBLE Basel Urban Boundary Layer Experiment
CAD Computer-Aided Design
CFD Computational Fluid Dynamics
CGM Conjugate Gradient Method
DEM Digital Elevation Model
DNS Direct Numerical Simulation
DXF Drawing Exchange Format
FVM Finite Volume Methods
GIS Geographical Information System
LAD Leaf Area Density
LES Large Eddy Simulation
NSE Navier-Stokes Equations
OpenFOAM Open Field Operation and Manipulation
PDE Partial Differential Equations
PISO Pressure Implicit with Splitting of Operators
PM Particulate Matter
RANS Reynolds-Averaged Navier-Stokes
SBL Surface Boundary Layer
SIMPLE Pressure-Linked Equations
TKE Turbulent Kinetic Energy

Part I.
Introduction

1. Preface

The air we breathe belongs to a chaotic and complex fluid system, the atmosphere (Stull, 2000). Most of the time, humans are exposed to the weather on the Earth surface, where interaction between the Atmospheric Boundary Layer (ABL) and the surface occurs. Furthermore, an important part of anthropogenic emissions are released close to the ground (Christen, 2005). The exposure to the different meteorological properties, including wind, temperature and humidity, as well as pollutants, affects life on Earth in many ways. In the few last decades, awareness of the influence of pollutants and particles on health has increased drastically (Grossman and Krueger, 1995; Molina and Molina, 2004). Dispersion characteristics near the Earth surface are mainly influenced by the meteorological conditions, especially by wind patterns (Rotach et al., 2004). Therefore, understanding the wind patterns and their influence on dispersion and transport of secondary flow parts, such as gases and particles, are key areas of research for disciplines including architecture, urban development and planning, agriculture, medicine, as well as related research, such as air quality measurements, wind-engineering, grain storage.

Fluid flowing over a solid wall forms a boundary layer (Wilcox, 2000), leading to the formation of the ABL in the troposphere. The troposphere can be divided in four zones: firstly the laminar layer (few millimeters), and the roughness layer (50-100 m above ground) forming the so-called Surface Boundary Layer (SBL). The two others are the transition layer (extending to about 0.5-1 km above ground) and the free atmosphere (extending to about 11 km above ground) (Rohli and Vega, 2008). We live in the lower region of the SBL and are exposed to the meteorological properties in the lower part of the boundary layer of the atmosphere the roughness layer. The structure of the ABL is controlled by the stability, which has an influence on the evolution of temperature and wind profiles (Stull, 2000). The structure of the roughness layer is however, directly influenced by the roughness elements on the ground. Roughness elements occur in different forms: texture of the ground (grass, cultivated areas) and larger objects, like forests or buildings. The roughness of a surface is generally expressed as the aerodynamic roughness length and can be classified according the Davenport-Wieringa roughness length classification (Stull, 2000) or similar classifications (Oke, 2006). Simple correlations describe the evolving ABL for neutral stabilities as a function of the velocity, the altitude above ground and the aerodynamic length. These correlations, however, reduce the complex flow situations, especially in rough areas to one parameter, the roughness length. On a micro-scale (10-100 m) (Orlanski, 1975) such correlations are not sufficient to capture the complexity of the evolving flow patterns in and around such roughness elements. But dispersion and transport characteristics, as well as measurements in the roughness layer are directly influenced by the complexity of the evolving flow patterns (Yassin et al., 2009).

Therefore, capturing the detail of flow characteristics within the roughness layer is an important step to understanding the mechanisms influencing flow fields in a wide variety of research areas, for example: a) pollutant dispersion in urban areas, which influences our health, b) interpreting point measurements, which enriches the knowledge of intensive field measurements, c) influence of forests on windfarms, which helps to optimize alternative energy resources, d) conceptualization of future cities, especially the comfort in urban areas, e) requirements for windbreaks, which helps to improve protecting of farm land or stock areas, f) influences on soil deposition, helps to optimize agricultural productivity.

There are three types of approaches frequently used to study the flow fields and pollutant or particle concentrations, which will be addressed in this thesis:

Experimental / Laboratory measurements approaches are setup in controlled environments, such as wind-tunnels.

Field measurements Field campaigns are conducted in real environments

Numerical approaches involving different forms of models, from analytical to physically-based

2. State of current research

It is important to define the scale on which the influence of roughness on a flow field is going to be studied (Orlanski, 1975). From a large scale perspective (meso- or synoptic-scale), single or multiple roughness elements, even large objects with dimensions of a few dozen meters and over a wide area (such as a city) will have a minor influence. Such elements can be considered negligible for flows in the free atmosphere or can be simplified using parameters such as the roughness length to estimate the influence on the ABL. On a smaller scale, roughness elements such as buildings, can have a significant influence on the flow patterns. According to Orlanski (1975) the micro-scale involves process from $\approx 0 - 2\,\mathrm{km}$. Britter and Hanna (2003) introduced three spatial scales in urban environments: city scale ($< 10 - 20\,\mathrm{km}$), neighborhood scale ($< 1 - 2\,\mathrm{km}$) and the street canyon scale ($< 100\,\mathrm{m}$). This thesis studies flows in the micro-scale range (Orlanski, 1975), from the street-canyon scale to neighborhood scale in urban contexts (Britter and Hanna, 2003). At this scale, roughness elements forming the canopy scale, are either sub-grid (for example, surface textures such as grass) or fully resolved (for example, trees or buildings). These objects form a sublayer of the roughness layer, the canopy layer (Britter and Hanna, 2003). Three roughness classes are introduced based on their fluid interaction characteristics: *sub-grid* (e.g. crop sort), *impermeable* (e.g. buildings) and *porous* (e.g. trees).

2.1. Experimental approaches

Experimental studies are mainly conducted in wind or water tunnels, whereby the full control makes this approach very practicable to study phenomena under ideal conditions. Wind tunnel studies have been conducted with idealized urban geometries to study urban effects (*impermeable*): pollutant concentrations in simple urban geometries (Davidson et al., 1996; Chang and Meroney, 2003), wind fields in water channels (Princevac et al., 2010) or fluxes (Barlow and Belcher, 2002). Also intensive wind tunnel experiments were conducted with real city geometries (Feddersen, 2005). Castro et al. (2006) studied the influence of the roughness layer in a wind-tunnel that was similar to urban structures to improve *sub-grid* approaches. Others used portable wind-tunnels to obtain in-situ measurements (Fister et al., 2011). Wind channel experiments were also conducted to study the effect of vegetation (*porous*) on wind flows (Grant, 1983). The results from the experimental studies are often used to validate numerical approaches. Nevertheless, the simplification of the objects and the ideal flow conditions are not able to reproduce real situations as they occur in urban areas or around large porous structures, such as forest edges. Macdonald et al. (1998) draw a comparison between wind tunnel and field experiments to bridge the gap between the two.

2.2. Field measurement campaigns

Field measurements provide the possibility to study real environmental flows. The roughness elements are mostly complex and not idealized, and the influences of synoptic phenomena are included. There is a large effort, in terms of both cost and time invested, involved in obtaining good field measurements, but they do provide a unique insight into natural flow characteristics. Many field measurements have been conducted in urban environments (*impermeable*) including one-point measurements (Louka et al., 2000), particle distribution at three locations (Weber and Weber, 2008) and turbulence (Brook, 1972; Rotach, 1995; Feigenwinter, 1999). Other extensive field campaigns are the Joint Urban 2003 study (Leach, 2005) and the BUBBLE (Christen, 2005; Rotach et al., 2005). Grimmond et al. (2002) give an extensive overview of campaigns focusing on CO_2 field measurements. A large field campaign, FLUXNET, studied meteorological properties in vegetation structures (*porous*) (Baldocchi et al., 2001). Other studies focused on the turbulence characteristics in and above forests (Allen, 1968; Raynor, 1971; Green et al., 1995) and behind windbreaks (Finnigan and Bradley, 1983). A review of early studies investigating the influence of roughness elements (*sub-grid*) can be found in Roth (2000).

2.3. Numerical approaches

The history of numerical approaches is long and encompasses a wide range of methods. High resolution and physically-based numerical approaches with simple objects or individual buildings addressing studies for *impermeable* roughness elements (Hunter et al., 1992; Calhoun et al., 2004). A series of studies used simple geometries and different numerical models to simulate pollutant dispersion and transport in urban environments (Sini et al., 1996; Andronopoulos et al., 2002; Tsai and Chen, 2004; Huang et al., 2009; Yassin et al., 2009; Li et al., 2009). Other studies focused on related topics such as the ventilation potential in urban environments (Moonen et al., 2011). Several studies used real and complex geometries, but either were verified with measurements taken from other studies in different backgrounds without validation, or their approaches (Chu et al., 2005; Neifytou et al., 2006; Yang and Shao, 2008) or with experimental wind-tunnel measurements (Carpentieri et al., 2009; Xie and Castro, 2009). In the scale *sub-grid*, there are studies to refine the aerodynamic roughness representation (Grimmond and Oke, 1999) or model approaches (Guilloteau and Mestayer, 2000; Singh et al., 2008). There are high resolution numerical CFD approaches, which were compared to field measurements (Murena et al., 2009; Wang and Zhang, 2009), but most of them are only on street canyon scale by modelling a single street canyon (Vardoulakis et al., 2003).
Only a few studies were conducted in real urban environments and compared to field measurements, whereof Hanna et al. (2006) gives a good overview. There have been many numerical studies verified using wind tunnels for vegetation elements (*porous* roughness elements) (Kobayashi et al., 1994; Packwood, 2000; Liang et al., 2006; Endalew et al., 2009; Yeh et al., 2010). Several studies with porous shelter roughness elements have been verified with field measurements (Hagen et al., 1981; Bradley and Mulhearn, 1983). There are different plain numerical approaches, including Geographical Information System (GIS) (Vigiak et al., 2003) or physically-based approaches (Bourdin and Wilson, 2008; Dalpé and Masson, 2009).

Very important knowledge can be drawn from the different approaches in the past. The experimental systems are an ideal way to validate model approaches because the ideal conditions in the controlled environment are readily transferable to numerical results. But the simplification of the objects in experimental studies, as well as the controlled conditions, cannot represent the complex conditions in the natural roughness layer, whereas field measurements capture the relevant process dynamics in environmental flows. The intensive effort required makes it difficult to realize spatially significant measurements over a larger extent (Christen, 2005). The numerical approaches are directly dependent on experimental and field measurements because the modelled results have no relevance without validation. CFD methods are based on physically-derived governing equations that are able to capture fluid dynamics in every detail (part II). Nevertheless, even with today's computational resources, it is not practicable to resolve every scale. Therefore, applicable models were derived, which enable a physically-based modelling of environmental flows. The combination of field measurements and physical numerical methods, combines the advantages of both approaches: the reality in the field measurement with the spatial resolution of the numerical results.

3. Scope and objectives

Our living environment, the roughness layer, is a layer of the ABL, which is influenced by natural (e.g. vegetation) and anthropogenic (e.g. buildings) roughness elements, which introduce a wide range of flow patterns. Previous research summarized in section 2 has been able to derive a large amount of important knowledge. Nevertheless, the continuing progress in experimental, measurement methods and computational resources as well as an increased ability to combine these, has opened up new possibilities to study the roughness layer. On the one hand, there is a lack of numerical studies with physically-based methods validated with field measurements. On the other hand, the increasing computational resources permit modelling over different scales. Furthermore, the awareness and urgency of the influence of anthropogenic emissions on climate (Charlson et al., 1992) and health (Molina and Molina, 2004) makes it essential to understand the dispersion and transport characteristics of pollutants and particles in the roughness layer. A key factor when studying dispersion and transport in such heterogeneous and complex surroundings, is the understanding and ascertainability of the evolving wind patterns in high spatial and temporal resolution. CFD methods have shown their ability of model flows in the ABL (Kim and Boysan, 1999) and, in combination with field measurements, to present new insights into phenomena that can be found at different scales with high spatial and temporal significance.
This thesis aims to:

i) study the CFD methods to model flow patterns that arise from the three roughness element classes:
    a) *sub-grid*
    b) *impermeable*
    c) *porous*
ii) validate these applications using:
    a) field measurements
    b) experimental measurements
iii) study the dispersion, respectively, transport of two important substances:
    a) gaseous fluids (e.g. CO_2)

    b) solids (e.g. pollen, PM10-particles)

iv) study these phenomena on three scales:
    a) micro-γ (Orlanski, 1975) / street canyon
    b) neighborhood
    c) regional (Britter and Hanna, 2003)

3.1. Structure

The background and theory of CFD methods in environmental flow simulations is discussed in part II. This part is divided into in an introduction (section 4), addressing the application of CFD in environmental flow simulations and arising difficulties, a discussion (section 5) of the fundamentals of CFD, the numerical methods applied and the software packages used and an overview of the methods used to incorporate the different roughness classes in the CFD methods and derived solution for some practicable problems, such as meshing of complex geometries (section 6). The main body of this thesis is then separated into four further parts, each covering a different aspect:

CFD in field experimental study (Part III) This part covers the use of experimental techniques to investigate *sub-grid* roughness (aim ia), iib) and iiib) and ivc)). CFD calculations were conducted for a portable wind-tunnel (Fister et al., 2011). The wind-tunnel was designed to be usable in field campaigns and simulate the ABL with real soil types. The tunnel was equipped with a rainfall simulator and measurement devices to study particle detachment and transport with and without rain. The measurements indicated a good reproduction of the logarithmic wind profile and the numerical results could be used to validate the spatial variations in the boundary layer development over the length of the tunnel. Secondary flow properties, such as turbulence intensity distribution over the tunnel and shear stresses on the ground, which are difficult to measure, were obtained from the model. They were used to model the particle detachment characteristics and compared to the collected data.

CFD with gaseous pollutants (Part IV) This part covers the use of field measurements and modelling to study the effect of *impermeable* roughness elements on the street canyon scale and the dispersion of transported gaseous fluid (aims ib) iia) iiia) and iva)). The evolving flow patterns around a large building were modelled and the numerical results were compared to CO_2 measurements obtained during a field campaign (Vogt et al., 2006). The traffic emissions were modelled and evaluated at different altitude levels near the building wall. A parameter study, which was validated with data of the BUBBLE campaign is described in detail. No measurements for the velocity components were available to validate the flow patterns alone, but the agreement with the CO_2 measurements show their correct representation by the model.

CFD through a tree stand and solid particles (Part V) This part covers the applications of the combined approach to a synthesis with *porous* and *sub-grid* roughness elements. The numerical results were verified with field measurements of the MicroPoem campaign (Michel et al., 2010) and covers the aims ic), iia), iiib) and ivb). The evolving wind patterns in and around a tree stand (windbreak) in southern Switzerland were modelled for different velocity classes. A new turbulence closure model was applied and the dispersion and transport of emitted pollen and the background pollen concentration was simulated using a combination of Eulerian and Lagrangian methods. The CFD methods show a very good accordance and were able to reproduce the complex flows around the stand. The study mixed two roughness classes (*sub-grid* and *porous*) and showed their significant influence on the pollen dispersion. An explanation for measured pollen concentration on the lee-side of the stand could be derived from the highly resolved numerical results.

CFD on a neighborhood scale (Part VI) This part examines the impact of *impermeable* roughness elements on street canyon and neighborhood scale (aims ib), iia) iiia) and ivb)). A 'pseudo-transient' method is introduced to model transient flow patterns over a large spatial extent with a high spatial resolution and affordable computational effort. Traditional transient calculations covering a large spatial extent with a high spatial resolution ($\approx 1\,\mathrm{m}$) and a long time periods are not practicable using today's computer resources (Parra et al., 2010). A clear description of the influence of the spatial distance to boundaries and validation location within the domain was obtained and the practicability to model complete cities was demonstrated.

Finally, in the 'Conclusion and synopsis' (Part VII) conclusions are drawn for the different aspects in this thesis, finishing with an outlook for possible future studies.

Part II.
Method and Theory

This part covers the theoretical background of the numerical approaches and some essential turbulence theory is outlined. An insight is given into the factors, which influence the quality of CFD results, such as assumptions, meshing techniques, software packages, techniques to model *sub-grid*, *impermeable* and *porous* roughness elements and the challenges involved in comparing field data with modelled results (e.g. turbulence scale problematic).

4. CFD in environmental applications

4.1. General considerations

CFD computations in environmental studies are influenced by many different parameters (Fig. 1). Four key considerations distinguish and define the different influencing parameters:

Requirements This topic covers the *spatial resolution* needed to model the desired phenomena in a given *spatial extent*, taking the available *computational resources* into account (section 4.2).

Numerics The numerical CFD method involves several aspects, which can influence the quality of the results to a greater or lesser degree. Challenges are the *quality of the mesh*, the applied *turbulence* models, the *discretization* method or the applied *solvers* and the *governing equations*. These topics are further discussed in section 5.

Meteorology In meteorology, the *range of scales* is wide, from synoptic (e.g. Rossby waves) to small scales (e.g. urban micro-meteorological effects) (Stull, 2000). Meteorological conditions influence many *parameters*, such as temperature, humidity, etc. (Stull, 2000). Due to the complexity, assumptions are needed to be able to model the meteorological conditions. Furthermore, the handling and processing of the *measurement data* to make them comparable to CFD results are not straightforward, especially with regard to the turbulence properties, section 4.4.

Geometry Modelling in the roughness layer, especially *impermeable* elements is greatly facilitated by the availability of geometrical data, such as CAD (or GIS).

A method by which the influence of trees and other vegetation elements on the flow can be modelled, needs to be incorporated into the numerical approach (6).

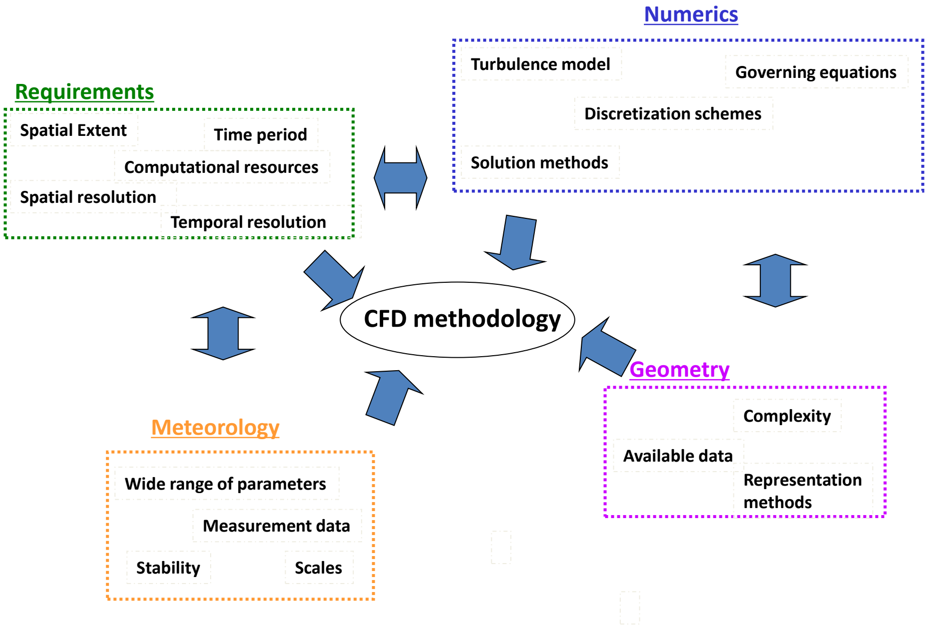

Figure 1: Influencing parameters on CFD calculations in environmental applications

4.2. Scales and resources

This section discusses the needs for the spatial and temporal resolution, taking into account available resources.

4.2.1. Spatial resolution

As introduced in section 2, the street canyon (micro-γ (Orlanski, 1975)) and neighborhood scale range from several meters up to 2 km. To resolve the processes at this scale, a sufficiently high spatial resolution has to be chosen. According to Franke et al. (2004), the resolution is dependent on the application. The intent of this thesis is to resolve the flow pattern in sufficient detail to study the dominating processes. Based on a common quality parameter y^+ (see section 6.1) the spatial resolution ranges from < 1 (near wall in part VI) to 2 m (horizontal resolution in part V) for the case studies.

4.2.2. Temporal resolution

CFD methods distinguish between steady-state and transient calculations: steady-state solutions reflect the mean flow fields, whereas transient calculations resolve temporal fluctuations explicitly. As the representation of the chosen scales (micro-γ / street canyon, neighborhood scale, section 3) with sufficient spatial resolution, the subdivision of the spatial extent can lead to a high number of elements. The combination of a high temporal and a high spatial resolution requires unavailable computational resources (Parra et al., 2010). For the case studies (parts III, IV and V) a steady-state flow field satisfied the needs of the temporal resolution to study the corresponding phenomena. To gain a deeper insight in the processes, especially for urban areas, where very complex flows develop (Li et al., 2006), a new approach is introduced: according to Parra et al. (2010) steady-state solution can be used to create a 'pseudo-transient' solution field. This is obtained by creating a collection (henceforth referred to as *inventory*) of steady-state solutions and then to use a *driver*, e.g. time resolved measurements, to drive the inventory. This means to tie together steady-state solutions to obtain a 'pseudo-transient' flow field. This technique is already widely applied in wind-engineering applications to estimate the potential of wind resources with numerical methods.

4.2.3. Computational resources

The University of Basel cluster *maia* could be used with $>$ 1000 cores (since 2011) and 2 workstations with (24GB and 48GB RAM), especially for pre-processing and simpler calculations. The employed software packages (section 5.5.2) required approximately a relation of 2 KB/element for pre-processing and $1-1.3$ KB/element for calculation. Therefore, meshes up to $20 \cdot 10^6$ elements were feasible, restricted by the pre-processing step and the software.

4.3. Stability and incompressibility

Two assumptions were set for the numerical approaches: neutral conditions for stability and incompressibility of the flows.

4.3.1. Stability

The static stability is one method to study the ability of air parcels to rise. Static stability only considers buoyancy effects, whereas the dynamic stability takes the influence of shear forces in the mean wind into account. The static stability distinguishes between, (Stull, 2000):

1. unstable: The buoyancy force on a displaced air parcel is in the same direction as the displacement

2. neutral: An air parcel displacement does not feel the influence of the buoyant force
3. stable: Temperature gradient is sub-adiabatic and the buoyancy force is opposite the displacement force

Assuming neutral conditions allows to neglect buoyancy effects, and makes it unnecessary to model the thermal effects in the roughness layer.
In addition, the free and forced convection need to be defined (Incropera and Witt, 2002). Free convection describes the flow motion occurring from density differences in a fluid, which results from different temperatures in the fluid and therefore are driven by buoyancy forces (e.g. hot building walls enclosed by cooler air resulting in fluid motion). Forced convection describes the situation, when the flow is not driven by temperature differences. Therefore, the motions on the studied scales (differing significantly on synoptic scale, e.g. cold fronts) convection caused by free convection are neglectable in advection driven flows.
For all case studies, neutral conditions were assumed and thermal effects as well as the influence of the buoyancy force were neglected. These assumptions are valid, based on published results on neutral stabilities in urban areas (Lundquist and Chan, 2006). The results from the study described in part V also show the validity of this assumption for flows around similar roughness elements, such as trees in advection dominated flows.

4.3.2. Thermal effects

To test the performance of CFD methods to represent thermal effects in the atmosphere, a hot and a cold bubble were simulated in a neutral stratified atmosphere and compared to the evolution according to Janjic et al. (2001). The software used in the simulations is described in section 5.5.1.

In a two dimensional simulation, the evolution of a hot bubble, respectively a disturbance near the ground in a neutrally stratified atmosphere over a horizontal distance of 20 km and vertical extent of 13.5 km was modelled (Janjic et al., 2001). The bubble was initialized according to:

$$T(x,z) = \bar{T} + 6.6cos^2\left[\frac{\pi}{2}\sqrt{\left(\frac{x-2750}{2500}\right)^2 + \left(\frac{z-2750}{2500}\right)^2}\right] \tag{1}$$

Figure 2 shows the evolution of the bubble from 0 s to 550 s. The characteristic rise of the bubble in the atmosphere is obtained. The upstreaming air pulls in colder air from the atmosphere and a mushroom-shaped temperature distribution can be observed. The corresponding movie is attached to this thesis in part VIII.

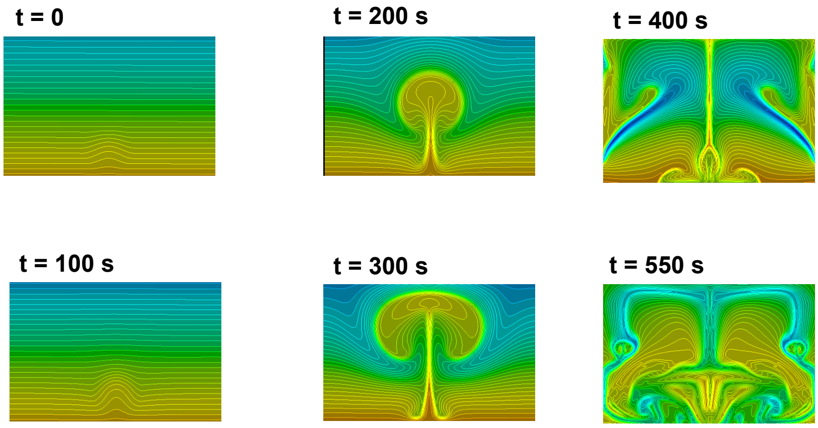

Figure 2: Transient 2D calculation of a warm bubble in a stratified atmosphere with a potential temperature of 300 K

In contrast, the *cold bubble test* was performed over a simulated horizontal extent of 40 km and a vertical extent of 10 km. A cold bubble was initialized according to:

$$T(x,z) = \bar{T} + 15cos^2\left[\frac{\pi}{2}\sqrt{\left(\frac{x-3000}{4000}\right)^2 + \left(\frac{z-3000}{2000}\right)^2}\right] \tag{2}$$

if

$$\sqrt{\left(\frac{x-3000}{4000}\right)^2 + \left(\frac{z-3000}{2000}\right)^2} \leqslant 1 \tag{3}$$

Figure 3 shows the evolution up to 950 s simulation time. The bubble pulls colder air down from the upper region of the simulation area. The strong disturbance after 400 s originates from the defined periodic boundary conditions, from $\gtrsim$ 400 s onwards.

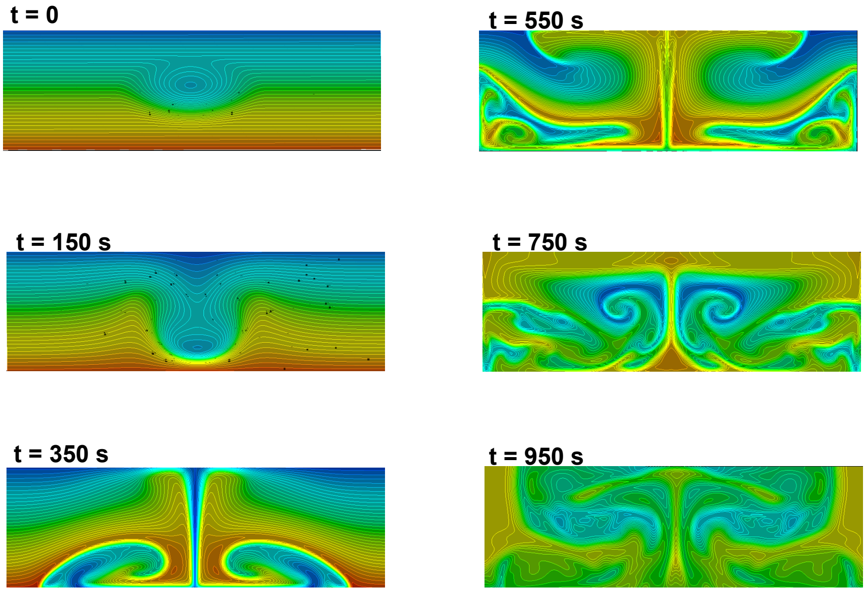

Figure 3: Transient 2D calculation of a cold bubble in a stratified atmosphere with a potential temperature of 300 K

The comparison to the temperature distribution given by Janjic et al. (2001) shows the feasibility of modelling thermal atmospheric processes by using CFD methods. But for many reasons, e.g. microphysics (clouds, precipitation), physical parametrization (soil, clouds, radiation), dynamics (large scale, conservation of enstrophy), the CFD methods introduced here are not practicable in any way to model meso-scale atmospheric processes.

4.3.3. Incompressibility

In fluid mechanics, incompressible flows are summarized as flows with very low Mach numbers $Ma < 0.3$, where the Mach number Ma expresses the ratio between the flow speed and the sound speed, (Wilcox, 2000). The description incompressible describes the flow and not directly the fluid property. Most likely no flows with Mach numbers > 0.3 occur in the roughness layer. Therefore, the assumption of incompressible flows is acceptable.

4.4. Measurement validations

The comparison of time-averaged CFD results with time-series of point-wise field measurements makes it necessary to define a average time-period for the Reynolds Decomposition (eq. 15 in section 5). In field measurements the average time-period is defined to capture the relevant flow scales (Voronovich and Kiely, 2007). To define an appropriate average time-period to compare with the modelled results, the 20 Hz data from the BUBBLE campaign at the 'Sperrstrasse' location were analysed. The Reynolds Decomposition is only applicable for stationary flows (Foken and Wichura, 1996). The statistics of statistical stationary flows are invariant to a time-shift (Pope, 2000). The data were filtered to select only stationary situations, according to:

$$\Delta\left\{\sigma_x^2(t_1....t_n)\right\} = \frac{\sigma_x^2}{\frac{1}{n}\left[\sigma_x^2(t_1) + ... + \sigma_x^2(t_n)\right]} \tag{4}$$

where σ_x is the dispersion of a variable under a time-shift in a full time series $(t_1 \cdot\cdot\cdot\cdot\cdot t_n)$. Stationarity is fulfilled if $\Delta\sigma_x \rightarrow 0$. Therefore, a small trigger value for the filter of $\Delta\sigma_x < 0.04$ was chosen. The raw 20 Hz data were first decomposed by the Reynolds decomposition (see section 5.3). Secondly a filter for the flow angle was applied (e.g. 130°). Figure 4 shows the correlation between the mean velocity and the TKE for wind angle 130° and a long (1200 s) and a short (30 s) time-period for filtered (stationarity) and not filtered data.

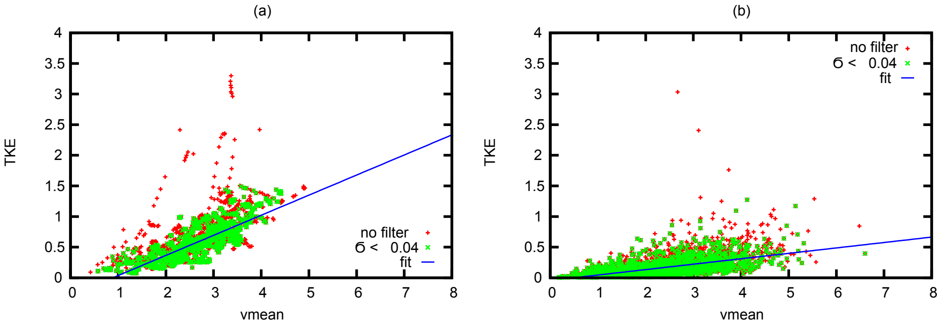

Figure 4: Correlation of the mean velocity to the TKE for $\triangle t = 1200$ s (a) and $\triangle t = 30$ s (b). The statistical analysis was carried out at the highest measurement point in a street canyon, 31.7 m above ground.

A dependency of the TKE (for more details on TKE see subsection 5.3.1)on the mean velocity properties was found in connection with the average time-periods length, thereby introducing some implications for comparing field measurement data and numerical CFD data. The results are outlined in part IV and part VIII.

4.5. Postprocessing - The ability of visualization

CFD results can represent a flow field with a high spatial resolution and therefore, with highly resolved process characteristics. The flow can be visualized, for example using stream-lines, vector plots, contour lines or similar visualization methods.

The three dimensional visualization is primarily of use as a qualitative method as it can show uniquely the complexity of flow patterns, as shown in Fig. 5.

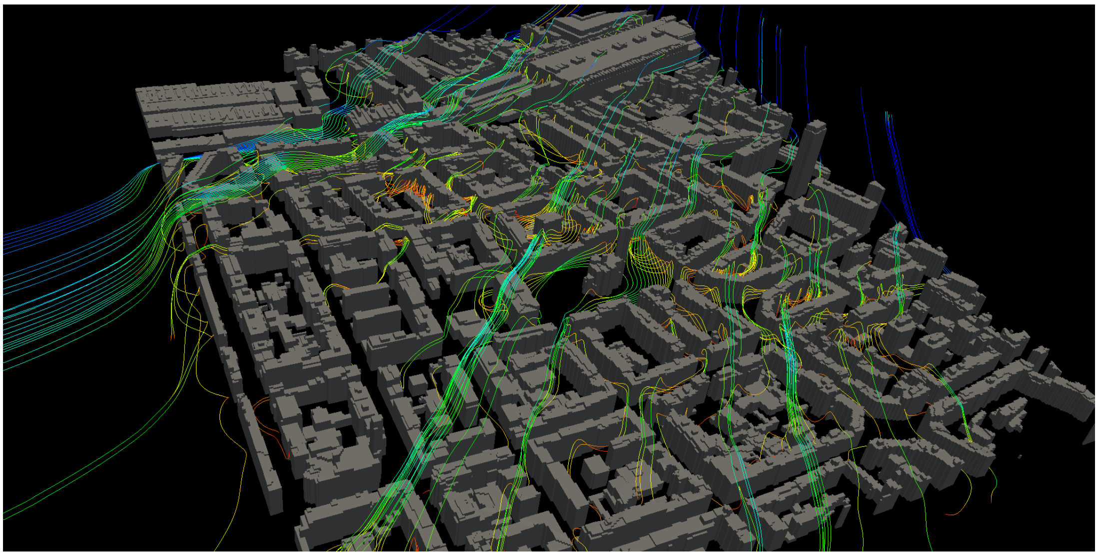

Figure 5: Streamlines during Se wind over a part of 'Klein-Basel', a city block of Basel, Switzerland. Colors indicate velocity (slow: red, high: green)

The three dimensional flow behaviour can be expressed as a combination of two variables: velocity as arrows and TKE as contours, Fig. 6(a) and Fig. 6(b). This allows an easier interpretation of the phenomena and the derivation of such numerical result fields with high spatial resolution is one advantage of CFD methods. Part IV illustrates how the interpretation of numerical flow fields can provide an important qualitative insight into real-situation flow dynamics, although the graphical representation alone lacks quantitative significance.

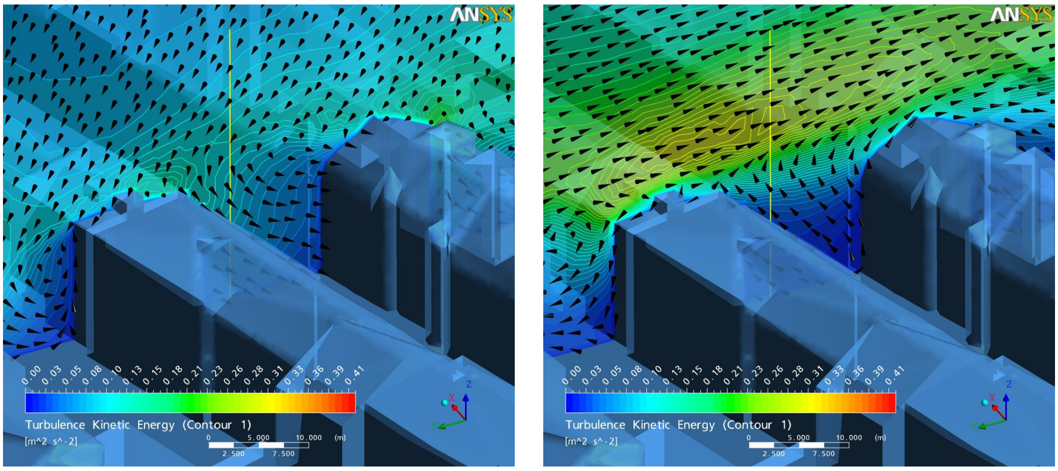

(a) 130° Mean velocity (arrows) and TKE (contour lines)

(b) 355° Mean velocity (arrows) and TKE (contour lines)

Figure 6: Flow patterns within street canyon for two inflow conditions (130° and 355°) illustrated with arrows and contour lines at 'Sperrstrasse' Basel Urban Boundary Layer Experiment (BUBBLE)

5. CFD Theory

As environmental flows are turbulent flows, the characteristics and phenomena of turbulent flows and their research history are briefly introduced in the next section, the fundamentals of the CFD method are discussed as well.

5.1. General view on turbulent flow phenomena

Starting with Leonardo da Vinci's "la turbolenza" (Richter, 2005), followed by 500 years of intensive research and support by increasing computational 'help', the complexity and chaotic behaviour of turbulent flow is still a research topic itself (Ecke, 2005). Turbulent flows can be found everywhere in our daily life (Pope, 2000) and can be described as flow with irregular and chaotic spatial and temporal fluctuations (Ecke, 2005). Turbulent flows have some important characteristics; they have a greater ability to transport and mix fluids than stratified (laminar) flows (Pope, 2000). In the last few centuries, major observations have been made and progress was achieved, such as the Euler equation of motion and the Navier-Stokes Equations (NSE) describing momentum conservation in fluid, including viscosity effects, which fulfill Newton's law of motion. The NSE, a set of 'simple' Partial Differential Equations (PDE), are able to describe every type of flow over all scales (Pope, 2000). Nevertheless, sensitivity to smallest changes in initial or flow conditions makes turbulent flow very difficult to capture. Interestingly, two statements of da Vinci are still state-of-the-art: the separation of the flow into a mean part and a fluctuating part (known as the Reynolds Decomposition) and the description of 'eddies' as elements in turbulence phenomena (Ecke, 2005). Richardson's energy cascade (Richardson, 1922) introduced the concept of transport energy from larger scales (or eddies), where the energy is introduced, to smaller scales, where viscous effects dissipate the energy. In 1941 Kolmogorov formulated a hypothesis about the relation between velocity and timescales to the length of an eddy. Together, Richardson's image of the energy cascade and Kolmogorov's hypothesis led to the derivation of the subdivision of the eddy length scales into an energy-containing range, inertial subrange and a dissipation range. Kolmogorov's hypothesis further deduced a transfer rate of energy, independent of the eddy length, in the inertial subrange and probably one of the most important consequences, a smallest scale of turbulence, the Kolmogorov scales (Pope, 2000), which characterize a definite scale for every turbulent flow. The wide range of scales and the sensitivity to small perturbations makes the numerical study of turbulent flows difficult.

5.1.1. Numerical approach to turbulence

There is a difference between turbulent flow simulations and turbulence models (Pope, 2000): simulations solve the governing equations (NSE) to compute the time-dependent velocity field for one realization of the turbulent flow. In contrast, turbulence models solve the equations for mean properties (Pope, 2000). Frequently applied approaches to turbulent flow simulations are a) Direct Numerical Simulation (DNS), where all scales of the fluid motion are resolved (including the Kolmogorov scales) and b) the Large Eddy Simulation (LES), where the scales for a filtered velocity field are solved according to the NSE, but small scales (dependent on the filter definition) are modelled using a turbulence model approach such as Reynolds-Averaged Navier-Stokes (RANS), where all turbulent length scales are modelled. DNS calculations are not feasible for environmental applications, because all scales have to be represented (from meso-scale motions to the Kolmogorov scale). LES have found an increasing use in environmental applications (Moonen et al., 2011). They show some advantages over RANS turbulence model approaches, but are associated with a considerably higher computational effort (Coirier et al., 2005; Salim et al., 2011). Turbulence models are mostly based on the RANS approach, which apply the Reynolds Decomposition to the governing equations (NSE).
Therefore, RANS models are still the most widely used methods, providing a good compromises between computational costs and accuracy.

5.2. Governing equations

CFD simulations are based on discretization and solution of the Navier-Stokes-Equations (NSE). The NSE describe the physics of liquids and gases in motion and are thus commonly applied to problems such as open channel flow, ocean currents and atmospheric wind. The NSE are based on Newton's law of motion that describes momentum conservation on an infinitesimal fluid element and are written as

$$\rho \cdot \frac{DU_i}{Dt} = \rho \cdot f_i + \frac{\partial \tau_{ij}}{\partial x_j} \tag{5}$$

where U_i are the velocity components in three dimensions, f_i the components of the body force per unit mass, ρ the density of the fluid and τ_{ij} the surface force per unit volume of the infinitesimal element. Equation (5) is often referred to as Cauchy's equation of motion (Kundu and Cohen, 2002). The stress in static fluids is isotropic, which means it is independent of the orientation. If a fluid is in motion, an additional stress is generated by the viscosity of the fluid such that the surface force in a fluid can be expressed as

$$\tau_{ij} = -p\delta_{ij} + \sigma_{ij} \tag{6}$$

where δ_{ij} refers to the Kronecker delta and p is the thermodynamic pressure. If the term $\sigma_{ij} = 0$, equation (6) represents the stress in a static fluid and reduces to the pressure $-p\delta_{ij}$. The deviatoric stress tensor σ_{ij} is the force generated by the viscosity effects in a moving fluid. The gradient of the velocity consists of a symmetric and an antisymmetric part. Because the antisymmetric part expresses the deformation by rotation of the fluid, the viscous stresses can only be generated by the symmetric component, i.e. the strain rate tensor e_{ij}.

$$e_{ij} = \frac{1}{2}\left(\frac{\partial U_i}{\partial x_j} + \frac{\partial U_j}{\partial x_i}\right) \tag{7}$$

For an isotropic medium with a symmetric stress tensor, it can be shown, that

$$\sigma_{ij} = 2\mu_{th} e_{ij} + \lambda e_{mm} \delta_{ij} \tag{8}$$

where μ_{th} and λ are variables expressing the local thermodynamic state (Kundu and Cohen, 2002). Inserting equation (8) into equation (6), the stress tensor equation (9) is formulated as

$$\tau_{ij} = -p\delta_{ij} + 2\mu_{th} e_{ij} + \lambda e_{mm} \delta_{ij} \tag{9}$$

By building an equation for the trace of the stress tensor and expressing $e_{mm} = \frac{\partial U_i}{\partial x_i}$, the following relation can be derived:

$$p = \bar{p} + \left(\frac{2}{3}\mu_{th} + \lambda\right) \cdot \frac{\partial U_i}{\partial x_i} \tag{10}$$

using $\bar{p} = -\frac{1}{3}\tau_{ii}$. With Stokes assumption $\lambda + \frac{2}{3}\mu_{th} = 0$, (Kundu and Cohen, 2002), we obtain the stress tensor equation

$$\tau_{ij} = -\left(p + \frac{2}{3}\mu_{th}\frac{\partial U_i}{\partial x_i}\right)\delta_{ij} + 2\mu_{th}e_{ij} \tag{11}$$

Substituting the stress tensor (eq. 11) in the momentum conservation equation (eq. 5), the NSE for a compressible fluid can be derived

$$\frac{DU_i}{Dt} = -\frac{1}{\rho}\frac{\partial p}{\partial x_i} + f_i + \frac{\partial}{\partial x_j}\left[2\mu_{th}e_{ij} - \frac{2}{3}\mu_{th}\left(\frac{\partial U_i}{\partial x_i}\right)\delta_{ij}\right]\frac{1}{\rho} \tag{12}$$

Fluids with stress rates linearly proportional to the strain rate are called Newtonian fluids. The viscosity μ is the constant of the proportionality, with $\mu = f(T) \sim \mu_{th}$. The continuity equation for incompressible fluids reads:

$$\frac{\partial U_i}{\partial x_i} = 0 \tag{13}$$

Using the strain rate tensor (eq. 7) and the incompressible continuity equation (eq. 13), the NSE for an isostropic, incompressible, Newtonian fluid reduce to

$$\frac{DU_i}{Dt} = -\frac{1}{\rho}\frac{\partial p}{\partial x_i} + f_i + \nu\frac{\partial^2 U_i}{\partial x_i^2} \tag{14}$$

where $\nu = \frac{\mu}{\rho}$ is the kinematic viscosity.

5.3. Turbulence modelling

One of the most common approaches to model turbulence is obtained by applying the Reynolds Decomposition (eq. 15) to the NSE (eq. 14)

$$U_i = \langle U_i \rangle + u_i \tag{15}$$

which leads to the RANS equations.

$$\frac{\bar{D}\langle U_i \rangle}{\bar{D}t} = -\frac{1}{\rho}\frac{\partial \langle p \rangle}{\partial x_i} + f_i + \nu\frac{\partial^2 \langle U_i \rangle}{\partial x_i^2} - \frac{\partial \langle u_i u_j \rangle}{\partial x_j} \tag{16}$$

The additional terms $\frac{\partial\langle u_i u_j\rangle}{\partial x_j}$ are called the Reynolds stresses and play a crucial role in turbulence modelling by using the RANS method. The mean velocity field is governed by four independent equations in three dimensions (eq. (13) and (eq. 14)). $\langle U_i\rangle$, $\langle p\rangle$ and the Reynolds stresses constitute more than four unknown variables, thus the set of equations cannot determine all of the unknown variables, i.e. an "unclosed" situation. The Reynolds stresses have to be defined in a separate exercise to solve the so called "closure problem". The additional equations are called 'turbulence models' and are divided into models using the turbulent viscosity hypothesis and models using Reynolds stress transport equations (Pope, 2000). A common family of turbulent viscosity models are two-equation models.

5.3.1. Turbulence closure: Two-equation eddy-viscosity models

A detailed review of different two-equation eddy-viscosity models is given in Menter (1994).
The turbulent kinetic energy (TKE) is defined as (Wilcox, 2000):

$$k = \frac{1}{2}\langle u_i u_i\rangle \tag{17}$$

The anisotropic stresses are defined as the shear stresses minus the isotropic stresses $\frac{2}{3}k\delta_{ij}$:

$$as_{ij} = \langle u_i u_j\rangle - \frac{2}{3}k\delta_{ij} \tag{18}$$

For the momentum transport only the anisotropic components as_{ij} are relevant and the isotropic part can be expressed by a modified mean pressure (Wilcox, 2000). In 1977, Boussinesq introduced the hypothesis that, in analogy to the stress-rate-of-strain of Newtonian fluids, the shear Reynolds stresses can be assumed to be proportional to the mean rate of strain (Versteeg and Malalasekera, 2007). The relation between the Reynolds stresses and the mean rate of strain is defined by a scalar coefficient, the turbulent viscosity ν_t.

$$\langle u_i u_j\rangle = \frac{2}{3}k\delta_{ij} - \nu_t\left(\frac{\partial\langle U_i\rangle}{\partial\langle x_j\rangle} + \frac{\partial\langle U_j\rangle}{\partial\langle x_i\rangle}\right) \tag{19}$$

It has be to mentioned that this approach assumes an isotropic behavior for the normal Reynolds stresses.

In the widely applied two-equation model, the standard $k-\epsilon$ model (Launder and Spalding, 1974), the turbulent viscosity ν_t is obtained by:

$$\nu_t = C_\mu \frac{k^2}{\epsilon} \tag{20}$$

where $C_\mu = 0.09$ is a model constant (Wilcox, 2000). In the standard $k - \epsilon$ model, two transport equations in addition to the continuity equation (eq. 13) and the RANS (eq. 16) are solved for the TKE k and the dissipation ϵ. Equation 21 shows the transport equation for the TKE:

$$\frac{\bar{D}\langle k \rangle}{\bar{D}t} = \frac{\partial}{\partial x_i}(\frac{\nu_t}{\sigma_k}\frac{\partial k}{\partial x_i}) + \mathcal{P} - \epsilon + S_k \tag{21}$$

and for the standard $k - \epsilon$ model ϵ is calculated according to:

$$\frac{\bar{D}\langle \epsilon \rangle}{\bar{D}t} = \frac{\partial}{\partial x_i}(\frac{\nu_t}{\sigma_\epsilon}\frac{\partial k}{\partial x_i}) + C_{\epsilon 1}\mathcal{P}\frac{\epsilon}{k} - C_{\epsilon 2}\frac{\epsilon^2}{k} + S_\epsilon \tag{22}$$

where σ_k and σ_ϵ are the turbulent Prandlt numbers, relating the diffusivity of k and ϵ to the turbulent viscosity ν_t according to the gradient-diffusion hypothesis (Wilcox, 2000). The gradient-diffusion hypothesis relates the flux of a scalar to the mean scalar gradient. $C_{\epsilon 1} = 1.44$ and $C_{\epsilon 2} = 1.92$ are model constants and S_k and S_ϵ source terms (section 6.2). Neglecting buoyancy effects, the TKE production is $\mathcal{P} = \nu_t 2 S_{ij}^2$, where S_{ij} is the shear stress.

5.4. Numerical Methods

Advective terms, such as $\langle U_j \rangle \frac{\partial^2 \langle U_i \rangle}{\partial x_j}$ in the NSE (eq. 16) contain non-linear quantities and are intricately coupled (Versteeg and Malalasekera, 2007). To solve the NSE, the velocity field has to be known and so the pressure has to be resolved. There is no transport equation for the pressure term p. In compressible cases, the pressure term is derived from density and temperature of the fluid. In the incompressible case, the density is constant and the velocity field should satisfy the incompressible continuity equation (eq. 13) if the pressure field is known.

5.4.1. Pressure coupling

The missing connection between the pressure and the density in incompressible flows poses a problem for computing the pressure (Versteeg and Malalasekera, 2007). Therefore, the correct pressure field in the momentum equations (eq. 16) must fulfill the continuity equations (eq. 13). The Semi-Implicit Method for Pressure-Linked Equations (SIMPLE) is a widely used iterative approach for solving steady-state calculations. SIMPLE creates a link between the velocity and the pressure (Kundu and Cohen, 2002). Assuming the pressure is discretized at the same nodes, a strongly non-uniform pressure field gives rise to a uniform field in the NSE (Versteeg and Malalasekera, 2007). This non-physical artifact can be overcome by creating a staggered grid, and the calculation of the pressure at the nodes and the velocity at the midpoints of the mesh (Harlow and Welch, 1965). The iterative SIMPLE approach starts with a estimated initial pressure field p^* and uses the momentum equations to calculate a velocity set U_i^*. The difference between the pressure p and the estimated initial pressure p^* is denoted as $p\prime$ and, similarly, the difference between the velocity components is U_i'. The correction of the velocity components U_i' can be calculated using p' by neglecting the influence of the neighboring nodes, which is one of the main approximations in the SIMPLE approach (Versteeg and Malalasekera, 2007; Kundu and Cohen, 2002).

$$U_i' = -\frac{1}{A_p}\frac{\partial p'}{\partial x_i} \tag{23}$$

where A_p depends, among others, on the mesh topology discretization. These new velocity components U_i' can be inserted into the continuity equation (eq. 13), giving rise to a Poisson equation.

$$-\frac{1}{A_p}\left(\frac{\partial^2 p'}{\partial x_i^2}\right) = \frac{\partial U_i^*}{\partial x_i} \tag{24}$$

The obtained p' were used to calculate the pressure p and the velocity field U_i by iteration. As the iterative process might lead to divergence, an under-relaxation factor α_{relax} has to be applied using equation 25 (Versteeg and Malalasekera, 2007), where α_{relax} mostly range from 0.3-0.8.

$$p_{new} = p^* + \alpha_{relax} p' \tag{25}$$

Originally designed for transient calculations, the Pressure Implicit with Splitting of Operators (PISO) approach can also be applied to steady flow calculations (Issa, 1985). The PISO approach contains one further step using the p' of the SIMPLE approach.

5.4.2. Discretization

The NSE (eq. 14) are a PDEs. To solve the PDEs for a computational domain, the domain is split into finite cells and the PDE is discretized on the mesh vertices. The creation of meshes is described in detail in section 6.2.2. Discretization is the transformation of the PDE into a set of algebraic equations. One method to discretize the PDE on the domain is the Finite Volume Methods (FVM) (Versteeg and Malalasekera, 2007). By integrating the terms of equation (eq. 14) over a cell volume Ω, the PDE can be expressed in integral form as:

$$\int_{\Omega} \frac{\partial U_i}{\partial t} \cdot d\Omega + \int_{\Omega} U_j \frac{\partial^2 U_i}{\partial x_j^2} \cdot d\Omega = \frac{1}{\rho} \int_{\Omega} \frac{\partial p}{\partial x_i} \cdot d\Omega - \nu \int_{\Omega} \frac{\partial^2 U_i}{\partial x_i^2} \cdot d\Omega \tag{26}$$

By applying Gauss's theorem to convert the volume integrals to surface integrals

$$\int_{\Omega} \left(\frac{\partial}{\partial x_i} \mathbf{F} \right) \cdot d\Omega = \int_{S} \mathbf{F} \cdot \mathbf{n} dS \tag{27}$$

one can rewrite the terms of the NSE (eq. 26). In the FVM, the surface integrals can approximated by the summation of a flux terms over the cell surfaces:

$$\int_{S} (\mathbf{F} \cdot \mathbf{n}) \cdot dS \cong \sum \mathbf{F} \cdot \mathbf{S} \tag{28}$$

where $\mathbf{F}$ is any tensor field and $\mathbf{n}$ the normal vector on the surface $\mathbf{S}$. The surface integrals, respectively the summation of the flux terms over the cell bounds, can be linearized by different schemes, e.g. central or upwind schemes, (Versteeg and Malalasekera, 2007). The discretization of the PDE in the complete domain leads to a set of linearized equations. These equations can be solved using one of many iterative methods. A widely applied iterative solver in modern CFD codes is the Conjugate Gradient Method (CGM). A good introduction can be found in Hestenes and Stiefel (1952) or Weller et al. (1998).

5.4.3. Boundary conditions

In order to solve a PDE, boundary conditions and initial conditions have to be specified. Boundary conditions characterize the flow behavior at the domain boundaries. Two types of basic boundary conditions exist, from which different commonly applied conditions are derived (Versteeg and Malalasekera, 2007; OpenFOAM, 2009): Dirichlet and Neumann. While Dirichlet conditions set the value of a dependent variable to a fixed value, Neumann conditions prescribe a gradient of the variable. Initial conditions specify the flow conditions at the simulation time $t_0 = 0$.

Boundary conditions for solid bounds for the fluid are Dirichlet conditions. In the near wall region, phenomena different to the free flow conditions can be found e.g. for a wall normal to x_2: 1) lower Reynolds numbers, 2) higher shear stresses, 3) $\langle u_2^2 \rangle$ turbulence varies with x_2^4, $\langle u_1^2 \rangle$ and $\langle u_3^2 \rangle$ vary with x_2^2 and 4) the impermeability condition $U_2 = 0$ affects the flow up to the integral scale from the wall (Pope, 2000), where the indices $x_1 - x_3$ denote the direction in the three-dimensional cartesian coordinate system. This subject is discussed in detail in section 6.1.

The typical inlet boundary conditions for simulation the ABL are introduced by Richards and Hoxey (1993) and discussed in Tominaga et al. (2008). The logarithmic inlet profile is specified according to:

$$U(z) = \frac{U^*_{fric}}{\kappa} \cdot \ln(\frac{z + z_0}{z}) \tag{29}$$

where the friction velocity U^*_{fric} is calculated as:

$$U^*_{fric} = \frac{\kappa \cdot U_h}{\ln(\frac{h+z_0}{z})} \tag{30}$$

The reference mean velocity U_h is the velocity at a reference altitude over ground h, z the vertical distance, z_0 is the roughness length and κ the von Kármán constant.
As shown in part IV, there are two widely applied approaches for the specification for the turbulent inlet conditions as suggested by Richards and Hoxey (1993), a constant TKE value k is derived from the friction velocity:

$$k = \frac{U^{*2}_{fric}}{\sqrt{C_\mu}} \tag{31}$$

where C_μ is the model constant for the k- ϵ model ($C_\mu = 0.09$) and the dissipation ϵ is computed as:

$$\epsilon = \frac{U^{*2}_{fric}}{\kappa \cdot (z + z_0)} \tag{32}$$

The second approach widely applied in engineering problems relates k to the turbulence intensity I and the mean velocity U:

$$k = \frac{3}{2} \cdot U^2(z) \cdot I^2 \tag{33}$$

and employs a constant dissipation:

$$\epsilon = \frac{k^{\frac{3}{2}}}{L_t} \tag{34}$$

where L_t is a characteristic length scale. Following Pope (2000) and ANSYS (2006) the vertical altitude of the domain is used as L_t. The definition of the boundary conditions, as well as the problems with the implemented wall-functions (as discussed in section 6.1) are critically reviewed in Blocken et al. (2007).

5.5. Numerical solvers and software

The history of CFD started with the introduction of the first mathematical basics in the early years of the 20th century and, supported by the progress in the computer industry, has resulted in a wide range of methods and software packages. The software packages that implement CFD methods cover a wide range of applications in different research areas and fields, mainly targeting engineering problems. In the last decade the packages have been frequently used in environmental simulations (section 2.3). Within this thesis, the following two packages were used.

5.5.1. Commercial - ANSYS CFD / ANSYS ICEM CFD

For the study in part IV, the commercial software package ANSYS CFX and the meshing software ANSYS ICEM CFD were used ANSYS (2006). The software package covers all steps, from pre-processing (creating mesh, setup simulation), solving, over to post-processing (visualization, data extraction). The available license did not support parallel calculations.

5.5.2. Open-source - OpenFOAM

In the last years, the number of open-source packages increased in many different applications (Mockus et al., 2002). In the area of CFD, Open Field Operation and Manipulation (OpenFOAM) (Weller et al., 1998) is one of the most flexible software packages among the open source codes. The basic concept of the software package is to provide a set of C++ modules. The modules can be used to create solvers that suit the specific research or engineering questions. For this thesis, the solver *simpleFoam* and *pisoFoam* were mainly used and adapted and extended to fulfill the necessary additional features, such as vegetation (part V), logarithmic boundary conditions at boundaries with uneven elevations, etc. Further, the Lagrangian package *Intermediate* was adapted and applied (part V). For visualization purposes, the package 'Paraview' (Paraview, 2011) was used.

6. CFD roughness methods

This section covers the implementation of the roughness effects in the CFD theory introduced in section 5.

6.1. Sub-grid

As mentioned in section 5.4.3, flows near walls have different properties than free flow. In CFD methodology, this is implemented by wall-functions that adapt the turbulent viscosity ν_t based on dimensionless properties. With this approach, *subgrid* roughness effects can be modelled (Pope, 2000; Blocken et al., 2007). In this step, the research fields of meteorology and engineering meet. An adequate correlation between the different definitions of the roughness (for example in meteorology z_0 and in engineering sand-grain roughness height k_s) must be deducted (Blocken et al., 2007).

Because viscous effects have a minor influence in the free stream, but dominate together with the shear stresses in the near-wall region, viscous scale quantities are introduced to characterize the phenomena: the friction velocity u_τ and the wall units y^+ and u^+ (eq. 35 - 37).

$$u_\tau = \sqrt{\frac{\tau_w}{\rho}} \tag{35}$$

$$y^+ = \frac{u_\tau x_\perp}{\nu} \tag{36}$$

$$u^+ = \frac{\langle U \rangle}{u_\tau} \tag{37}$$

Figure 7 shows a schematic view of the first grid cell next to the wall. $x_{2,p}$ indicates the distance to the mid-point of the cell, where the dimensionless units (eq. 35 - 37) were applied.

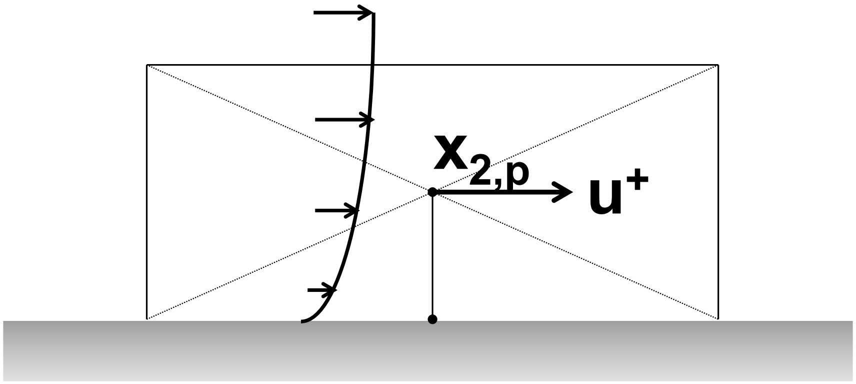

Figure 7: Schematic view on first grid cell next to the wall. $x_{2,p}$ indicates the distance to wall and u^+ the dimensionless velocity

If fluid moves over a fixed surface, boundary layers develop (Pope, 2000). The general distinction of the different layers is:

- viscous sublayer,
- buffer layer,
- log-law region

In the viscous sublayer, the wall unit y^+ equals u^+. In the log-law region, a logarithmic profile is developed and u^+ is described as:

$$u^+ = \frac{1}{\kappa} \ln y^+ + B - \triangle B(k_s^+) = \frac{1}{\kappa} \ln E y^+ - \triangle B(k_s^+) \tag{38}$$

with the Kármán constant $\kappa = 0.41$, $E = e^{B\kappa}$, B the integration constant, which is determined numerically by DNS simulations (Pope, 2000) and $\triangle B(k_s^+)$ represents the influence of the roughness. The bridge between the roughness length k_s and z_2, as well as the application is shown in detail in part V.
Further, the y^+ can be used to quantify the mesh resolution in the near-wall regions. The near-wall model approach requires the use of meshes with a high mesh density in the near-wall regions. The $k - \epsilon$ models are not capable of resolving the near wall flow and therefore $30 < y^+ \lesssim 300$ should be reached. Other two-equation models, such as the $k - \omega$ model are capable of resolving the near-wall flow without wall-functions at sufficiently high mesh resolutions ($y^+ < 5$) (Menter, 1994).

6.2. Impermeable

Opaque elements, such as buildings, must be geometrically resolved, if the influence on the fluid flow should be obtained. This leads to some complexity when creating the meshes. The geometry information is mostly provided in form of CAD or GIS data, from which a mesh has to be created, suitable for CFD analysis. The next sections introduce some mesh-techniques and also a problem with urban CAD models.

6.2.1. Geometrical datasets

There are detailed CAD models for cities existing. The model used in this thesis represent the city of Basel, Switzerland and was used for the studies in urban areas, part IV and part VI. Figure 8 shows an overview of the 3 dimensional CAD model.

The CAD model consists of polygon information in a Drawing Exchange Format (DXF)-file format with three different layers: The ground layer, consisting of Digital Elevation Model (DEM) model, a layer with the polygons describing the building walls and one layer with the roof properties. Each polygon is stored as a list of coordinates of the vertices and their connectivity. This gives a visual impression of a closed and very detailed surface of the city topology. But the

Figure 8: Image of the urban CAD model of Basel in birdseye perspective

geometrical data are often not directly be applicable to create meshes and there are often some major problems in urban city models (Krischok, 2009).

6.2.2. Meshes

The construction of meshes is an important step for CFD calculations and can influence the accuracy of the calculations significantly (Franke et al., 2004). Complex topology, such as urban areas consists of different objects. Unstructured meshes provide the highest flexibility to create body-fitted grids for complex geometries, but are the least accurate (Versteeg and Malalasekera, 2007). There are guidelines for CFD calculations in urban areas recommending the important parameters for CFD meshes (Franke et al., 2004; Tominaga et al., 2008).

6.2.3. Element shapes and mesh-types

Figures 9(a) to 9(d) show four commonly applied mesh-types.

Pure tetrahedral meshes are easy to build and result in body-fitted meshes. But they have some negative properties, such as higher truncation errors due to bulky shapes, poor iterative convergence and bad expansion ratios (Franke et al., 2004; Versteeg and Malalasekera, 2007). The near-wall regions are not perpendic-

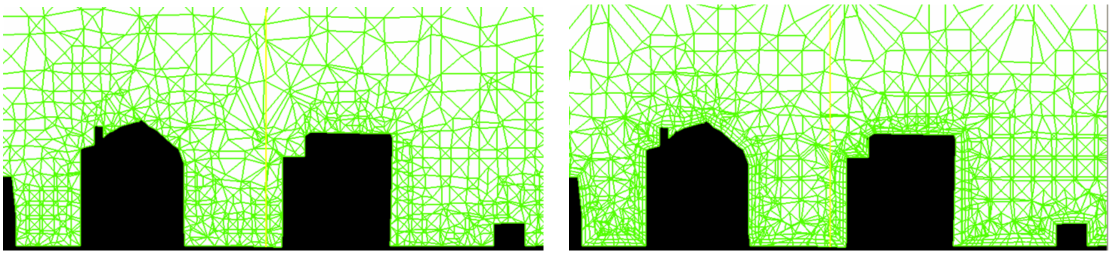

(a) Tetrahedral elements

(b) Tetrahedral elements with prismatic layers

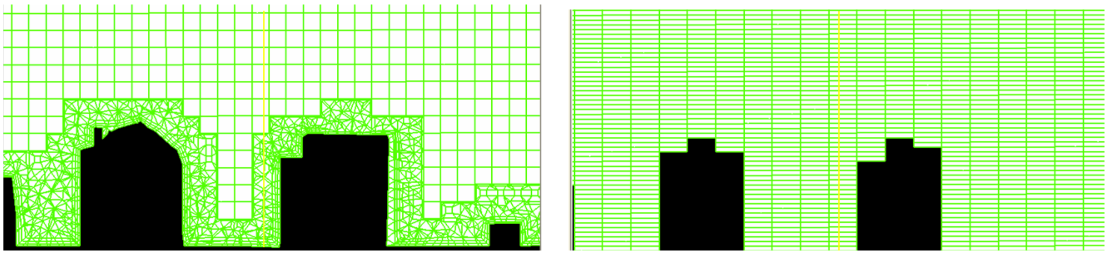

(c) Tetrahedral elements with prismatic layers and hexahedral elements

(d) Hexahedral / Cartesian mesh

Figure 9: Different mesh techniques demonstrated with an urban CAD model

ular to the building walls, leading to varying y^+, which can negatively influence wall-functions (section 6.1) (Pope, 2000). Introducing up to three prismatic layers around object walls (Fig. 9(b)) leads to a better iterative convergence behavior (Tominaga et al., 2008). The effort to build the hexahedral core in the free-stream regions, Fig. 9(c) is a possible solution to reduce truncation errors and the number of elements. Using plain hexahedral meshes (Fig. 9(d)) the detail of the geometrical representation is dependent on the mesh-resolution. Hexahedral meshes are easy to build and can handle even raw and volume-inconsistent (section 6.2.2) geometrical data sets, but need a sufficiently fine mesh resolution to represent the geometrical details correctly. Nevertheless, hexahedral meshes with a sufficiently high resolution to represent the object details, and a higher resolution near walls (where stronger gradients evolve) give rise to good convergence behaviour and smaller truncation errors (Franke et al., 2004; Karim et al., 2008).

6.2.4. The problem of volume inconsistency

The graphical representation of the object surfaces in the CAD data does not necessarily describe a closed surface. For example, the urban CAD model of the city of Basel consists of a large amount of single polygons ($> 200'000$ single entities) describing the topology. Due to discontinuous surfaces, these CAD data could not be used directly with standard meshing methods, as introduced in section 6.2.3.

One approach is to manually clean up the geometry, which is very time consuming and only feasable for small regions. But with this approach, it is possible to use meshing software, as ANSYS ICEM CFD, to build the meshes.

6.2.5. Specific approach for urban meshes

Within this study, a simple approach to create high quality meshes for spatially large computational domains with complex and raw urban CAD data was developed. The approach was designed for polygonal data sets, but can easily be extended to data sets based on DEM. The steps involved in creating a mesh from such data are:

Division of the geometrical data into layers The layers in the CAD model were split into a) terrain description (DEM) and b) description of the walls and roofs of the buildings and similar objects. The vertices were stored with their 3D coordinates and the connectivity according a unique identifier to make each polygon accessible by one index. To speed up a later search within the data, all polygons were associated with a 2 dimensional search grid. Each grid-element index holds the pointer to the polygon connectivity array, which consisted of the vertex indices.

Cartesian mesh A 3D structured cartesian mesh was built over the study site with a ground-following surface mesh, representing the DEM. A sufficiently fine mesh resolution must be specified to ressolve the urban structure in the coordinate system of the CAD data. The data was stored as a structured mesh, which means each ground-surface grid-cell specifies the horizontal coordinates of their four nodes and the cells in higher levels can be deducted from their element number. Besides the smaller storage use, the indexing and searching within a structured mesh is fast compared to searching within a unstructured mesh, where each element consists of nodes and no dependency on their location within the computational space can be deducted from neighbor cells.

Geometrical implementation For each ground cell, the vertical geometrical extent is calculated. This means, the calculation of lowest altitude h_{min} (normally from DEM-polygons) and the altitude of the highest polygon above the element centerpoint including the skew of roofs to obtain h_{max}. This needs a fast method to search within the geometrical separated data as introduced in the first paragraph. This step is stable even several polygons are superimposed upon each other. Also, holes in the geometry do not influence this method or lead to an interruption of the meshing process.

Conversion to unstructured mesh Unstructured meshes are the most flexible way in which to represent very complex geometrical data. Furthermore, the mesh input for most of the CFD software packages (section 5.5) are configured for unstructured meshes. Therefore, the structured Cartesian grid is converted into an unstructured grid by associating each cell face with the corresponding meta data (boundary conditions for CFD calculations) and deleting all elements with a value smaller than h_{max}.

Higher resolution near walls The last step makes it possible to select all wall faces in all elements, whereby each hexahedral element consists of 8 nodes and 6 faces describing the cell completely. Their faces can be extruded (n times), leading to a higher mesh resolution near walls for wall-functions ($y^+ > 30$).

The approach is also stable with geometrically faulty data, such as discontinuous topology, repetitive polygons with the same geometrical data, single polygons describing e.g. eaves, etc. and leads to an ideal mesh as defined by Franke et al. (2004).

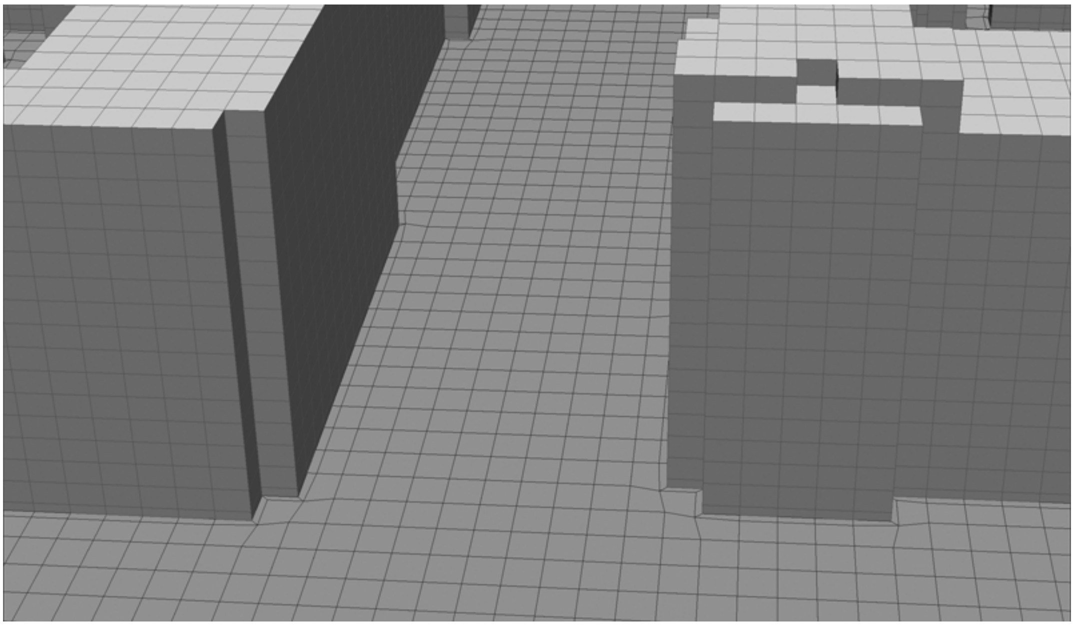

Figure 10: Mesh with one boundary layer around all walls (ground and building), representing impermeable boundaries for flow

Figure 10 shows a small extent of the meshed domain, with the horizontal resolution given by a mean grid spacing of 1.5 m and vertical extension of 100 m. In the bottom 25 m, the resolution is 1 m, after which the vertical grid spacing irregularly increases (max. 3 m) to achieve a detailed representation of the buildings. Additionally, two sub-layers were created near the building walls and ground with a resolution of each approx. 0.5 m.

6.3. Porous

Porous structures can be modelled by different methods, e.g. as porous media (Santiago et al., 2007). But the internal structure of the vegetation can have an important influence on the flow evolution (Zhou et al., 2004). To incorporate the effect in the introduced CFD methods in section 5, an additional source term is added to the governing equations. This reflects the effects of vegetation in the CFD calculations (Kobayashi et al., 1994; Wilson and Shaw, 1977). The source terms are described here only with few comments, as their derivation is described in detail in part V.

To reduce momentum, a negative source term is added in the RANS equations (eq. 16):

$$S_{u,i} = \frac{1}{\rho}\frac{\partial p}{\partial x} = C_d \alpha |U| U_i \tag{39}$$

Both parameters C_d and α are dependent on the vegetation canopy. α is the Leaf Area Density (LAD) of the vegetation and C_d the drag coefficient. According to Green et al. (1995), trees reduce turbulent energy and following Sanz (2003), the loss in the k transport equation (21) can be modelled with:

$$S_k = C_d \alpha \left[\beta_p |U_i|^3 - \beta_d k |U_i|\right] \tag{40}$$

where $\beta_p \in [0, 1]$ is the transfer coefficient of turbulent energy production by the mean velocity and β_d the coefficient for the TKE breakdown. Furthermore, the source term for the dissipation is:

$$S_\epsilon = \frac{C_d \alpha}{2} \left[C_{\epsilon 4} \beta_p \frac{\epsilon}{k} |U_i|^3 - C_{\epsilon 5} \beta_d |U_i| \epsilon\right] \tag{41}$$

According Sanz (2003) the production β_p, the reduction factor β_d and, depending of the turbulence model, the model constants $C_{\epsilon 4}$ and $C_{\epsilon 5}$ can be derived independent on the vegetation characteristics.

The vegetation density is incorporated into the computational domain by adding a new static field. Figure 11 shows an example for an α-field implemented within a domain.

7. CFD dispersion and transport

The introduced CFD methods allow the computation of wind fields in the different roughness classes *sub-grid*, *impermeable* and *porous*. Two different types of material are transported in environmental flows: gaseous fluids and solid particles (e.g. PM10-particles from traffic exhausts). The simulated wind fields can

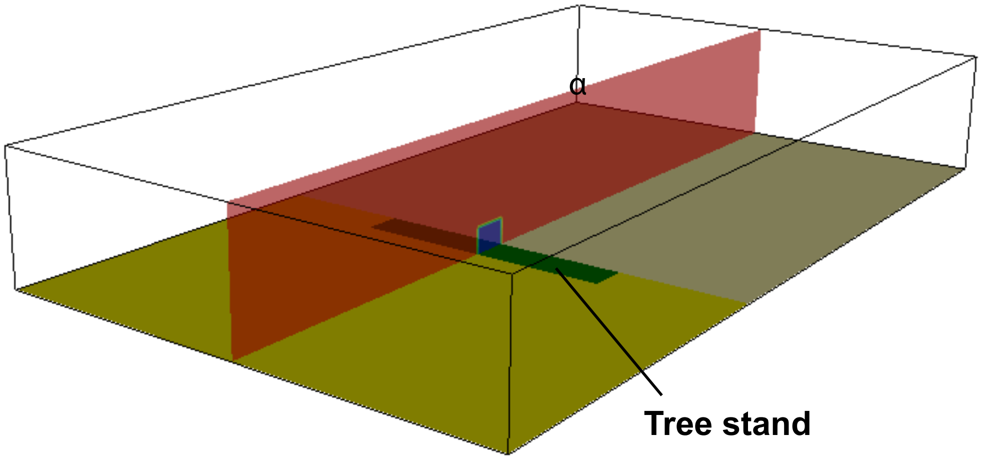

Figure 11: Incorporation of vegetation (dark green rectangle) by the leaf-area density α (blue to red shaded cross-section) in a computational domain

be used to model the corresponding dispersion and transport processes of fluids. CO_2 disperses during transport, but is transported with the fluid (part IV). Solid particles, with a defined weight m and diameter D, experience buoyancy and drag forces (part V). The next two sections introduce the basics for both types of transported materials.

7.1. Gaseous fluids

If a soluble fluid is transported, it can be seen as a multicomponent flow. This approach was used for the simulation of CO_2 dispersion in section IV. In multicomponent calculations, the fields are computed only for a single fluid based on the governing equations. The fluid for which the flow fields are calculated is considered as a mixture of individual fluids. The influence of the different fluid components is represented by the individual fluid properties within the mixture. The properties of the mixture in each cell is dependent on the proportion of each component in the cell. The proportion of each component in the domain can be calculated by solving an additional continuity equation for each component in the mixture (eq. 13):

$$\tilde{\rho}_i \frac{\tilde{U}_i}{\delta x_i} = -\frac{\delta}{\delta x_i} \left\{ \rho_i (\tilde{U_{ij}} - \tilde{U_i}) - \overline{\rho_i u_j} \right\} \tag{42}$$

where ˜ indicates the mass-average, as for $\tilde{\rho}_i$ is the mass-averaged density and $\tilde{U_{ij}}$ the mass-averaged velocity of fluid of component i (ANSYS, 2006). The relative mass flux term $(\tilde{U_{ij}} - \tilde{U_i})$ models the motions of the individual components in the mixture. The primary driver for these motions are concentration gradients. These lead to relative diffusive motions of the components in the mixture. The kinematic diffusivity D_i controls the physical influence of the single components in the mixture. The turbulent fluxes $\overline{\rho_i u_j}$ can be modelled using the eddy-dissipation assumption (section 5.3.1), which leads to an advection-diffusion equation for the proportion of the component in each cell Y_i for component i:

$$\frac{\partial(\bar{\rho}\tilde{U_j}\tilde{Y_i})}{\partial x_j} = \frac{\partial}{\partial x_j}\left\{\frac{\partial Y_i}{\partial x_j}(\rho_i D_i + \frac{\mu_t}{Sc_t})\right\} \tag{43}$$

where Sc_t is the turbulent Schmidt number $Sc = \nu_t/D$. The standard continuity equation can be obtained (eq. 13), if all component continuity equations (eq. 42) are summed.

7.2. Solid particles

To model transport of solid particles with weight m and diameter D, a Lagrangian approach can be used. Lagrangian approaches describe the flow or path of a fluid element, from the perspective of the element, whereas Eulerian approaches have the perspective of the fluid field.

Particles transported by air are influenced by different forces, including gravity, aerodynamic drag and lift. Newton's Second Law postulates the following relation for a falling particle in the air (Shao, 2008):

$$\rho_p V\frac{\partial U_{i,p}}{\partial t} = -\rho_f\frac{\pi D^2}{8}C_d(U_{i,p} - U_i)|U_{i,p} - U_i| + Vg(\rho_p - \rho_f) \tag{44}$$

where the index p denotes particle properties, f for the gaseous fluid, $g = 9.81ms^{-2}$, the gravitation constant, V the volume and D the particle diameter. The particle aerodynamic drag coefficient is dependent on the particle Reynolds number Re_p (Shao, 2008) as follows:

$$Re_p = \frac{|U_{i,p} - U_i|D}{\nu} \ll 1 : C_d = \frac{24}{Re_p} \tag{45}$$

$$Re_p < 1000 : C_d = \frac{24}{Re_p}(1 + \frac{1}{6}Re_p^{2/3}) \tag{46}$$

$$Re_p > 1000 : C_d = 0.424 \tag{47}$$

Turbulent behavior of the gaseous fluid strongly influences particle motion, especially if they are small (Fritsching, 2004). The influence of turbulence on the particle trajectories can be incorporated according to Sommerfeld (1992). The basic idea is that the turbulence influences the particle path during a defined time period τ_i, which is precisely the time, that the particle is influenced by one eddy, before the influence of an other eddy begins.

$$\tau_i = \frac{L}{|U_{i,p} - U_i|} \tag{48}$$

where L is the Lagrangian integral length of the turbulence according Sommerfeld (1992)

$$L = c\frac{k}{\epsilon} \tag{49}$$

where $c = 0.3$ is a constant derived from experiments. The fluctuating velocities are sampled using a Gaussian distribution with a standard deviation of an isotropic turbulence field $u_i = \sqrt{2k/3}$ (Gjesing et al., 2009).

Part III.
CFD in field experimental study

Andres Gartmann, Wolfgang Fister, Wolfgang Schwanghart, Mathias D. Mueller (2011)
CFD modelling and validation of measured wind field data in a portable wind tunnel,
Aeolian Research, Volume 3, Issue 3, 315-325, DOI 10.1016/j.aeolia.2011.07.002

Aeolian Research 3 (2011) 315–325

Contents lists available at ScienceDirect

Aeolian Research

journal homepage: www.elsevier.com/locate/aeolia

CFD modelling and validation of measured wind field data in a portable wind tunnel

Andres Gartmann[a,*], Wolfgang Fister[b], Wolfgang Schwanghart[b], Mathias D. Müller[a]

[a] Institute of Meteorology, Climatology and Remote Sensing, University of Basel, Klingelbergstr. 27, CH-4056 Basel, Switzerland
[b] Physical Geography and Environmental Change, Department of Environmental Sciences, University of Basel, Klingelbergstr. 27, CH-4056 Basel, Switzerland

ARTICLE INFO

Article history:
Received 10 September 2010
Revised 5 July 2011
Accepted 5 July 2011
Available online 12 August 2011

Keywords:
Wind erosion modelling
Computational fluid dynamics
Wind tunnel
RANS
Turbulence models

ABSTRACT

Computational fluid dynamics (CFD) methods enable the detailed study and analysis of three dimensional flow patterns. This article provides a basic introduction to the fundamentals of CFD and its application as an assessment tool for near-wall boundary layers in internal flows. The Reynolds-averaged Navier–Stokes (RANS) approach with the k–ϵ turbulence model was used to model the characteristic channel flow properties observed in a portable wind tunnel with a coupled rainfall simulator. Wind velocity fields were measured at four cross-sections and compared to simulated data sets.

A good correspondence between simulated and measured velocity profiles was obtained (RMSE 0.5 ms^{-1}). In addition, we simulated the complex flow patterns caused by the specific construction of the wind tunnel and calculated the spatial distribution of derived measures such as wall shear stress and turbulence characteristics. It is shown that these measurements deviated significantly from their theoretical distributions, and an explanatory model for an observed bias in wind erosion and transport rates experimentally derived in the tunnel could be developed.

We conclude that CFD is a valuable tool for modelling measured flow fields and to assess the spatial variation of variables that often cannot be sufficiently covered by measurements. Nevertheless, accurate measurements of the wind field are necessary to calibrate and validate such simulations and to provide reliable boundary conditions. CFD is thus a promising tool for aeolian research being complementary, to but never separated from, a measurement setup.

1. Introduction

The application of computational fluid dynamics (CFD) in aeolian research and wind engineering has significantly increased in the last two decades (Murakami et al., 1999; Parsons et al., 2004; Bauer, 2009). CFD implements the concepts needed to solve the governing equations for fluid mechanics using numerical methods and is often used jointly with physical experimentation, such as wind tunnels or field studies. Recently, CFD has been increasingly applied in aeolian research to provide new insights into flow dynamics and its interactions with soil surfaces and particles (Parsons et al., 2004).

The application of CFD is often motivated by the limitations of measurement techniques. Measuring devices may interfere with the wind field and produce measurement artifacts (Greeley et al., 1996) or may be often limited in spatial coverage. In addition, measurements usually require elaborate equipment, manpower, and time and thus involve high costs. Interpolation techniques are frequently used to overcome this problem and to obtain spatially and temporary coherent information. These techniques rely on various assumptions and results are usually associated with high uncertainties. Thus, CFD models are used to assess different scenarios that cannot be, or are too costly to be, investigated experimentally (Wakes et al., 2010) and were shown to be a flexible, efficient and cheap alternative to experimental setups (Alhajraf, 2004; Parsons et al., 2004).

At the same time, there is a strong need for validation and assessment of the data obtained by simulation. It is not merely the feedback process of formalizing knowledge and testing if theory is in conflict with reliable data, but numerical approximations, parametrization schemes (e.g. turbulence models, discretization techniques) and the choice of boundary conditions can introduce errors in simulated data sets that should be evaluated against measured data.

Recent advances in computational techniques have considerably increased the use of numerical models, a demand that is encountered by a growing range of commercial and academic CFD software. There is considerable scope for further research in the application of these tools to a wide range of problems in aeolian dynamics. The effective application of CFD, however, requires training in these methods, a thorough understanding of the physical basis of models applied and their inherent limitations of their assumptions (Lane, 1998).

---

* Corresponding author. Tel.: +41 61 267 06 88; fax: +41 61 267 06 89.
E-mail address: andres.gartmann@unibas.ch (A. Gartmann).

1875-9637/$ - see front matter © 2011 Elsevier B.V. All rights reserved.
doi:10.1016/j.aeolia.2011.07.002

Here, we present results of a study that was conducted to characterize the wind field in a portable wind and rainfall tunnel using CFD. The portable wind tunnel is used to experimentally assess wind and water erosion in the field. During development and construction of the wind tunnel emphasis was placed more upon optimizing mobility than on approximation to natural wind and rainfall conditions (Fister and Ries, 2009). This implies considerable limitations of the development of a thick boundary layer. The central aim of this study is to assess the aerodynamic properties of the wind tunnel and to identify possible artifacts introduced by the experimental setup itself by modeling the wind field using a CFD approach. Our key objectives are (i) to shortly describe the numerical techniques to solve the governing equations, (ii) to simulate and validate the wind velocity patterns in the wind tunnel, (iii) to highlight the problems and potentials of the wind tunnel based on the results of the simulation, (iv) and to show how these results can be used to explain spatial patterns of erosion and transport in the tunnel.

2. Basic principles

2.1. Governing equations

CFD simulations usually involve discretization and solution of the Navier–Stokes-equations (NSE). The NSE describe the physics of liquids and gases in motion and can be written for incompressible fluids as

$$\frac{DU_i}{Dt} = -\frac{1}{\rho}\frac{\delta p}{\delta x_i} + f_i + \mu\frac{\delta^2 U_i}{\delta x_j^2} \tag{1}$$

where U_i are the velocity components in three dimensions, f_i the body force per unit mass, ρ the density and μ the dynamic viscosity (Versteeg and Malalasekera, 1995).

The continuity equation for incompressible flows is:

$$\frac{\partial U_i}{\partial x_i} = \bigtriangledown \mathbf{U} = 0 \tag{2}$$

Incompressible flows are characterized by very low Mach numbers, where the Mach number Ma refers to the ratio between the flow speed and the sound speed (Wilcox, 2000). The term incompressible thus describes a property of flow and not a fluid property.

2.2. Turbulence modelling and closure problem

Turbulent-flow simulations involve the computation of a velocity field as one realization of the turbulent flow. The two best known turbulent simulations are direct numerical simulations (DNS) and Large Eddy simulations (LES). DNS of the NSE renounce a turbulence model and are very cost- and time-intensive since all significant time- and length-scales are resolved (Shao, 2008). The computational costs increase with the Reynolds number Re^3 (Eq. (8)). LES solve the equations for a filtered velocity field for the larger-scale turbulence motions and apply turbulence models for non-resolved turbulent motions. Turbulence models imply that the fluid motion is computed based on mean quantities (Pope, 2000). One of the most applied turbulent models approach is obtained by applying the Reynolds decomposition (Eq. (3)) to the NSE (Eq. (1))

$$U_i = \langle U_i \rangle + u_i \tag{3}$$

which leads to the Reynolds-averaged Navier–Stokes (RANS) equations

$$\frac{\bar{D}\langle U_i \rangle}{\bar{D}t} = -\frac{1}{\rho}\frac{\partial \langle p \rangle}{\partial x_i} + f_i + \nu\frac{\partial^2 U_i}{\partial x_i^2} - \frac{\partial \langle u_i u_j \rangle}{\partial x_j} \tag{4}$$

The additional terms $\frac{\partial \langle u_i u_j \rangle}{\partial x_j}$ are called the Reynolds stresses and are crucial to turbulence modeling using the RANS method. The mean velocity field is governed by four independent equations (Eqs. (2) and (1)). $\langle U_i \rangle$, $\langle p \rangle$ and the Reynolds stresses constitute more than four unknown variables and the set of equations cannot determine all the unknown variables, which is described as "unclosed". The Reynolds stresses have to be defined in a separate exercise to solve the so called "closure problem". The approaches used to solve the closure problem are divided into models using the turbulent viscosity hypothesis and models using Reynolds stresses transport equations (Pope, 2000). The turbulent-viscosity hypothesis (Eq. (5)) introduces a proportional relation between the Reynolds stresses and the mean rate of strain using a scalar coefficient, the turbulent viscosity ν_t

$$\langle u_i u_j \rangle = \frac{2}{3}k\delta_{ij} - \nu_t\left(\frac{\partial \langle U_i \rangle}{\partial \langle x_j \rangle} + \frac{\partial \langle U_j \rangle}{\partial \langle x_i \rangle}\right) \tag{5}$$

where k is the turbulent kinetic energy (TKE) $\frac{1}{2}\langle u_i u_i \rangle$. Among the more evolved methods to compute the turbulent viscosity are two-equation models. There are a wide range of approaches (Pope, 2000) of which the k–ϵ model is the most commonly used model in engineering applications. It solves two transport equations for the TKE k and the dissipation ϵ. Then the turbulent viscosity is obtained by Eq. (6)

$$\nu_t = C_\mu \frac{k^2}{\epsilon} \tag{6}$$

where $C_\mu = 0.09$ is a model constant. Based on ν_t, the Reynolds stresses (Eq. (5)) are obtained and using this additional equation, all unknown properties in the NSE can be computed.

3. Methods

3.1. Numerical methods

Advection terms, such as $\langle U_i \rangle \frac{\partial \langle U_i \rangle}{\partial x_i}$ in the NSE (Eq. (1)) contain non-linear quantities and are intricately coupled (Versteeg and Malalasekera, 1995). To solve the NSE, the velocity field has to be known and so the pressure has to be resolved. There is no transport equation for the pressure term p. In compressible cases, the pressure term is derived from density and temperature of the fluid. In the incompressible case, the density is constant and the velocity field satisfies the incompressible continuity equation (Eq. (2)) for a given pressure field. Several methods were elaborated such as the semi-implicit method for pressure-linked equations (SIMPLE) (Versteeg and Malalasekera, 1995) which calculates the pressure in an iterative procedure so the velocity field is divergence free (Eq. (2)). A pressure field p^* is estimated and linked to the pressure field $p = p^* + p'$ with a correction pressure term p'. The estimated pressure is used to solve the momentum equations, which gives an estimated velocity field U_i^*. U_i^* is coupled to the velocity field U_i by the correction pressure term p'. By solving the continuity equation for the correction pressure field p', a divergence free velocity field can be found. Other methods used to solve the conjunction in the advection terms of the NSE are described in Versteeg and Malalasekera (1995).

The NSE (Eq. (4)) is a partial differential equation (PDE). To solve the PDE on a computational domain, the domain is split into finite cells and the PDE is discretized on the mesh vertices. One method to discretize the PDE on the domain is the finite volume method (FVM) (Versteeg and Malalasekera, 1995). By integrating the terms of Eq. (4) over a cell volume V, the PDE can be expressed in integral form. Using Gauss's theorem, most of the derivative terms can be converted to surface integrals

$$\int_V (\nabla \cdot \mathbf{F})dV = \int_S \mathbf{F}\cdot \mathbf{n}dS \approx \sum \mathbf{F}\cdot \mathbf{S} \tag{7}$$

where **F** is any tensor field and **n** the normal vector on the surface **S**. The surface integrals and the summation of the flux terms over the cell bounds are discretized by different schemes, e.g. central or upwind differencing, Versteeg and Malalasekera (1995). The discretization of PDE on the complete domain leads to a set of discretized equations. These equations are solved using iterative methods such as the conjugate gradient method (CGM) (Hestenes and Stiefel, 1952; Weller et al., 1998).

3.1.1. Boundary conditions and wall function

Boundary and initial conditions must be defined to completely specify the PDE. Boundary conditions have to be specified for the computational domain and characterize the flow behavior at the domain boundaries. Two types of boundary conditions exist (OpenFOAM, 2009): Dirichlet and Neumann. While Dirichlet conditions set the value of a dependent variable to a fixed value, Neumann conditions prescribe a gradient of the variable. Initial conditions specify the flow conditions at the simulation time $t_0 = 0$.

Boundary conditions for solid boundaries for the fluid are Dirichlet conditions. In the near-wall region, different phenomena to the free-flow conditions can be found e.g. for a wall there will be: (1) lower Reynolds numbers, (2) higher sheer stresses, (3) $\langle u_2^2 \rangle$ turbulence varies with x_2^4, where x_2 is the vector normal to the wall, $\langle u_1^2 \rangle$ and $\langle u_3^2 \rangle$ varies with x_2^2 and (4) the impermeability condition $U_2 = 0$ affects the flow up to the integral scale from the wall (Pope, 2000).

To account for these circumstances, the wall conditions in CFD calculations have characteristic properties. These were derived from channel flows, where the boundary layer plays an important role and were intensively studied at the end of the 1980s using experimental data and DNS results (Pope, 2000). The Reynolds number Re_0 is used to characterize flows

$$Re_0 = \frac{\overline{U}_0 h}{2\nu} \tag{8}$$

where $\overline{U}_0 = \langle U \rangle_{x_2 = h/2}$ is the mean velocity at the midpoint of the channel and h the vertical channel height. Based on the NSE (Eq. (4)) the total shear stress is calculated as function of the vertical channel coordinate x_2 (Eq. (9))

$$\tau = \rho\nu \frac{d\bar{U}_3(x_2)}{dx_2} - \rho\langle u_2 u_3 \rangle \tag{9}$$

Viscous effects have a minor influence in the free stream, whereas in the near-wall region, viscous effects and the wall shear stress $\tau_w = \tau(x_2 = 0)$ are important properties. These can be characterized by viscous scales quantities: the friction velocity u_τ and the wall units y^+ and u^+ (Eq. (12))

$$u_\tau = \sqrt{\frac{\tau_w}{\rho}} \tag{10}$$

$$y^+ = \frac{u_\tau x_2}{\nu} \tag{11}$$

$$u^+ = \frac{\langle U \rangle}{u_\tau} \tag{12}$$

Treatment of flow in the near-wall region can be simplified by considering four different regions:

- viscous sublayer, $y^+ < 5$
- buffer layer, $5 < y^+ < 30$
- log-law region, $y^+ > 30$ and $\frac{2x_2}{h} < 0.3$
- outer layer, $y^+ > 50$

The fully developed mean velocity gradient profile in a channel can be defined by the friction velocity u_τ and an additional, flow specific, non-dimensional function (Pope, 2000). For the viscous sublayer and the log-law region, different relations for u^+ can be evaluated. In the viscous sublayer the wall unit y^+ is equal the u^+. In the log-law region u^+ is described by:

$$u^+ = \frac{1}{\kappa}\ln y^+ + B = \frac{1}{\kappa}\ln E y^+ \tag{13}$$

with the Karman constant $\kappa = 0.41$, $B = 5.2$ (determined by DNS simulations) and $E = e^{B\kappa}$. The outer layer is described by the velocity-defect law not shown here.

The wall laws are crucial in CFD simulations: In high Reynolds number flows, and to incorporate the influence of surface roughness, the transport equations for the turbulent quantities in the RANS approach as well as the turbulent viscosity (Eq. (6)) are adjusted using wall functions (Pope, 2000; Blocken et al., 2007). These wall functions are based on the segmentation of the near-wall flow and the corresponding terms, for the turbulent viscosity in the log-law region, Eq. (13). The described k–ϵ model needs wall functions to be able to model boundary flow. More sophisticated models, like the k–ω are able to resolve the near-wall regions without the use of wall functions (Menter, 1994) but are computationally more expensive and require higher resolved data of the inlet boundary conditions in the near-wall region. The near-wall model approach requires the use of meshes with a high mesh density in the near-wall regions. The y^+ can be used to quantify the mesh resolution in the near-wall regions. For wall treatment using wall functions a $y^+ < 30$ is needed to resolve the wall region appropriately. For resolving the wall region with, for example a k–ω model, $y^+ < 5$ has to be obtained (Salim and Cheah, 2009).

3.1.2. Atmospheric boundary layer and particle detachment

The velocity in a neutral atmospheric boundary layer can be expressed following Richards and Hoxey (1993) as

$$U(z) = \frac{u_*}{\kappa}\log\left(\frac{z + z_0}{z_0}\right) \tag{14}$$

where z_0 is the aerodynamic roughness length. The friction velocity is calculated using expression

$$u_* = \frac{\kappa U_0}{\log\left(\frac{h_{ref} + z_0}{z_0}\right)} \tag{15}$$

where U_0 is the velocity at a reference height h_{ref} above ground. z_0 is a roughness parameter of the surface. Various studies (Shao, 2008) show that z_0 is approximated by 1/30 of the roughness element height and tables of values exist for different surface types. For example, sea and smooth desert have $z_0 = 0.0002$ and city centers have $z_0 > 2$ according to the Davenport–Wieringa classification (Stull, 2000). The theoretical profile (Eq. (14)) is used as reference velocity profile to characterize the CFD results as well as the flow in the portable wind channel.

The characteristic of the flow near the surface governs particle detachment and transport. Data on flow characteristics in the free stream and boundary layer and its interplay with the surface derived from CFD methods can thus provide valuable quantities to assess particle detachment and transport. The motion of a particle in the air is influenced in general by aerodynamic and gravity force (Shao, 2008) and the terminal velocity can be expressed as

$$w_t = g\frac{4d\sigma_p}{3C_d(Re_p)w_t} \tag{16}$$

where σ_p is the particle-to-air density ρ_p/ρ, d the particle diameter, C_d the aerodynamic drag coefficient and $Re_p = w_t d/\nu$. Here we applied following equation for the drag coefficient (Shao, 2008).

$$C_d = \frac{24}{Re_p}\left[1 + 0.15Re_p^{0.687}\right] \tag{17}$$

According to Shao (2008) the terminal velocity w_t can be used to characterize the particle motions in suspension, saltation and creep. The vertical velocity in atmospheric surface layers is approximately κu_* (Shao, 2008). By combining Eq. (16) and the vertical velocity, a function for the critical diameter d_{ss}, where particles with smaller diameters than d_{ss} are suspended and larger are saltated, can be obtained:

$$w_t(d_{ss}) = \kappa U_* \tag{18}$$

3.1.3. Numerical solvers and software

Different commercial software packages such as ANSYS CFX (ANSYS, 2006) and open-source CFD codes exist. They cover a wide range of application fields mainly targeting engineering problems. OpenFOAM (Weller et al., 1998) is one of the most flexible software packages among the open-source codes. The basic concept of the software package is to provide a set of C++ modules that can be used to create solvers that best fit the specific research or engineering question. Additional pre- and post-processing utilities complete the library. Here, we used version 1.7.0 and the 'simpleFoam' solver (OpenFOAM, 2009) which solves the incompressible and steady NSE for Newtonian fluids.

3.2. Experimental setup and measurement

The wind tunnel of a portable wind and rainfall simulator was used for this study (Fig. 1). The main focus during development and construction of the tunnel was its portability, and thus its application in field surveys. Studies on wind and water erosion in central Aragon and Andalusia, Spain, showed its applicability in-situ soil erosion research (Fister and Ries, 2009).

The air-stream of the push-type wind tunnel is generated by a 4 kW fan with 163 cm^3. A transition section of four meters length leads the airstream to the honeycomb (H = 0.7 m, W = 0.7 m, L = 0.15 m, tube opening of 0.04 m). A baffle made of 0.4 mm thick plywood is attached in front of the honeycomb (angle of 22°) in order to divert the air stream from the upper 0.2 m downwards, thus creating higher wind velocities near the ground and reducing wind velocities at the tunnel roof where the rainfall nozzles are situated. A double layer of wire mesh (spacing of 5 mm) is attached to the honeycomb to further reduce turbulence of the air-stream. The lowest tube row (0.04 m) is blocked with gaffer tape creating a tripping fence. Downstream of the honeycomb there is a 0.5 m long fetch, which is covered with a floor mat to protect underlying soil from deflation and rainfall. This setup, including fan orientation, baffle, wire mesh, honeycomb, tripping fence and fetch, is meant to create a preformed turbulent boundary layer with best possible homogeneity and reproducibility.

The working section of the wind tunnel has the same cross-section as the honeycomb (0.7 m × 0.7 m) and a length of 4 m. The tunnel itself is made of four separate 1 m long sections of aluminium and Perspex sheets that can be folded up completely for transport. The wind tunnel covers a test plot 2.2 m wide and 3.15 m long. The plot can be easily accessed by opening the Perspex sheets on one side of the tunnel for preparation and measurement. A more detailed description of the tunnel (Fig. 2), the rainfall component and its simulated wind and rainfall conditions is given in Fister et al. (2011a,b).

Characterization of wind conditions in the tunnel was achieved using a pietot tube and a multi-functional sensor (Testo 435-3). In addition to recording static and dynamic pressure of wind-flow, the air temperature and humidity were measured with a frequency of 1 Hz for intervals of 20 s at every measurement point, thus allowing calculation of wind velocities from recorded dynamic pressure values. Four complete cross-sections of the tunnel were measured at 0.5 m, 1.5 m, 2.5 m, and 3.5 m downstream of the honeycomb (see Fig. 2). The first cross-section at 0.5 m is used as inlet for all calculations with CFD and is therefore defined as the zero position. According to their position behind the inlet, the following cross sections at 1.5 m, 2.5 m, and 3.5 m are therefore defined as 1.0 m, 2.0 m, and 3.0 m, respectively. Spacing between measuring points was $\Delta x = \Delta z = 0.05$ m, resulting in a total number of 169 locations per cross-section (see Fig. 2). Wind velocities at each position were measured consecutively for 20 s. In addition, vertical wind velocity profiles were measured at each cross-section at the centerline (0.35 m away from both sides of the wind tunnel).

Fig. 1. Wind tunnel setup for wind field calibration measurements. A bottom structure made of wood and roof cardboard was used to create constant conditions for the calibration (outdoor laboratory). In the field, the wind tunnel has an open floor with natural soil surface.

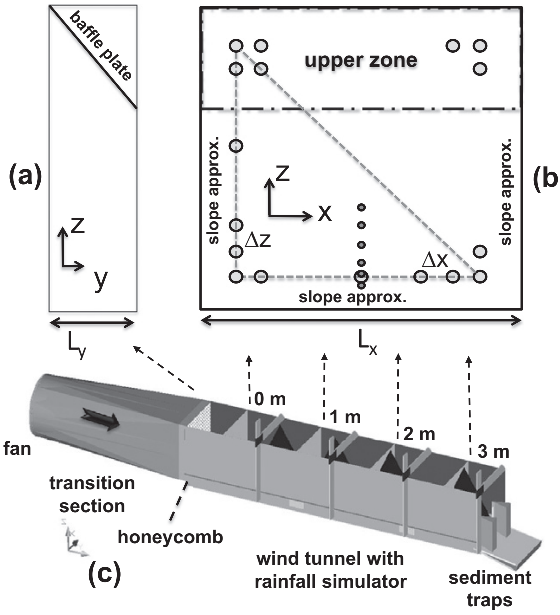

Fig. 2. Schematic view of wind tunnel and measurement points: (a) inlet region with baffle (b) inlet cross-section with measurement grid points (dots) $\Delta x = \Delta z = 0.05$ m. The upper zone is the region behind the blend with lower velocity. L_y = 0.7 m and L_x = 0.5 m (c) wind tunnel with positions of cross-sections.

Fig. 3. Image of the gutter at the end of the wind channel. More residual sediment is caught underneath the upper wedge trap.

Out of three repeated measurements a mean velocity profile was calculated. Spacing between points of measurements was 0.01 m below 0.2 m height and 0.05 m for heights ranging from 0.2 m to 0.4 m.

The prototype of a combined sediment trap for simultaneous sediment collection of surface runoff and wind-driven material is only briefly described here. A more detailed description of the sampler and the measurement procedure is given in Fister and Schmidt (2008). The surface runoff from the plot is collected in a gutter system (Fig. 3) made of 0.5 mm thick aluminium sheets ($W = 0.7$ m, $L = 0.6$ m). Apart from sediment detached and transported by interrill processes, the creeping and rolling fraction of sediment transported by wind can also be collected with the gutter. The gutter is covered by a roof of same dimensions for protection from direct rainfall and to collect detached wind-driven splash material. Attached to the gutter system are two wedge-shaped sediment traps and a beam with four Modified Wilson and Cooke Samplers (Wilson and Cooke, 1980).

4. Results and discussion

4.1. Comparison of theoretical and measured wind profiles

The analytic logarithmic velocity profile (Eq. (14)) is used to compare the measured velocity profiles with the ideal atmospheric boundary profile. The measured profiles deviate from the ideal profile below 0.05 m and above 0.2 m. A good accordance was observed between these heights. The correlation between the ideal and measured profiles increases with distance from the inlet. The discrepancy in the lower part aggravates the derivation of u_* and z_0 (Fig. 4). The best accordance over the whole profile was found using for U_0 at $h_{ref} = 0.1$ m from the measurements 3 m behind the inlet and $z_0 = 0.0005$. This value characterizes the ground as very smooth and agrees with the experimental setup.

The theoretical mean velocity profile largely disagrees with the inlet profile (Fig. 4). While the correlation between the theoretical and the experimental profiles increases with distance from the inlet, the clear difference at the inlet shows that the inlet profile is not consistent with an analytically fully developed velocity profile in an ideal channel flow. The disparity is most likely related to the inlet configuration of the tunnel, partly the 4 cm high tripping fence and especially the baffle plate that generates a flow regime different from an ideal channel geometry. In the near-surface region $0 < z < 0.05$ m the velocity is higher than that of the theoretical profile. The higher similarity of the theoretical profile and the profiles at $y = 1, 2$ and 3 m behind the inlet indicate an increasing adjustment of the preformed wind field to boundary conditions with distance from the honeycomb.

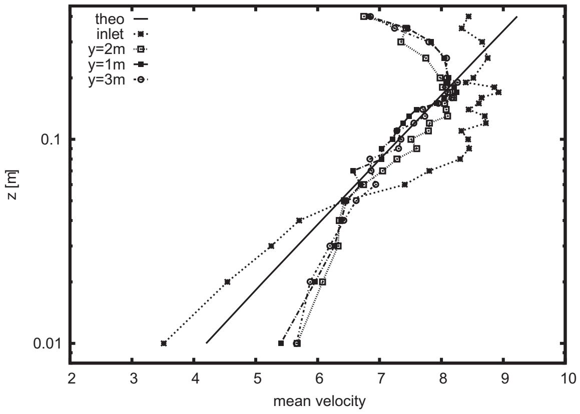

Fig. 4. Theoretical mean velocity inlet profile based on the wall laws and measured mean velocity profiles at the inlet and at $y = 1$, 2, and 3 m behind the inlet.

The distinct velocity reduction for $z > 0.25$ m is only partly caused by the friction from the upper boundary (roof). Instead, it is induced by the position of the baffle that deflects the air flow from the upper 0.2 m downwards to reduce wind velocities near the roof where pressure nozzles are installed. These intrinsic constraints for the theoretical channel velocity profiles were expected and taken into account to guarantee good rainfall conditions and the portability of the combined wind and rainfall simulator.

The structural setup of the wind tunnel induces differences to an ideal boundary wind profile, especially in the near-surface regions and implies that the analytical model is not applicable to characterize the wind field in the tunnel. It will be shown in the following sections that solving the NSE using CFD allows for a detailed, three-dimensional description of the aerodynamic characterization of the tunnel.

4.2. Mesh configuration and boundary conditions

The CFD simulations were run with two different mesh configurations. A fixed element size of $\Delta y = 0.01$ m was specified for both meshes along the length of the tunnel. One mesh was built using a uniform mesh resolution in x and z direction with $\Delta x = \Delta z = 0.01$ m (Fig. 5a). The second mesh was refined in the near-wall regions (Fig. 5b) to enable higher y^+ in the computations. A mean $y^+ \simeq 5$ could be obtained for the refined mesh, while the uniform mesh has $y^+ \simeq 22$.

The wind-tunnel chamber was modeled using the measured values at the first cross Section (0.5 m behind honeycomb) as inlet boundary conditions. The experimental data were resampled to the higher spatial resolution of the computational grid using linear interpolation. Since experimental data is unavailable for regions close to the tunnel walls, an extrapolation scheme is required to characterize the inlet boundary conditions in this area. Based on the wall boundary theory, this region is not in the viscous sublayer

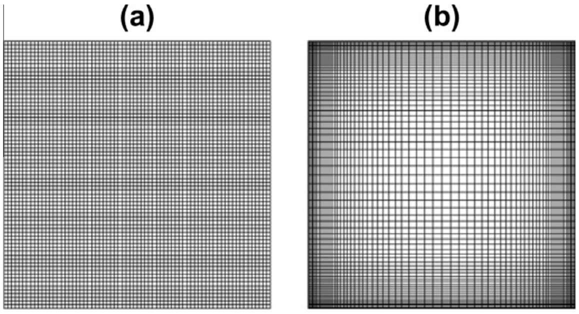

Fig. 5. Mesh at inlet boundary condition (a) uniform mesh resolution over the cross-section of the wind tunnel (b) refined mesh in the near wall regions.

and, thus, a linear interpolation to the boundary value on the side with $\langle U_i \rangle = 0$ would introduce an unrealistic wind profile. This is confirmed by the inlet profile measurements (Fig. 4) which indicate strong deviations from a linear wind profile in this region. Moreover, test simulations with linear interpolated values towards the walls lead to a secondary flow near the ground wall of the tunnel, which introduced strong turbulence and negatively affected the velocity profile up to $z \approx 0.35$ m. Thus, the analytical mean velocity profile could not be used to model the extrapolation region at the inlet.

To overcome the problems of extrapolation, the velocity slope for $0.01 < z < 0.05$ m was derived from the mean velocity profile at the inlet, Fig. 4. Subsequently, the gradient function was used to extrapolate from the measured region to grid points located between 0.01 and 0.05 m from the walls. Between the walls and 0.01 m a linear interpolation was used. This scheme was used for the ground and side walls but not the "upper zone" (Fig. 2). In this area, the missing values were modeled using linear interpolation between the outer measurement grid points and the wall value $\langle U_i \rangle = 0$, because the velocity distribution behind the baffle plate tends to zero. Fig. 6 shows the interpolated inlet mean velocity field.

The inlet wind velocity field shows velocity gradients towards all boundaries, except the upper area above 0.4 m where the influence of the baffle plate is dominant. Up to a height of 0.3 m, the

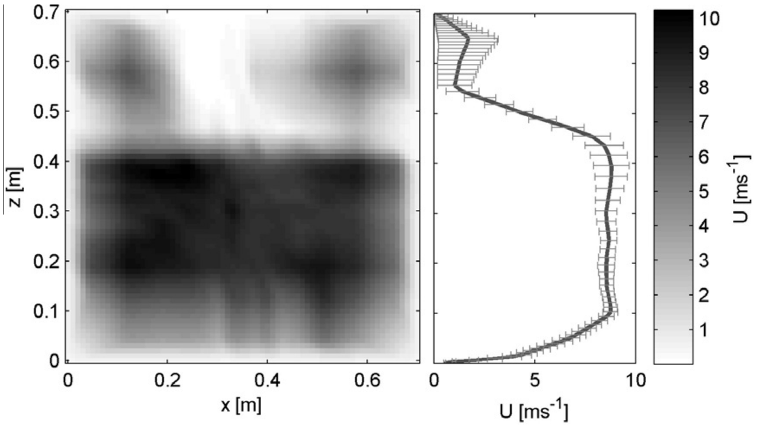

Fig. 6. Surface plot for the inlet velocity boundary condition at the beginning of the flow chamber. The errorbars in the right plot indicate the variability of the wind speed in various depth for 0.1 > *x* > 0.6 m.

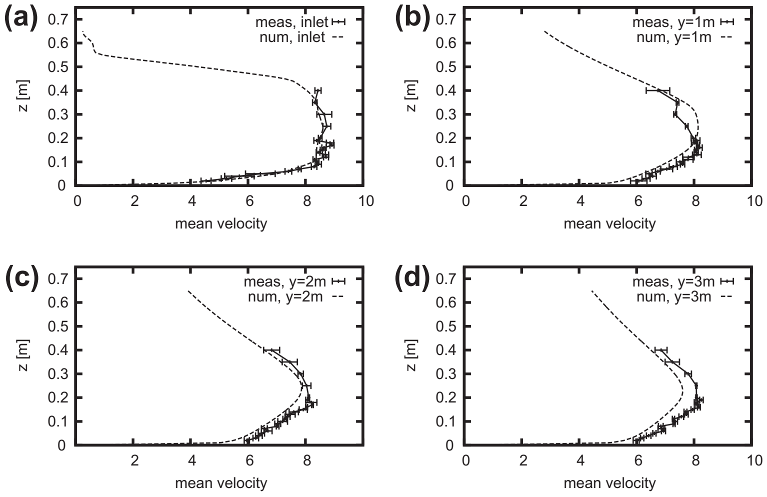

Fig. 7. Velocity profiles for (a) inlet, (b) *y* = 1 m, (c) *y* = 2 m and (d) *y* = 3 m after the inlet boundary condition.

error bars show a standard deviation of less than 1 m/s, above the deviation further increases to values higher than 2 m/s. The two areas with higher wind velocities in the upper part are caused by parts of the airflow that bypassed the blend on each sides. The low deviations of the velocity in the lower section of the wind tunnel show the effectiveness of the velocity rectifier elements before the inlet surface to the wind tunnel chamber. So a wide cross section with a uniform velocity field could be obtained.

The CFD calculations were performed with the k–ϵ model and the SIMPLE algorithm for the velocity-pressure coupling. The standard deviation of the measurements were used for the TKE values at the inlet boundary conditions according to Eq. (19)

$$k_{\text{boundary}} = \frac{1}{2} \cdot U^2_{stdDev} \tag{19}$$

The inlet dissipation field was estimated based on the TKE values at the inlet according to Eq. (20)

$$\epsilon_{\text{boundary}} = \frac{k^{3/2}}{L_t} \tag{20}$$

with the length scale L_t = 0.7 m for the inlet dimension of the wind tunnel (ANSYS, 2006).

4.3. Wind field modelling

A very good agreement of the modeled wind profiles with the measured data was found throughout the length of the tunnel. The root-mean-square error between the values predicted by the model and the measured data varies around 0.5 ms^{-1} and visual comparison of the velocity profiles (Fig. 7) suggests that the CFD simulations were able to reproduce the modification of the velocity profile along the flow chamber. The influence of the flow configuration by the baffle plate in the upper zone (Figs. 2 and 5) is captured well by the simulations.

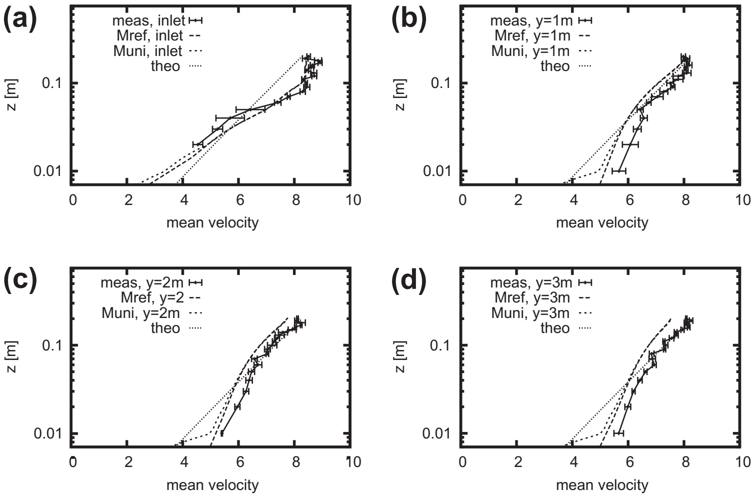

Fig. 8. Velocity profiles for 0 < z < 0.2 m for (a) inlet, (b) y = 1 m, (c) y = 2 m and (d) y = 3 m after the inlet boundary condition. Mref shows the results with the refined mesh, Muni with the uniform mesh and theo the theoretical profile from Eq. (14).

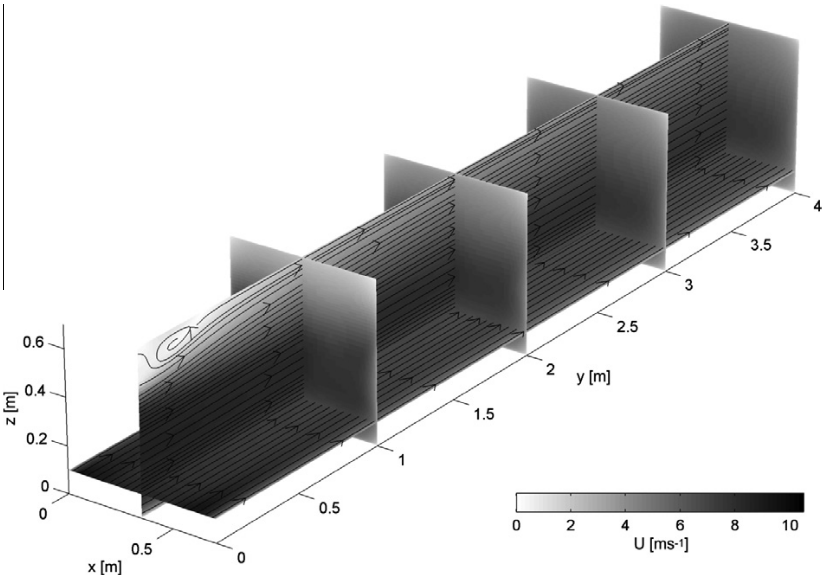

Fig. 9. Velocity profile and stream lines in the wind tunnel as calculated by the CFD simulation. Slices through the 3D wind field are shown at x = 0.35 m, y = 1, 2, 3 and 4 m, z = 0.1 m.

As discussed in Section 4.1 the profiles have two distinct flow regions. As can be seen in Fig. 8 the CFD simulations were able to reconstruct both flow regions appropriately. The profiles with the uniform mesh in Fig. 8 (Muni) are forced in the lowest element (below $z = 0.01$ m) to the value of the theoretical profile Eq. (13), where as the refined Mesh (Mref) is sufficient fine to resolve the flow for $z < 0.1$ m.

The results from the refined mesh are in slightly better agreement with the measured velocity profile. The effort for creating a denser mesh in the near wall regions is compensated by a better representation of the strong velocity gradients in this part of the domain with the k–ϵ turbulence model.

The velocity pattern in the wind-tunnel chamber features a back-flow in the stagnation area in the upper part next to the inlet boundary (Fig. 9). These flow patterns introduce turbulence due to the strong velocity gradients between the high velocity in the middle of the tunnel and the slower back-flowing part in the "upper zone" where a rotating vertex develops. This disturbance can be tracked until the end of the wind tunnel.

The measurement data can be used to validate the spatial accuracy of the simulations. The measurements and numerical results were re-sampled to the refined grid with $\Delta x = \Delta z = 0.07$ m resolution using linear interpolation. The relative error was then obtained using Eq. (21)

$$\eta_{\mathrm{rel}} = 100 \cdot \frac{U_{\mathrm{CFD}} - U_{\mathrm{meas}}}{U_{\mathrm{meas}}} \tag{21}$$

where U_{CFD} and U_{meas} are the simulated and measured wind velocities, respectively. Irrespective of higher errors towards the corners of the spatial domain, a good agreement between surface measurements and simulated data is obtained (Fig. 10).

4.4. Turbulence characteristics and shear stress

The experimental quantification of turbulence characteristics and wall shear stress is extremely difficult and nearly impossible if characterization of spatial patterns is required since measurements are often labor and time consuming and measurement devices may influence the wind field. In most studies, shear stress is calculated from wind profile measurements. Because of their difficulty studies that really measure shear stress are rare and usually lack the spatial differentiation (Walker and Nickling, 2003). Such data, however, is needed to assess the spatial variability of wind erosion rates and can be obtained from CFD simulation results

$$I = \frac{\sqrt{\frac{2}{3}k}}{U} \tag{22}$$

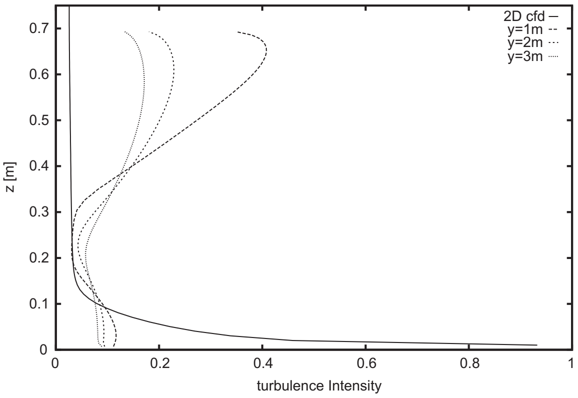

Fig. 11. Intensity profiles at inlet and 1, 2 and 3 m behind the inlet boundary condition and the ideal intensity profile derived from a two-dimensional calculation with the same conditions.

A measure that characterizes turbulence is the turbulence intensity I (Eq. (22)), which is calculated as the ratio between the TKE and mean velocity (Pope, 2000). The vertical turbulence intensity in the higher part ($0.5 < z < 0.7$ m) along the tunnel chamber largely reflects the turbulence induced by the vortex behind the baffle plate as can be seen in Fig. 11. When compared to an ideal boundary layer intensity profile, turbulence intensity as derived from the CFD simulations shows significant deviations near the ground and in the upper part of the tunnel. While the turbulence intensity near the ground is decreased, the turbulence induced by the baffle plate increases the turbulence intensity above 0.3 m compared to an ideal boundary layer. A good accordance was found between 0.1 and 0.3 m.

Detached particles or water droplets can be influenced in different ways by the turbulent characteristics (Pruppacher and Klett, 1997). In atmospheric flows the turbulence properties, in the case of k–ϵ model results, the TKE can influencing the trajectories of particles (Gorlé et al., 2009). Because the TKE level in the channel is based on the standard deviation of 1 Hz measurements, the numerical results have to be interpreted carefully. Nevertheless, the deviations from the ideal boundary layer can be expected to influence results gained by experiments with particle detachment and rainfall simulations.

Fig. 12 shows the relative deviation of the wall shear stress on the ground wall of the wind tunnel from the shear stress of the ideal logarithmic profile obtained from a two-dimensional calculation. The plot has to be interpreted critically due to the problems

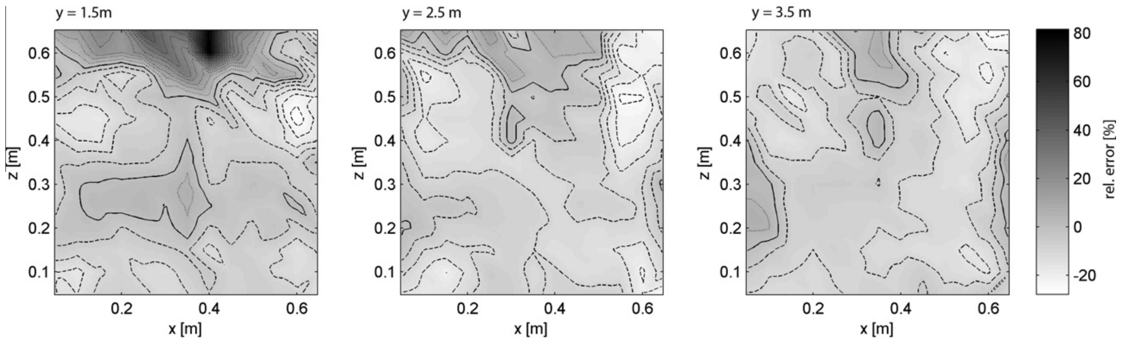

Fig. 10. Surface and contour plots of the relative error (Eq. (21)) of the simulated wind velocities in 1, 2, and 3 m distance behind the opening to flow chamber. Contour lines are drawn at 5% distances. The solid line indicates the 0% contour, dotted and dot-dashed contours represent positive and negative errors, respectively. The spatial extend of the figure is limited on the area covered by measurements (see Fig. 2).

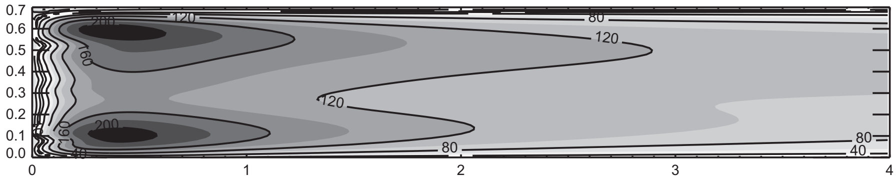

Fig. 12. Contour plot of the relative deviation [%] of the wall shear stress distribution on the ground from the shear stress of an ideal boundary profile derived from a two-dimensional calculation.

associated in defining the boundary conditions and the lack of validation data mentioned above. Nevertheless, it is one of few options to obtain an impression of the spatial distribution of shear stress on the surface and provides valuable information for analyzing experimental results of e.g. transport phenomena.

The inlet velocity profile introduces a characteristic distribution of the wall forces (Fig. 12). In the region near the inlet, two areas developed symmetrically spread around the central axis of the wind tunnel. The constant geometric properties and the adjustment of the wind field to the boundary conditions lead to a more homogeneous wall shear stress in the second half of the tunnel. The increased wall shear stress on the left hand side (in flow direction) of the tunnel can be used to explain higher erosion rates on this side during field measurements, which will be considered in detail in the next section.

4.5. Particle transport

Experiments on particle detachment and transport conducted with the wind tunnel detected a distinct bias of sediment transport towards the left side (Figs. 3 and 13b). This pattern agrees well with the lateral distribution of wind velocity and turbulent kinetic energy (Fig. 13a). Together with the shear stress distribution on the ground (Fig. 12), these data provides an explanation for the unsymmetrical transport of the material and inherent bias in the tunnel.

The reason for the observed asymmetric shear stress lies in the production of the wind by the fan. It produces not homogeneous wind conditions over the whole length of the propeller. Instead, we observe a velocity increase from the hub of the propeller to about three quarters of the propeller length. Further outside the velocity is again reduced. Although the wire mesh in front of the honeycomb and the honeycomb reduces this effect significantly, it is still weakly preserved. The highest erosion rates can be expected at the position of the wedge traps. This effect has an important influence when calculating the mean erosion rate for the tunnel. In contrast, at the position of the MWAC Samplers, we would expect a reduced erosion rate due to the reduced shear stress.

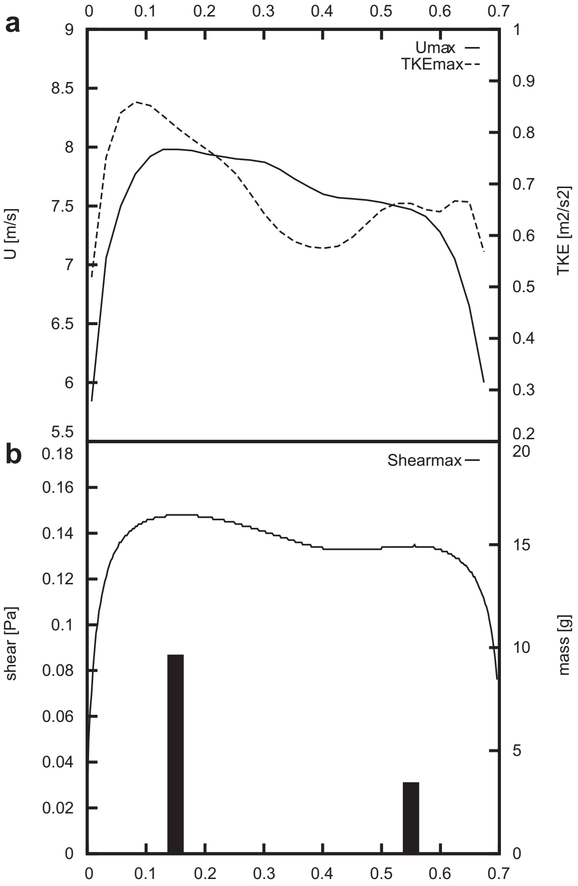

Fig. 13. Lateral profiles of maximal velocity and turbulent kinetic energy along the channel (a) and the maximal shear stress along the channel with measured transported material (b).

4.6. Saltation and suspension

By solving Eq. (18), the critical particle diameter can be obtained to distinguish areas in the tunnel where saltation and suspension prevails. The expression can be numerical evaluated on the ground of the channel as function of shear stress.

Fig. 14 shows the diameter for which particles with higher diameters are in saltation and creep. Particles with smaller diameters are suspended. Based on the method, the pattern follows very clearly the shear stress pattern. The pattern shows only minor spatial variability in the micrometer range (34–40 μm) and suggests a homogeneous spatial distribution of the governing transport processes in the tunnel. The observed processes are the same all across the ground with a distinction of grain size of approximately 40 μm, which is very good for reproducibility and comparability of results of different soils. Particles larger than 40 μm are detached and transported as saltation, while smaller ones are transported as suspension. This leads to the conclusion, that the dominating transport mechanisms over the channel are, depending on soil texture, saltation and, for large particles, creep. These results show that the tunnel provides good conditions for detachment studies.

4.7. Geometrical modifications

The effort to change variables such as the geometry is less with CFD methods than it is to implement and test changes in practice. This gives the ability to perform modulations of the wind channel and the results can be used for planning further enhancements and modification of the wind tunnel. To examine the advantages of a longer channel on the evolution of the velocity profile, the channel

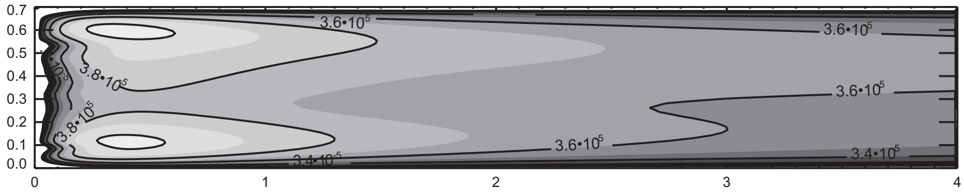

Fig. 14. Critical diameter for distinction of dust and sand according Eq. (18) on the ground.

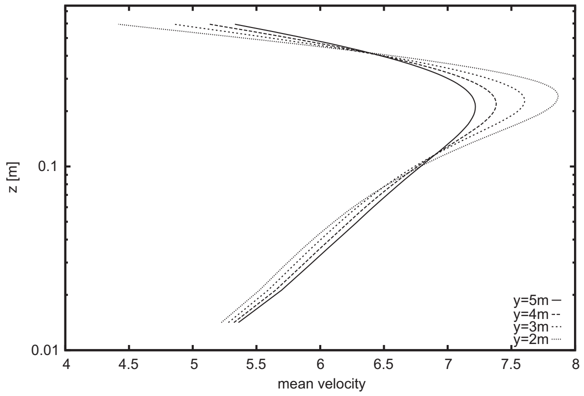

Fig. 15. Velocity profiles for 2 m, 3 m, 4 m, 5 m after the inlet condition for a prolongation of the channel to 5.5 m.

was extended to a length of 5.5 m and computed with the same boundary conditions. Fig. 15 shows the effect on the vertical velocity profiles.

It can be seen that the profiles mitigate along the channel but preserving the shape of the profile. The prolongation of the channel leads only to a linear mitigation of the magnitude and the low differences in the profiles would lead to the conclusion that an extension of the tunnel would not give any further improvement.

5. Conclusion

We conducted an in-depth analysis of the wind-field characteristics of a portable wind tunnel using CFD simulations. The tunnel's wind-field that was previously measured experimentally corresponds very well with the results obtained from the physically based CFD simulations. The numerical approach enables us to study the flow conditions in the flow chamber in great detail. Our analysis suggests that theoretical profiles for ideal boundary flows are not applicable to approximate the velocity evolvement along the experimental tunnel in sufficient accuracy. In addition, the CFD simulation results and derivatives provide an accurate method to explain secondary processes like particle detachment. Further it provides explanations for an observed bias in sediment transport in the channel and enables us to plan and implement future structural changes to the tunnel to reduce this bias.

Our results underpin the notion that a critical assessment of experimental setups is vital to transfer their findings to natural conditions and to compare them with data obtained by different setups. In addition our results lay the corner stone for further efforts and advances in simulating e.g. structural changes to the wind tunnel and its effects on the wind field. CFD can thus become a valuable and fast planning tool for rebuilding and improving the portable wind tunnel.

Accurate measurements of the wind field are extremely important to calibrate and validate such simulations and to provide reliable boundary conditions. CFD simulations can then be used to assess the spatial variations that can often insufficiently be covered by measurements and to derive variables such as shear stress and TKE that are very difficult to determine experimentally. CFD may thus be a valuable tool being complementary (Parsons et al., 2004) to but never separated from a measurement setup.

Acknowledgments

The authors wish to acknowledge Prof. Dr. J.B. Ries and Akad. Dir. Dr. R.-G. Schmidt for their cooperation and Miriam Marzen and Thomas Iserloh for their help with the measurements at the Institute of Physical Geography, Trier University, Germany. Construction and development of the wind and rainfall simulator was funded by the Deutsche Forschungsgemeinschaft (DFG), project Ri835/3. The second author was supported by a Ph.D.-scholarship provided by the state of Rhineland Palatinae (GraFöG). We thank Prof. Dr. Eberhard Parlow for his support for this publication. Further we thank the anonymous reviewers for the constructive critics and comments.

References

Alhajraf, S., 2004. Computational fluid dynamic modeling of drifting particles at porous fences. Environmental Modelling and Software 19, 163–170, Modelling of Wind Erosion and Aeolian Processes.

ANSYS, ANSYS CFD Reference Manual, 11.0 ed., ANSYS Inc., 2006.

Bauer, B., 2009. Contemporary research in aeolian geomorphology, Geomorphology 105, 1–5. Contemporary research in aeolian geomorphology – 6th International Conference on Aeolian Research (ICAR VI).

Blocken, B., Stathopoulos, T., Carmeliet, J., 2007. Cfd simulation of the atmospheric boundary layer: wall function problems. Atmospheric Environment 41, 238–252.

Fister, W., Iserloh, T., Ries, J.B., Schmidt, R.G., 2011a. Comparison of rainfall characteristics of a small portable rainfall simulator and a combined wind and rainfall simulator. Zeitschrift für Geomorphologie 55 (Suppl. 3), 109–126.

Fister, W., Iserloh, T., Ries, J.B., Schmidt, R.G. 2011b. A portable wind and rainfall simulator for in situ soil erosion measurements. Catena, in press.

Fister, W., Ries, J., 2009. Wind erosion in the central Ebro Basin under changing land use management. Field experiments with a portable wind tunnel. Journal of Arid Environments 73, 996–1004.

Fister, W.H., Schmidt, G., 2008. Concept of a single device for simultaneous simulation of wind and water erosion in the field. In: D.G.D., Cornelis, W., Eyletters, M., Hollebosch, P. (Eds.), Tagungsband der Conference on Desertification, 23.01.2008, Gent, Belgien, pp. 106–113.

Gorlé, C., van Beeck, J., Rambaud, P., van Tendeloo, G., 2009. Cfd modelling of small particle dispersion: the influence of the turbulence kinetic energy in the atmospheric boundary layer. Atmospheric Environment 43, 673–681.

Greeley, R., Blumberg, D.G., Williams, S.H., 1996. Field measurements of the flux and speed of wind-blown sand. Sedimentology 43, 41–52.

Hestenes, M.R., Stiefel, E., 1952. Methods of conjugate gradients for solving linear systems. Journal of Research of the National Bureau of Standards 49, 409–436.

Lane, S.N., 1998. Hydraulic modelling in hydrology and geomorphology: a review of high resolution approaches. Hydrological Processes 12, 1131–1150.

Menter, F.R., 1994. Two-equation Eddy-viscosity turbulence models for engineering applications. AIAA Journal 32, 1598–1605.

Murakami, S., Ooka, R., Mochida, A., Yoshida, S., Kim, S., 1999. Cfd analysis of wind climate from human scale to urban scale. Journal of Wind Engineering and Industrial Aerodynamics 81, 57–81.

OpenFOAM, OpenFOAM The Open Source CFD Toolbox – Programmers' Guide, version 1.6 ed., OpenCFD Ltd., 2009.

Parsons, D.R., Wiggs, G.F.S., Walker, I.J., Ferguson, R.I., Garvey, B.G., 2004. Numerical modelling of airflow over an idealised transverse dune. Environmental Modelling and Software 19, 153–162, Modelling of Wind Erosion and Aeolian Processes.

Pope, S.B., 2000. Turbulent Flows. Cambridge University Press.

Pruppacher, H., Klett, J., 1997. Microphysics of Clouds and Precipitation. Kluwer Academic Publishers.

Richards, P., Hoxey, R., 1993. Appropriate boundary conditions for computational wind engineering models using the k–ϵ turbulence model. Journal of Wind Engineering and Industrial Aerodynamics 46 (47), 145–153.

Salim, S., Cheah, S., 2009. Wall y+ strategy for dealing with wall-bounded turbulent flows. In: Proceedings of the International MultiConference of Engineers and Computer Scientists 2009, vol. II, Hong Kong.

Shao, Y., 2008. Physics and Modelling of Wind Erosion,, .. Atmospheric and Oceanographic Sciences Library, second ed. Springer Science + Business Media B.V.

R. Stull, Meteorology for Scientists and Engineers, G. Garloson, second ed., 2000.

Versteeg, H., Malalasekera, W., 1995. An Introduction to Computational Fluid Dynamics. Longman Scientific and Technical.

Wakes, S.J., Maegli, T., Dickinson, K.J., Hilton, M.J., 2010. Numerical modelling of wind flow over a complex topography. Environmental Modelling and Software 25, 237–247.

Walker, J., Nickling, W.G., 2003. Simulation and measurement of surface shear stress over isolated and closely spaced transverse dunes in a wind tunnel. Earth Surface Processes and Landforms 28, 1111–1124.

Weller, H.G., Tabor, G., Jasak, H., Fureby, C., 1998. A tensorial approach to computational continuum mechanics using object-oriented techniques. Computers in Physics 12, 620–631.

Wilcox, D.C., 2000. Basic Fluid Mechanics, DCW Industries.

Wilson, S., Cooke, R., 1980. Wind Erosion. Wiley.

Part IV.
CFD with gaseous pollutants

Andres Gartmann, Mathias D. Müller, Eberhard Parlow, Roland Vogt (2011)
Evaluation of numerical simulations of CO_2 transport
in a city block with field measurements,
Environmental Fluid Mechanics, in press, DOI 10.1007/s10652-011-9226-z

Environ Fluid Mech
DOI 10.1007/s10652-011-9226-z

ORIGINAL ARTICLE

Evaluation of numerical simulations of CO_2 transport in a city block with field measurements

Andres Gartmann · Mathias D. Müller · Eberhard Parlow · Roland Vogt

Received: 31 December 2010 / Accepted: 20 September 2011

Abstract Studying urban air-transport phenomena is highly complex, because of the heterogenous flow patterns that can arise. The main reason for these is the variable topology of urban areas, however, there is a large number of influencing variables such as meteorological conditions (e.g., wind situation, temperature) and anthropogenic factors such as traffic emissions. During a one-year CO_2 measurement campaign in the city of Basel, Switzerland, steep CO_2 gradients were measured around a large building. The concentration differences showed a strong dependency on the local flow regimes. Analysis of the field data alone did not provide a complete explanation for the mechanisms underlying the observed phenomena. The key numerical parameters were defined and the influence of turbulent kinetic energy dependency on the time interval for the Reynolds decomposition was studied. A Reynolds-Average Navier-Stokes Computational Fluid Dynamics (CFD) approach was applied in the study area and the CO_2 concentrations were simulated for six significant meteorological situations and compared to the measured data. Two flow regimes dependent on the wind situation, which either enhanced or suppressed the concentration of CO_2 in the street canyon, were identified. The enhancement of CO_2 in the street canyon led to a large difference in CO_2 concentration between the backyard- and street-sides of a building forming the one wall of the canyon. The specific characteristics of the flow patterns led to the identification of the processes determining the observed differences in CO_2 concentrations. The combined analysis of measurement and modeling showed the importance of reliable field measurements and CFD simulations with a high spatial resolution to assess transport mechanisms in urban areas.

Keywords CFD · CO_2 transport · Urban areas · Turbulent kinetic energy · RANS

A. Gartmann (✉) · M. D. Müller · E. Parlow · R. Vogt
Institute of Meteorology, Climatology and Remote Sensing, University of Basel,
Klingelbergstrasse 27, 4056 Basel, Switzerland
e-mail: andres.gartmann@unibas.ch

1 Introduction

Human activity in urban areas degrades air quality, which in turn strongly affects the quality of life and health of the population. Understanding the transport mechanisms of anthropogenic emissions from fossil-fuel combustion in urban areas is a key issue in assessing the impact of pollution and improving air quality. Heterogeneous flow patterns evolve in both space and time owing to the complexity of the topology in urban areas. The dispersion of pollutants is dominated by micro-scale wind patterns within the urban boundary layer [13]. The flow patterns lead to strong horizontal concentration gradients of air pollutants, greenhouse gases and particles [28]. CO_2 concentration can be measured and can be used as a substitute for combustion emissions, such as from traffic, in urban areas. Further assessment of the contribution to the global CO_2 cycle of the urban sources is challenging, as spatially significant measurement data in urban areas are difficult to obtain [9].

A better understanding of such air borne phenomena and the key mechanisms for the dispersion of pollutants in urban areas can be gained by different approaches.

Experimental studies with simple objects and numerical simulations such as data from wind-tunnel experiments have been used to evaluate numerical methods for turbulent simulations, such as Large Eddy Simulations (LES) or turbulent Reynolds-Average Navier-Stokes (RANS) models [7,15,4,6]. These methods help to develop and verify numerical models but the simplification of the geometry and the idealized flow conditions in experimental setups do not have the same relevance to real situations as do field measurements. Extensive field campaigns [9,20,28] provide data from point measurements that have high temporal resolution, but contain little information about the spatial properties of the flow. Finally, model studies with idealized city geometries have been utilized to study urban air-borne phenomena [12,21,1,27,11]. An overview of street canyon modeling is given by [24]. Numerical methods, such as computational fluid dynamics (CFD), are well-known instruments for computing and analyzing flow patterns [13]. Different studies have been conducted with idealized geometries and air pollution transport, [23], but only a few numerical studies used complex city geometries and field-measurement data to validate the numerical results [10, 29].

To capture transport dynamics of CO_2 distribution in a street canyon, a previous study measured CO_2 concentrations in a street canyon in Basel, Switzerland, and in an adjacent backyard. The result showed a large difference in CO_2 concentration between the front (street-side) and back of a large building that constituted part of the canyon wall. The CO_2 concentration differences were strongly dependent on wind direction and only weakly dependent on traffic frequency and atmospheric stability [26].

This article describes the numerical approach and the comparison of CFD CO_2 results with field measurement data in a real city geometry. Basic guideline exists for CFD calculations in urban areas, e.g., [8] or [22]. Based on these guidelines, a sensitivity study was first conducted to determine the numerical parameters that influence the calculations. An appropriate time-average period for the Reynolds decomposition in the measurement data had to be defined for the comparison of RANS models with field measurements. This was achieved in other studies by minimizing the error between modelled and measured data through reducing the length of the Reynolds decomposition time-average period, e.g., [5]. The length of the Reynolds decomposition time-average period has a significant influence on the turbulent kinetic energy (TKE) in street canyons. The influence of time-average periods on the velocity and turbulence profiles in a street canyon was analyzed in detail using field data of the Basel Urban Boundary Experiment (BUBBLE) [20].

Six representative wind flow conditions were modeled with the results from the sensitivity analysis and the CO_2 field-measurement data analysis. These were compared to the measurement data to study the mechanisms in detail and to address the reason for the strong dependency of the CO_2 concentration differences on wind condition.

This article shows the application of CFD in a complex city geometry and the comparison to field measurements, whereby the ability of CFD methods to obtain flow characteristics and transport phenomena of fluid components within real urban areas was shown. Further, it shows the influence of, and gives recommendations for, the definition of the time-average period for the Reynolds decomposition of the field measurements in comparison to RANS results.

2 Methods

2.1 Measurements

Two measurement data sets used for this study were obtained at two sites in the city of Basel, Switzerland. Figure 1 shows the center of Basel with the locations of the two sites (A,B).

2.1.1 Sensitivity analysis

Field-measurement data of the Basel Urban Boundary Experiment (BUBBLE) [20] were used for the sensitivity analysis. During the one year BUBBLE campaign, a measurement tower was located within a street canyon in a densely built-up area of the city of Basel, Fig. 1a. Wind fields were measured on six levels using sonic anemometers with a time resolution of 20 Hz. This measurement setup provides an ideal framework to evaluate the performance of solvers and numerical parameters for CFD calculations in a complex topology.

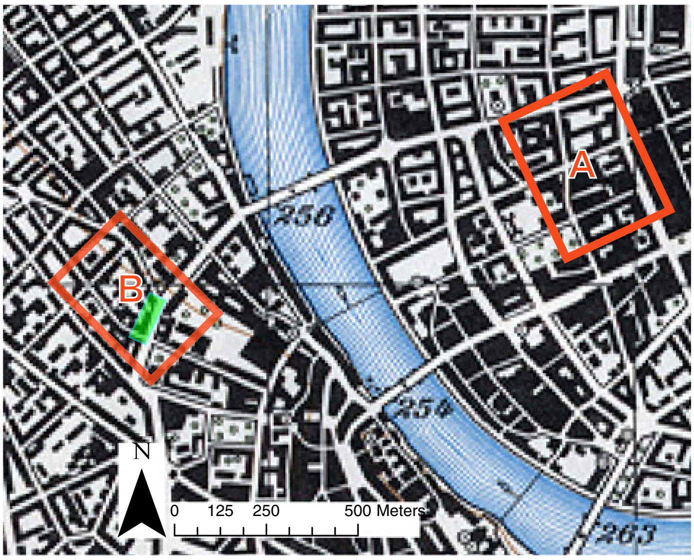

Fig. 1 Location of the two study sites in Basel, Switzerland. *A* indicates the computational domain for the sensitivity analysis. *B* the location for the CO_2 transport simulations. The green shaded area in *B* indicates the building shown in Fig. 2. Base map copyright GVA BS, 25102002

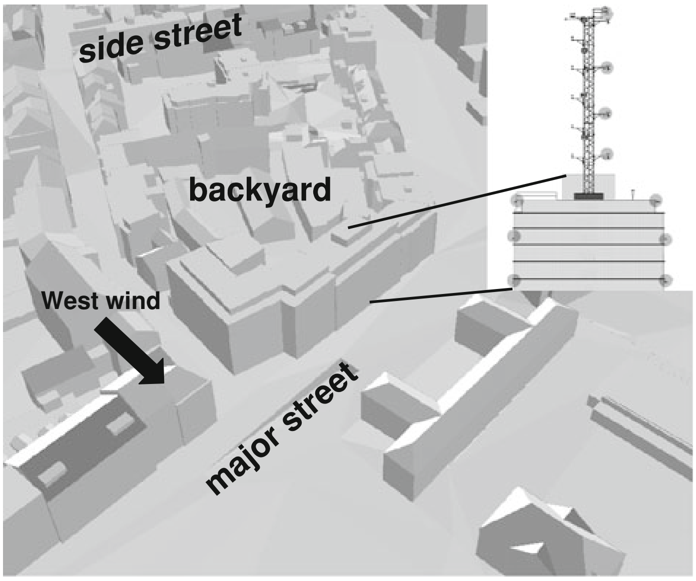

Fig. 2 Schematic view over the measurement site and cross section through the measurement setup (adapted from [26])

2.1.2 CO_2 *dispersion*

Figure 2 shows the area and the large 20 m high building (indicated as site B in Fig. 1), located in the center of Basel, Switzerland, as a computer-aided design (CAD) model. A main street with North-South orientation and heavy traffic runs in front of the building and at the rear of the building there is a large backyard surrounded by smaller buildings. CO_2 measurements were carried out around the building from September, 2004 to August, 2005. A closed-path gas analyzer (Li6262, LiCOR) and a multiplexer system with 10 inlets were used to measure the CO_2 concentration at 4, 15 and 21 m above the ground on each side and at 25, 28.5, 34 and 40 m over the top of the building on a measurement tower.

The concentration profiles were averaged over 30 min intervals. The detailed configuration can be seen in the schematic view, where the dots represent the inlets for the CO_2 measurements, inset Fig. 2. The stationary measurement tower on top of the building was also equipped with an eddy covariance system. The streets adjoining the other side of the smaller buildings are sidestreets with less traffic. The two dominant wind directions over the region are from West, indicated by the arrow, and East [20].

2.2 Numerical modeling

2.2.1 Governing equations

The turbulent wind field in urban areas are strongly influenced by the heterogeneity of the topology. For this reason, stability has a minor influence within the lower urban boundary layer [14]. This allows the simplification of neglecting buoyancy and thermal effects, which is applicable for advection dominant flows. Following [25], the Navier-Stokes equations (NSE) for incompressible fluid flow can be written as:

$$\frac{DU_i}{Dt} = -\frac{1}{\rho}\frac{\delta p}{\delta x_i} + f_i + \mu\frac{\delta^2 U_i}{\delta x_j^2} \tag{1}$$

where U_i are the velocity components in three dimensions, ρ the density, f_i body forces, p the pressure and μ the viscosity of the fluid [25]. Together with the incompressible continuity equation

$$\frac{\delta U_i}{\delta x_i} = 0 \tag{2}$$

the NSE build the governing equations for CFD simulations. By applying the Reynolds decomposition

$$U_i = \langle U_i \rangle + u_i \tag{3}$$

on the NSE, Eq. 1, one of the most applied turbulent model approaches, the Reynolds-Averaged Navier-Stokes (RANS), Eq. 4, is obtained [18].

$$\frac{\bar{D}\langle U_i \rangle}{\bar{D}t} = -\frac{1}{\rho}\frac{\delta \langle p \rangle}{\delta x_i} + f_i + \nu \frac{\delta^2 \langle U_i \rangle}{x_i^2} - \frac{\delta \langle u_i u_j \rangle}{\delta x_j} \tag{4}$$

where ν is the kinematic viscosity $\nu = \mu/\rho$. The additional terms $\frac{\delta \langle u_i u_j \rangle}{\delta x_j}$ are the Reynolds stresses and increase the number of unknown variables to more than four. The Reynolds stresses have to be obtained by other assumptions, which is called the closure problem [18].

One way to solve the closure problem is through models using the viscosity hypothesis [18]. The turbulent-viscosity hypothesis introduces a proportional relation between the Reynolds stresses and the mean rate of strain using a scalar coefficient, the turbulent viscosity ν_t

$$\langle u_i u_j \rangle = \frac{2}{3} k \delta_{ij} - \nu_t \left(\frac{\delta \langle U_i \rangle}{\langle x_j \rangle} + \frac{\delta \langle U_j \rangle}{\langle x_i \rangle} \right) \tag{5}$$

where k is the turbulent kinetic energy. Two-equation models, where the $k - \epsilon$ model is one of the most applied approaches, solve for the TKE k and the dissipation ϵ each an additional transport quation [18]. Thus, the turbulent viscosity can be obtained from:

$$\nu_t = C_\mu \frac{k^2}{\epsilon} \tag{6}$$

where $C_\mu = 0.09$ is a model constant [18]. A good overview of other two-equation approaches can be found in [16].

A multicomponent flow approach was used for the simulation of the CO_2 dispersion. In multicomponent simulations the fields are computed only for a single fluid based on the governing equations. The fluid is considered as a mixture of single fluids in order to incorporate the influence of the different fluid components. The properties of the mixture in each cell is dependent on the proportion of each component in the cell. The proportion of each component in the domain can be calculated using a separate continuity equation for each component k:

$$\frac{D\tilde{\rho}_k}{Dt} = \frac{\delta \tilde{\rho}_k}{\delta t} + \frac{\delta (\tilde{\rho}_k \tilde{U}_i)}{\delta x_i} = -\frac{\delta}{\delta x_i} \left\{ \rho_k (\tilde{U_{ki}} - \tilde{U}_i) - \overline{\rho_k u_i} \right\} \tag{7}$$

where $\sim$ indicates the mass-average and $\tilde{U_{ki}}$ the mass-averaged velocity of the fluid of component k [2]. The relative mass flux term $(\tilde{U_{ki}} - \tilde{U}_i)$ models the motions of the single components in the mixture. The primary effect for these motions are the concentration gradients, which lead to relative motions in form of diffusion of the components in the mixture. The physical influence of the component is incorporated using the kinematic diffusivity D_k.

The turbulent fluxes $\overline{\rho_k u_i}$ can be modeled using the eddy dissipation-assumption, which leads to a advection-diffusion equation for the fraction Y_k:

$$\frac{\delta(\bar{\rho}\tilde{Y_k})}{\delta t} + \frac{\delta(\bar{\rho}\tilde{U_i}\tilde{Y_k})}{\delta x_i} = \frac{\partial}{\partial x_i}\left\{\frac{\partial Y_k}{\partial x_i}\left(\rho_k D_k + \frac{\mu_t}{Sc_t}\right)\right\} \tag{8}$$

where Sc_t is the turbulent Schmidt number $Sc = \nu_t/D$. If all continuity equations (Eq. 7) are summed, the standard continuity equation can be obtained (Eq. 2).

2.2.2 Setup

The commercial software package ANSYS CFX [2] was used for all CFD calculations. The buildings within 150 m of the CO_2 measurement location were included in the CFD computations. The meshes were constructed with the package ANSYS ICEM CFD [3]. All numerical simulations were steady-state simulations.

For the ground and building walls, smooth wall-functions were applied because the roughness influence would be of a smaller order than the resolved scales and a slip condition was set for the top of the domain, which ensured a parallel flow at the top of the boundary [8].

The CO_2 dispersion was modeled using a multicomponent approach. The simulated mixture was given the gaseous fluid properties of air, CO_2 and N_2 as a constraint. The mass fraction of air and CO_2 is computed according Eq. 8, with the mass fraction of N_2 as residual to ensure unity in every cell. The influence of the CO_2 traffic source was modeled as a surface source term with constant fluxes from the streets. Different source strengths had to be defined, because of the irregular traffic frequency on the main street (average 800–1200 vehicles per hour) compared to the smaller streets ($<$ 400 vehicles per hour). For weekend situations, the source strengths on the streets were reduced by half, due to lower traffic density. Six conditions were modeled (three westerly wind and three easterly wind situations) for the comparison and the analysis of the experimentally determined CO_2 characteristics. The numerical parameters as mesh resolution, boundary conditions and turbulence closure for the CO_2 CFD calculations were defined based on the results of a prior sensitivity analysis.

2.3 Sensitivity analysis

The influence of the numerical parameters of the applied CFD code was evaluated because the evaluation of CFD calculations should be based on high resolution measurements [17]. The domain for the validation cases had a spatial extent over 200 m in both horizontal directions within a densely built-up area. The vertical extent was 80 m and the maximal height of the buildings in the model domain approx. 20 m.

The following numerical parameters were tested with the applied numerical CFD code: (1) mesh, (2) turbulence model, (3) boundary condition, based on the general guidelines for urban CFD calculations [8,22]. All results were compared to the mean velocity and the TKE measurement profiles to obtain their performance.

1—Mesh: Four meshing methods with different complexities were tested using cell-size resolutions between 0.8 m and 4 m: (A) Plain tetrahedral, (B) tetrahedral with prism layers around walls, (C) tetrahedral with prism layers around walls and hexahedral shapes in the free stream regions, (D) cartesian [3].

The advantage of tetrahedral meshes (A, B, C) is their ability to represent the geometrical data more or less independently of the resolution [25]. Although dependent on mesh resolution, Cartesian meshes (D) result in simplification of the geometrical data. Tetrahedral meshes can produce elements with poor aspect ratios [22]. Changing distances of the first mid-point to surface elements can be prevented in (B) by adding prism layers near surfaces. Hexahedral element shapes introduce smaller errors and have a better iteration convergence [8], which was tested by adding hexahedral, rectangular shapes in the free stream region (C).

The plain tetrahedral meshes show poor results near walls because of the changing distances of the element midpoints to the wall surfaces. This leads to changes in the y^+ value (dimensionless distance from the wall), which is a key value for the necessary wall-functions [2]. The strongest correlation with the measured profiles was achieved using a minimum of three prism cell layers around walls. The additional hexahedral elements in the free stream regions had a minor influence on the results and only small effects on the divergence properties of the computations. In contrast to the tetrahedral meshes, the Cartesian meshes rendered poor results for the wind patterns within the street canyon.

The best results were found using tetrahedral meshes with approximately 1 m resolution and a minimum of three prismatic layers around walls.

2—Turbulence Model: Both the standard $k-\epsilon$ model and the RNG $k-\epsilon$ model were tested, because the widely used $k-\epsilon$ turbulence closure for RANS calculation has limitations due to the overproduction of kinetic energy in regions with stagnated flow situations [8]. However, the direct comparison of computations using the RNG $k-\epsilon$ approach and the standard model, showed no significant difference in this case.

3—Boundary Conditions: Uniform inlet conditions as well as logarithmic profiles were tested. For the logarithmic inlet profiles of the mean velocity $U(z)$ Eq. 9, as suggested by [19], was applied in combination with the friction velocity U_{fric}

$$U(z) = \frac{U^*_{fric}}{\kappa} \cdot \ln\left(\frac{z+z_0}{z_0}\right) \tag{9}$$

$$U^*_{fric} = \frac{\kappa \cdot U_h}{\ln\left(\frac{h+z_0}{z_0}\right)} \tag{10}$$

The reference mean velocity U_h is the velocity at a reference altitude over ground h, z the vertical distance, z_0 is the roughness length and κ the von Karman constant. For the sensitivity analysis, the reference height to calculate the friction velocity U^*_{fric}, the height above ground of the highest measurement point was used ($h = 32\,\text{m}$).

For the TKE k and the dissipation ϵ, two approaches were tested: (A) as suggested by [19] a constant TKE value k is derived from the friction velocity

$$k = \frac{U^{*2}_{fric}}{\sqrt{C_\mu}} \tag{11}$$

where C_μ is the model constant for the k- ϵ model ($C_\mu = 0.09$) and the dissipation ϵ is computed according:

$$\epsilon = \frac{U^{*2}_{fric}}{\kappa \cdot (z+z_0)} \tag{12}$$

The second approach (B) relates k to the turbulence intensity I and the mean velocity U:

$$k = \frac{3}{2} \cdot U^2(z) \cdot I^2 \tag{13}$$

and also dissipation:

$$\epsilon = \frac{k^{\frac{3}{2}}}{L_t} \tag{14}$$

where L_t is a characteristic length scale. Following [18] and [2] the vertical extension of the domain of 80 m was used.

3 Results and discussion

The time-average period for the Reynolds decomposition of the measured data had to be specified before the field measurements could be compared to velocities from RANS models.

3.1 Time-average period

Figure 3a shows the correlation between measured mean velocity V_{mean} and the TKE values for time-average periods of 1200 s and (b) 30 s for the same data set of July and August, 2002 in the street canyon, where the sensitivity analysis was conducted.

A strong dependency between time-average periods used for the Reynolds decomposition and the TKE values in the street canyon was observed. The ratio between the mean velocity and the TKE was significantly higher when longer time-averages (e.g., 1200 s) were applied compared to shorter time-averages (e.g., 30 s). This indicates that different time-averages lead to different ratios between the mean velocity and TKE. This is an important fact when RANS results are compared to measurement data, which is discussed in the next section.

Figure 4 shows the profiles for measured data with different time-average periods and the numerical results from the sensitivity analysis. The mean velocity values are only weakly influenced by the time-average periods, as can be seen in Fig. 4a. Figure 4b shows the influence of the time-average periods on the TKE distribution within the street canyon and the mean deviation, where the time-average period has a significant influence on the TKE profiles. For the mean velocity components, a good agreement between observations and model results was achieved, as can be seen in Fig. 4a. Using approach (A) for the turbulence entities leads to TKE profiles with higher TKE than with approach (B), Fig. 4b.

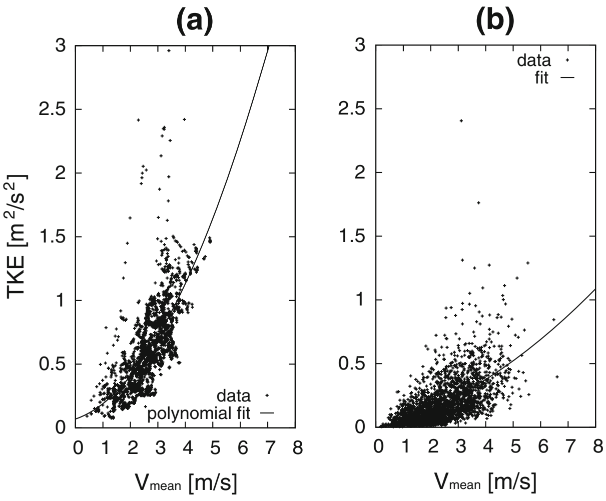

Fig. 3 Data points (+) represent the turbulent kinetic energy (TKE) magnitude at top of the tower (32 m above ground) and the *solid lines* represent the polynomial fit for Reynolds decomposition time-average periods of **a** 1200 s, **b** 30 s for SE wind angle (130°)

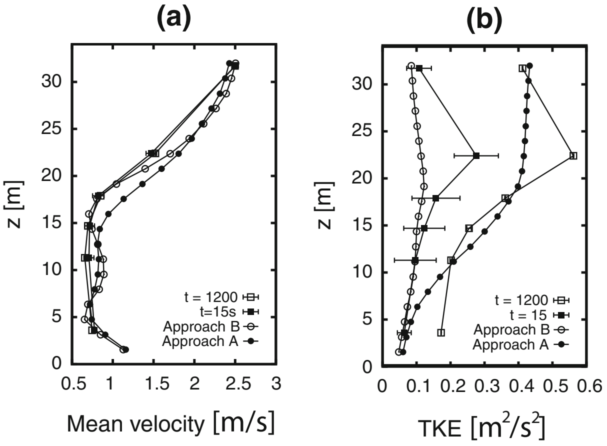

Fig. 4 Comparison between modeled data using Eqs. 11 and 12 (Approach A) or based on Eqs. 13 and 14 (Approach B) and measured data (time-average period for Reynolds decomposition 1200 and 30 s): **a** mean velocity, **b** TKE as profile from distance to the ground $z[m]$

A weak correlation could be found in the mean velocity profiles, using the approach with constant inlet turbulent values (A). Constant boundary conditions for TKE lead to comparable results for time-average periods of >600 s, but then to weaker correlations with mean velocity values, see Fig. 4. The best results were found with the boundary conditions (B) for the TKE ($I = 5{-}10\,\%$) together with time-average period of 15–60 s for all studied conditions and over all six measured levels in the street canyon. The results are in good agreement with appropriate time-average periods described in another study [5]. The better accordance between the CFD results and the measurements on all six levels using over two months of 20 Hz measurement data for the analysis indicated that there is an optimal average-time period for comparison. Other studies found the same appropriate time-average periods. Therefore, the use of 15–60 s for the Reynolds decomposition of field measurements in street canyons can be recommended for the comparison to RANS results. Because a defined time-average period does not exist for the Reynolds decomposition in RANS models caused by the model assumptions, the time-average period is not to be considered as the time-scale for the TKE. Generally, long time-average periods are associated with large spatial scale eddies. It is possible that, owing to the high spatial resolution in the model, explicitly resolved turbulence (as advection in the CFD results) is accounted as TKE in measurements. Further, an assumption for the Reynolds decomposition is the statistical stationarity of the flow. In urban areas the stationary condition for the Reynolds decomposition is rarely fulfilled and the longer the time-average length is, the higher the probability that the assumption is not fulfilled.

Independent of the time-average period, the significant change in the TKE profile at roof level (approx. 20 m above ground) has a poorer correlation with the measurement data compared to the lower part of the canyon, Fig. 4. Neither of the applied models were able to adequately simulate the acceleration of the TKE. This might be due to either the model formulation or the limitation of an insufficient horizontal extent. No significant differences could be found by comparing simple uniform inlet conditions and logarithmic profiles, because the influence of the topology was significantly stronger than the influence of the boundary conditions in densely built-up areas. Nevertheless the logarithmic profiles are recommended.

3.2 CO_2 concentration simulations

The measured CO_2 concentrations showed large differences between the street and backyard profiles, with a strong dependency on wind direction [26]. During westerly wind flow, the

Table 1 30 min averaged velocity U_{mag} and background concentrations $c_{\mathrm{background}}$ measured at top of the tower during the six scenarios. Day stands for weekdays (WD) and weekends (WE) and the absolute wind direction (WDir)

nr	Day	Date	WDir	U_{mag}	$c_{\mathrm{background}}$
1	WE	03.07.2005–09:00	Easterly	1.38	408.7
2	WE	17.07.2005–11:30	Westerly	1.82	378.6
3	WE	23.07.2005–09:00	Easterly	1.75	401.3
4	WE	23.07.2005–11:00	Westerly	2.4	370.2
5	WD	28.07.2005–12:00	Easterly	3.11	383.5
6	WD	21.07.2005–10:30	Westerly	3.55	378.4

Table 2 Measurement and modeled differences between front and backyard CO_2 concentrations for weekdays (WD) and weekends (WE) for easterly and westerly wind situations at the six conditions

nr	Day	WDir	λ_{meas} [−]	λ_{cfd} [−]	η []
1	WE	Easterly	5.4	6.7	0.24
2	WE	Westerly	32.2	66.7	1.07
3	WE	Easterly	13.3	16.1	0.21
4	WE	Westerly	51.3	49.3	0.04
5	WD	Easterly	6.9	4.5	0.34
6	WD	Westerly	52.7	66.9	0.27

CO_2 concentration was much higher on the street side then on the rear side of the building. The concentration differences between the two sides of the building were negligible during easterly wind episodes. There was practically no dependency on stability conditions and only a weak dependency on traffic frequency. To involve the representative cases for one week, 3 days were modeled: one weekday, Saturday and Sunday. A westerly and an easterly wind case was included for each weekday type. To account for different velocities for each of the three westerly and easterly wind cases, different velocities based on the measurement point on top of the tower on the building were selected in the data. As discussed, the time-average period had a strong influence on the TKE distribution in a street canyon. As the averaging interval of the concentration profiles was at least 30 min, boundary conditions suggested by [19] were used and the average mean velocities of 30 min at top of the tower for the six situations were used as U_h in Eq. 10. Table 1 summarizes the six situations with the 30 min averaged velocities and the CO_2 concentration, which were used as background concentrations measured at top of the tower at 40 m above ground.

To compare the measured and the modeled results qualitatively, the concentrations on each side of the building are summed with the highest available temporal resolution of 30 min and then the difference λ between the front and backyard side were calculated according:

$$\lambda = \sum c_{i,front} - \sum c_{i,back} \tag{15}$$

where c_i expresses the concentration at 4, 15, respectivly 21 m above ground. Table 2 shows the concentration differences λ based on the measurements and the CFD computations. The relative error η was computed using:

$$\eta = \left| \frac{\lambda_{cfd} - \lambda_{meas}}{\lambda_{meas}} \right| \tag{16}$$

As can be seen in Table 2, a good correlation was found between the modeled results and the experimental data (relative error <30%). The variable dispersion of the CO_2 from the street to the measurement points (Fig. 2) were the main reason for the strong dependency of

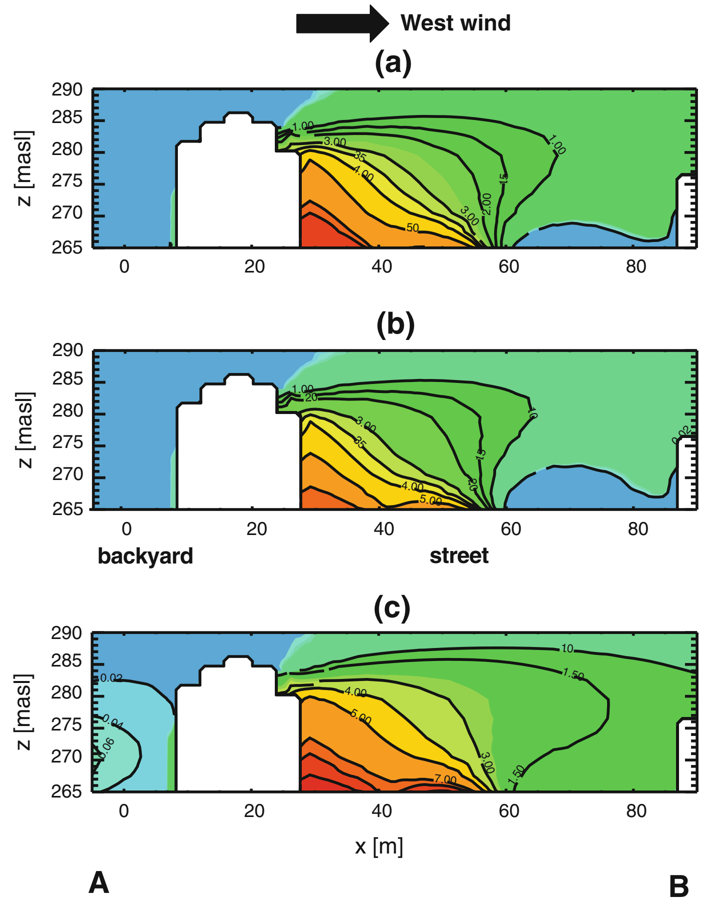

Fig. 5 Contour plot (location indicated in Fig. 8) of percentage of CO_2 relative to background concentration during westerly situations (Table 1) with following velocity magnitudes: **a** situation 2—$U_{mag} = 1.8$ m/s; **b** situation 4—$U_{mag} = 2.4$ ms^{-1}; **c** situation 6—$U_{mag} = 3.6$ m/s

the concentration differences between backyard and street. The good correlation between the measured and modeled differences of the CO_2 concentrations leads to the conclusion that the main characteristics of the flow patterns in the street canyon could be modeled in sufficient detail. The outlier on the weekend during the westerly wind episode might be due to higher traffic frequency or local irregular high emissions and could not be completely explained over that time period.

One of the advantages of CFD calculation is their spatial validity. The flow and corresponding CO_2 part in the fluid can be visualized and analyzed by using the CFD data.

The levels of the CO_2 layers could be visualized using the cross sections of the CO_2 mass part fields, representing the CO_2 concentrations. Figure 2 shows an overview of the site and Fig. 8 the location of the cross sections. Figure 5 shows the relative CO_2 concentration during westerly wind situations. The CO_2 from the street was transported towards the building wall in all three cases. A significantly higher CO_2 concentration (averaged 5 %) occurred on the western side of the street canyon (Fig. 5), whereas approximately the background CO_2 concentration was found on the eastern side.

One can see that the higher the velocity was, the more of the emitted CO_2 from the street was transported to the right area. Figure 6 shows the concentration levels during easterly wind situations, where a completely different CO_2 distribution was found. The CO_2 emitted from

Fig. 6 Contour plot of relative CO_2 concentration (% of background) during easterly situations with following velocities: **a** situation 1—$U_{mag} = 1.4$ m/s; **b** situation 3—$U_{mag} = 1.8$ m/s; **c** situation 5—$U_{mag} = 3.1$ m/s

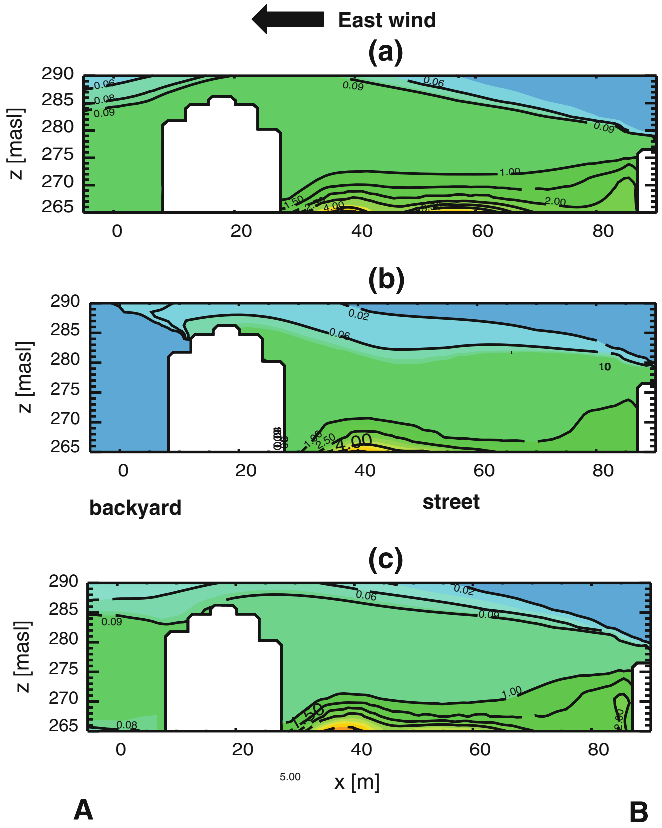

Fig. 7 Vector and contour plot: **a** westerly wind situation (Table 2—nr. 6) **b** easterly wind situation (Table 2—nr. 5). Contours describe magnitude of the velocity component normal to the plane shown in percentage

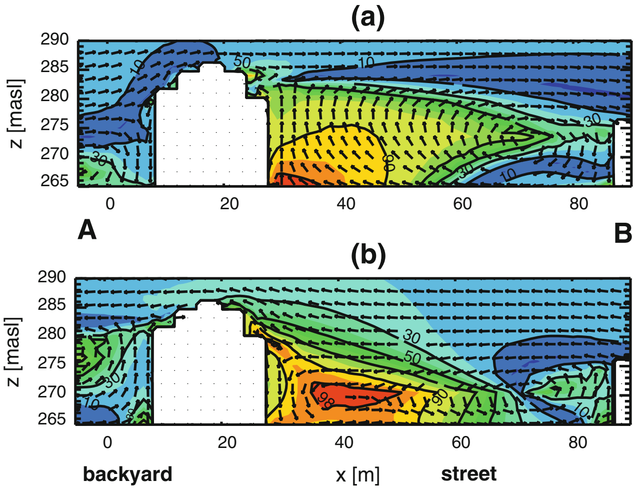

the street was not transported vertically, but concentrated close to the street level. Concentrations not higher than 1 % of the background can be expected near the left side of the street canyon. For all velocities, the CO_2 concentration field was more or less homogeneous in the area directly above the street. The cause of the concentration levels lies in the structure of the evolving flow patterns in the street canyon. Figure 7a shows a vector plot during westerly wind episodes, where the vectors show the projected velocity components on the cross section and the contour lines the percentage of the velocity magnitude of the components normal to the plane, Fig. 8. Figure 8 shows the three dimensional extent of the flow 5 m above the

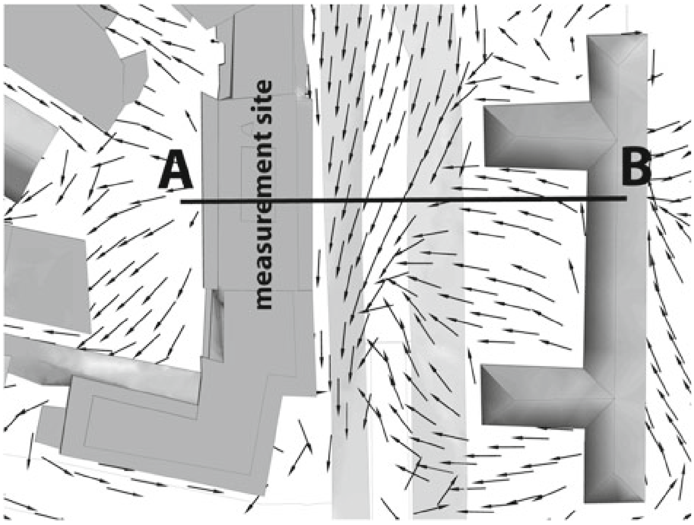

Fig. 8 Vector plot during westerly wind episode

ground and with A and B indicating the cross section showed in Fig. 5, 6, and 7, to explain the influence of the velocity components parallel to the street.

One vortex, rotating clockwise, was developed with a center point near the eastern building of the street canyon during westerly wind episodes, Fig. 7a. The flow near the ground had components orthogonal to the building wall on the left side, resulting in emitted CO_2 being transported towards the building wall. One prolate vortex was developed with the center point on the same height above the ground during easterly wind episodes, Fig. 7b. This counter-clock wise rotation transported the street CO_2 away from the building wall on the west side of the street.

Velocities evolved parallel to the building wall in the street canyon in both easterly and westerly wind episodes. As a result, the emitted CO_2 from the street was transported and concentrated along the street. CO_2 was transported to the measurement points by the combination of the velocity components vertical to the building wall, due to the vortex structures, and the components along the street.

Turbulence intensity is a measure of the ratio between the TKE and the mean velocity. By solving Eq. 13 to I (intensity), the turbulence intensity distribution over the street canyon can be visualized (Fig. 9). A higher intensity was found on the right side of the street canyon and lower intensity near the right building wall during westerly and easterly wind episodes. This indicates, that the TKE drove dispersion on the right side of the canyon, while the TKE had a lower impact on the CO_2 distribution near the measurement points on the left building wall. This supports the homogeneous CO_2 distribution during easterly wind episodes, where TKE counteracted to the transport effect of the counter-clockwise rotating vortexes. During westerly wind episodes the low turbulence intensity near the left building wall supported the acceleration of the CO_2.

The flow patterns are summarized schematically in Fig. 10. The dots on the left building wall indicate the points where the CO_2 measurements were made.

The separation line of the flow is defined by the height of the larger building (left side of the street canyon) during westerly wind situations. During easterly wind episodes, the separation line between the two flow patterns is defined by the level of the lower building (Fig. 10a). These two opposite vortex structures were the cause of the strong dependency of the CO_2 concentrations on the wind situations. The high mean velocity over the main street visible in Fig. 8 and indicated in the contours in Fig. 7 supported the accumulation of CO_2

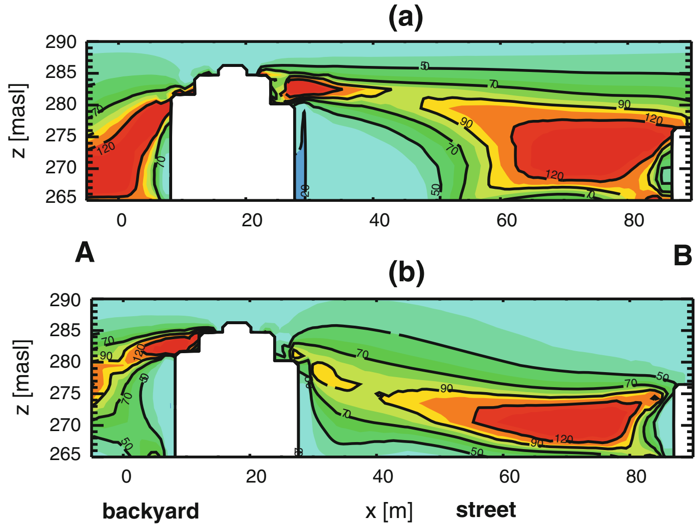

Fig. 9 Vector and contour plot with **a** westerly wind (Table 2—nr. 6), **b** easterly wind (Table 2—nr. 5). Contours describe turbulence intensity (Eq. 13)

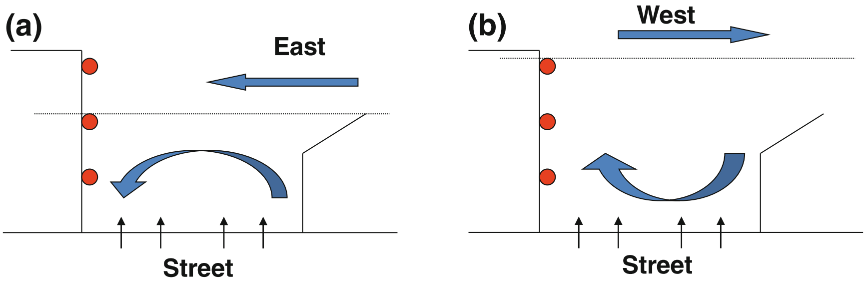

Fig. 10 Schematic flow patterns for **a** easterly and **b** westerly wind situations with measurement inlet points (*red*), separation lines and vortices that develop during wind situations

from traffic emissions along the street. The accumulated CO_2 was transported by the vortex towards the measurement inlet points, Figs. 8 and 10. In case of easterly wind, the CO_2 from the street was captured by the flow patterns in the low levels above the street and transported away from the measurement inlets by the counter-clockwise rotating eddies.

4 Conclusion

The results from the parametric study are in accordance with the recommendations for CFD calculations in urban areas [8,22]. The results show the ability of CFD to model complex flow patterns with highly heterogeneous geometry in very good agreement with high resolution temporal measurements in street canyons, where complex flow patterns can evolve. The evaluation with observation data leads to very good results for the mean velocity components within the complex study area. A strong dependency on the time-average periods of the Reynolds decomposition between the TKE values in a street canyon was found, which is an important aspect for comparing measurement data to RANS models results. Detailed analysis suggested that a time-average period of 15–60 s should be used for the Reynolds decomposition when comparing to RANS results in urban CFD calculations. This is similar to the time-average periods used in other studies. The validation of the computed TKE values also led to good results, except in the detached flow regions at roof level.

This case-study demonstrates the usefulness of CFD methods in analyzing and simulating realistic flow patterns in urban areas based on a comparison with a dependent quantity (CO_2 concentration) that is a proxy for air pollution. The accuracy of the numerical approach to capture the CO_2 transport is shown by the comparison with the field data. Computation of the spatially distributed CO_2 concentrations led to a conclusive explanation for the strong dependency on the wind direction of measured CO_2 differences around a building. Completely different concentration profiles were found depending on the wind conditions in the street canyon. This shows that, in real urban areas, the concentration of pollutants can differ significantly from neighborhood scale and only detailed flow simulations combined with field measurements can give a detailed insight into the processes giving rise to complex urban flow patterns.

References

1. Andronopoulos S, Grigoriadis D, Robins A, Venetsanos A, Rafailidis S, Bartzis J (2002) Three-dimensional modelling of concentration fluctuations in complicated geometry. Environ Fluid Mech 1:415–440
2. ANSYS (2006) ANSYS CFX Reference Manual. ANSYS Inc., 11th edn
3. ANSYS (2006) ANSYS ICEM CFD Reference Manual. ANSYS Inc., 11th edn
4. Barlow J, Belcher S (2002) A wind tunnel model for quantifying fluxes in the urban boundary layer. Bound Layer Meteorol 104:131–150
5. Burrows DA, Hendricks EA, Diehl SR, Keith R (2007) Modeling turbulent flow in an urban central business district. J Appl Meteorol Climatol 46(12):2147–2164
6. Coirier W, Fricker D, Furmanczyk M, Kim S (2005) A computational fluid dynamics approach for urban area transport and dispersion modeling. Environ Fluid Mech 5:443–479
7. Davidson M, Snyder W, Lawson R Jr, Hunt J (1996) Wind tunnel simulations of plume dispersion through groups of obstacles. Atmos Environ 30(22):3715–3731
8. Franke J, Hirsch C, Jensen AG, Krüs HW, Schatzmann M, Westbury P, Miles S, Wisse J, Wright N (2004) Recommendations on the use of CFD in predicting pedestrian wind environment. In: COST Action C14. Impact of wind and storms on city life and built environment, Working group 2—CFD techniques
9. Grimmond C, King T, Cropley F, Nowak D, Souch C (2002) Local-scale fluxes of carbon dioxide in urban environments: methodological challenges and results from chicago. Environ Pollut 116:243–254
10. Hanna SR, Brown MJ, Camelli FE, Chan ST, Coirier WJ, Hansen OR, Huber AH, Kim S, Reynolds RM (2006) Detailed simulations of atmospheric flow and dispersion in downtown Manhatten—an application of five computational fluid dynamics models. Am Meteorol Soc, pp 1713–1726
11. Huang Y, Hu X, Zeng N (2009) Impact of wedge-shaped roofs on airflow and pollutant dispersion inside urban street canyons. Build Environ 44:2335–2347
12. Lee I, Park H (1994) Parameterization of the pollutant transport and dispersion in urban street canyons. Atmos Environ 28(14):2343–2349
13. Li X, Liu C, Leung D, Lam K (2006) Recent progress in CFD modelling of wind field and pollutant transport in street canyons. Atmos Environ 40:5640–5658
14. Lundquist J, Chan S (2006) Consequences ofurban stability conditions for computational fluid dynamics simulations of urban dispersion. J Appl Meteorol Climatol 46:1080–1097
15. Macdonald RW, Friffiths R, Hall D (1998) A comparison of results from scaled field and wind tunnel modelling of dispersion in arrays and obstacles. Atmos Environ 32(22):3845–3845
16. Menter F (1994) Two-equation eddy-viscosity turbulence models for engineering applications. AIAA J 32(8):1598–1605
17. Murena F, Favale G, Vardoulakis S, Solazzo E (2009) Modelling dispersion of traffic pollution in a deep street canyon: application of CFD and operational models. Atmos Environ 43:2303–2311
18. Pope SB (2000) Turbulent flows. Cambridge University Press,
19. Richards P, Hoxey R (1993) Appropriate boundary conditions for computational wind engineering models using the k-e turbulence model. J Wind Eng Ind Aerodyn 46(and 47):145–153
20. Rotach M, Vogt R, Bernhofer C, Batchvarova E, Christen A, Clappier A, Feddersen B, Gryning SE, Martucci G, Mayer H, Miteva V, Oke T, Parlow E, Richner H, Roth M, Roulet Y, Ruffieux D, Salmond

J, Schatzmann M, Voogt J (2005) Bubble—an urban boundary layer meteorology project. Theor Appl Climatol 81:231–261

21. Sini J, Anquetin S, Mestayer PG (1996) Pollutant dispersion and thermal effect in urban street canyons. Atmos Environ 30(15):2659–2677
22. Tominaga Y, Mochida A, Yoshie R, Kataoka H, Nozu T, Yoshikawa M, Shirasawa T (2008) Aij guidelines for practical applications of CFD to pedestrian wind environment around buildings. J Wind Eng Ind Aerodyn 96:1749–1761
23. Tsai M, Chen K (2004) Measurements and three-dimensional modeling of air pollutatns dispersion in an urban street caynon. Atmos Environ 38:5911–5924
24. Vardoulakis S, Fisher BE, Pericleous K, Gonzalez-Flesca B (2003) Modelling air quality in street canyons: a review. Atmos Environ 37:155–182
25. Versteeg H, Malalasekera W (2007) An introcudtion to computational fluid dynamics. 2. Pearson Education Limited,
26. Vogt R, Eitel J, Parlow E (2006) Coupling of backyard to street canyon CO_2 concentrations. In: 6th International conference on urban climate ICUC-6, Sweden
27. Wang X, McNamara K (2006) Evaluation of CFD simulation using RANS turbulence models for building effects on pollutant dispersion. Environ Fluid Mech 6:181–202
28. Weber S, Weber K (2008) Coupling of urban street canyon and backyard particle concentrations. Meteorol Z 17:251–261
29. Xie Z, Castro IP (2009) Large-eddy simulation for flow and dispersion in urban streets. Atmos Environ 43:2174–2185

Part V.

CFD through a tree stand and solid particles

Prepared for submission to Boundary Layer Meteorology

Abstract

The focus on the study and prediction of pollen dispersion has increased in the last decade, because air-transported allergens such as pollen have been shown to be responsible for an increasing prevalence of diseases. The understanding of the emissivity and release characteristics of pollen is a key requirement towards a quantitative study of pollen dispersion. The dispersion of pollen from an isolated tree stand in Switzerland was studied in detail during the pollen emission study MicroPoem. The interpretation of the measured pollen dispersal solely based on the measurements is difficult but CFD methods have been shown to have utility in modelling such complex.

This study shows the application of CFD methods to model the flow and dispersion characteristics around the stand. Subsequently, the pollen dispersion by the stand was modelled by calculation of Lagrangian trajectories with Eulerian flow fields.

The realizable $k-\epsilon$ turbulence model was adapted for the canopy calculations, compared with the standard $k-\epsilon$ model and combined with roughness parametrization to incorporate the surrounding ground properties. The behavior and characteristics of the source were studied using two particle clouds, one accounting for the pollen emitted from the stand and one for the background concentration. The greatest difference between the measured and modelled concentration distribution was found at the measurement point furthest away from the stand. A detailed analysis of the settlement characteristics of the background pollen concentrations delivered a conclusive explanation for the observed measurement phenomena. Furthermore, the Lagrangian approach enabled detailed interpretation of the emission characteristics and the influence of the surrounding agricultural landscape, which was shown to have a significant effect on the fate of the pollen, i.e. settlement or suspension in the atmosphere.

8. Introduction

Pollen is an important component of air-borne allergens (Monn, 2001; Burge and Rogers, 2000). The variety and prevalence of diseases due to aeroallergens in Europe has continuously increased over the last decades (D'Amato et al., 2002). Trees are not only important sources of pollen but also strongly influence its dispersal through their effect on flow patterns in the atmospheric roughness layer. Knowledge of the influences on meteorological properties is important in order to understand the pollen dispersion characteristics and crucial for different research communities and applications, such as agricultural, wind engineering or meteorology. Vegetation structures used as windbreaks play several important roles in agriculture besides their effects on pollen dispersion patterns (Cleugh, 1998).

There is a long history of experimental research on the influence of different kinds of windbreaks on different meteorological properties (Aase, 1974; McNaughton, 1988; Bradley and Mulhearn, 1983; Cleugh, 1998) and several different numerical studies have been conducted, e.g. (Hagen et al., 1981; Packwood, 2000; Santiago et al., 2007; Yeh et al., 2010; Bourdin and Wilson, 2008). In these studies, the windbreaks were modelled using either an impermeable barrier or a porous structure by applying Darcy's Law or by influencing the pressure accordingly. These approaches have some limitations, especially because, according to Zhou et al. (2004), the internal structure of tree windbreaks is important. More recently, several studies have shown that vegetation canopies can be modeled as porous media using Reynolds-averaged Navier-Stokes (RANS) models with a two-equation turbulence closure (Sanz, 2003; Katul et al., 2004; Liang et al., 2006; Dalpé and Masson, 2009). Rosenfeld et al. (2010) highlight the importance of detailed studies for tree windbreaks and, based on Sanz (2003), showed the applicability of RANS models with a two-equation turbulence closure model. The results were verified with the measurement data of Bradley and Mulhearn (1983), but not with field or appropriate experimental data. Therefore, one goal of this study is to verify the numerical method with field data of the in-situ pollen emission study MicroPoem (Michel et al., 2010, 2011*b*). This natural tracer experiment aims to describe the physical process, i.e. the quantification of pollen emission as a function of (micro-) meteorological factors, because adequate protective and pre-emptive measures require both reliable assessment of production and release of various pollen species, and the forecasting of their atmospheric dispersion. The source consists of an isolated single stand near Illarsaz, Switzerland, which forms a natural windbreak. Pollen forecast models, which may be based either on statistical knowledge or full physical transport and dispersion modelling, can provide pollen forecasts with full spatial coverage (Skjøth et al., 2006; Helbig et al., 2004; Schueler and Schlünzen, 2006; Sofiev et al., 2006a,b). Basically, the central part of these recent pollen forecast models corresponds to traditional air pollution transport and dispersion models (Venkatram and Wyngaard, 1988). The most important shortcoming in these pollen transport systems, however, is the description of emission, namely the dependence of the emission rate on physical processes such as turbulent exchange or mean transport and biological processes such as ripening and preparedness for release. In the present study, the obtained pollen data are used, on the one hand, to validate the model output and, on the other hand, to describe the local pollen transport over the source and relatively quantify its contribution to the observed downwind pollen concentration.

Therefore, the goals of this study are i) to derive the numerical Eulerian approach for the modelling of the flow fields and the Lagrangian approach for the pollen dispersion, ii) to model the flow through the stand as well the pollen transport and dispersion, iii) to verify the numerical approach by comparing the flow field with micrometeorological field measurements and the pollen concentration on the lee-side of the stand, and iv) to derive the distribution of the emissivity and background pollen concentration at different measurement locations.

9. Numerical modelling

Two widely used two-equation turbulence models, (i) the standard $k-\epsilon$ model and (ii) the realizable $k-\epsilon$ model, were used to model the canopy flow. This section provides a detailed introduction to the governing equations, which is necessary to explain the derivation of the new applied realizable $k-\epsilon$ model in the canopy flow. All CFD calculations were carried out using the open-source package OpenFOAM (Weller et al., 1998). OpenFOAM is one of the most advanced and flexible open-source packages. It provides a set of C++ modules that can be used to create solvers and solutions for a wide range of research and engineering problems. We used version 1.7.1 and adapted the solver *simpleFoam* to provide support for the vegetation implementation and the Lagrangian package to cover the requirements for simulating pollen dispersion.

9.1. Governing equations

The Navier-Stokes-Equations (NSE) and the continuity equations form the governing equations for most Computational Fluid Dynamics (CFD) calculations. They describe the physics of liquids and gases in motion. The NSE are based on Newton's Law of Motion describing momentum conservation on an infinitesimal fluid element and can be written for incompressible fluid flow as in eq. 50.

$$\frac{DU_i}{Dt} = -\frac{1}{\rho}\frac{\partial p}{\partial x_i} + f_i + \nu\frac{\partial^2 U_i}{\partial x_j^2} \tag{50}$$

where U_i denotes the velocity components in three dimensions, ρ is the density, f_i body forces, p the pressure and ν the kinematic viscosity of the fluid (Versteeg and Malalasekera, 2007). The notation *incompressible* is a description of the flow properties, not of the fluid itself (Wilcox, 2000). The continuity equation for incompressible flows can be written as:

$$\frac{\partial U_i}{\partial x_i} = 0 \tag{51}$$

The RANS equations can be formed by applying the Reynolds decomposition

$$U_i = \langle U_i \rangle + u_i \tag{52}$$

to the NSE eq. 50:

$$\frac{\bar{D}\langle U_i \rangle}{\bar{D}t} = -\frac{1}{\rho}\frac{\partial \langle p \rangle}{\partial x_i} + f_i + \nu\frac{\partial^2 \langle U_i \rangle}{\partial x_i^2} - \frac{\partial \langle u_i u_j \rangle}{\partial x_j} + S_{u,i} \tag{53}$$

where ν are the kinematic viscosity and $S_{u,i}$ additional momentum sources. The Reynolds stresses $\frac{\partial \langle u_i u_j \rangle}{\partial x_j}$ introduce more variables than can be solved by the NSE and the continuity equations, giving rise to the requirement for turbulence closure, which is refered to as the *closure problem* (Wilcox, 2000). The approaches to solve the closure problem are divided into viscosity models using the turbulent viscosity hypothesis and Reynolds Stress Models (RSM), which solve additional transport equations for the stress terms.

9.2. Turbulence closure

Eddy viscosity models, like the $k - \epsilon$ model, are based on the assumption that there is a relation between the Reynolds stresses and the viscosity stresses coupled by the mean-flow properties (Versteeg and Malalasekera, 2007). The trace of the second-order tensor - the normal stresses $\langle u_i^2 \rangle$ - are called the turbulent kinetic energy (TKE) (Wilcox, 2000):

$$k = \frac{1}{2}\langle u_i u_i \rangle \tag{54}$$

whereas the the remaining components are the shear stresses. The anisotropic stresses are defined as the shear stresses minus the isotropic stresses $\frac{2}{3}k\delta_{ij}$

$$as_{ij} = \langle u_i u_j \rangle - \frac{2}{3}k\delta_{ij} \tag{55}$$

For the momentum transport only the anisotropic components as_{ij} are relevant and the isotropic part can be expressed by a modified mean pressure (Wilcox, 2000). In 1877, Boussinesq introduced the hypothesis, that in analogy to the stress-rate-of-strain of Newtonian fluids, the shear Reynolds stresses can be assumed to be proportional to the mean rate of strain (Versteeg and Malalasekera, 2007):

$$\frac{2}{3}k\delta_{ij} - \langle u_i u_j \rangle = \nu_t\left(\frac{\partial \langle U_i \rangle}{\partial x_j} + \frac{\partial \langle U_j \rangle}{\partial x_i}\right) \tag{56}$$

where ν_t is the turbulent viscosity. It has be to mentioned that this approach assumes an isotropic behavior for the normal Reynolds stresses.

In the standard $k-\epsilon$ model (Launder and Spalding, 1974), two transport equations are solved for the TKE k and the dissipation ϵ. The turbulent viscosity ν_t is obtained by:

$$\nu_t = C_\mu \frac{k^2}{\epsilon} \tag{57}$$

where $C_\mu = 0.09$ is a model constant (Wilcox, 2000). The transport equation for the TKE can be written as:

$$\frac{\bar{D}\langle k \rangle}{\bar{D}t} = \frac{\partial}{\partial x_i}\left(\frac{\nu_t}{\sigma_k}\frac{\partial k}{\partial x_i}\right) + \mathcal{P} - \epsilon + S_k \tag{58}$$

and for the standard $k-\epsilon$ model ϵ is given by:

$$\frac{\bar{D}\langle\epsilon\rangle}{\bar{D}t} = \frac{\partial}{\partial x_i}\left(\frac{\nu_t}{\sigma_\epsilon}\frac{\partial k}{\partial x_i}\right) + C_{\epsilon 1}\mathcal{P}\frac{\epsilon}{k} - C_{\epsilon 2}\frac{\epsilon^2}{k} + S_\epsilon \tag{59}$$

where σ_k and σ_ϵ are the turbulent Prandlt numbers, relating the diffusivity of k and ϵ to the turbulent viscosity ν_t according to the gradient-diffusion hypothesis (Wilcox, 2000). $C_{\epsilon 1} = 1.44$ and $C_{\epsilon 2} = 1.92$ are model constants. Neglecting buoyancy effects, the TKE production is $\mathcal{P} = \nu_t 2S_{ij}^2$.
At high mean strain rates the normal stresses can be negative ($\eta = Sk/\epsilon > 3.7$) in the standard $k-\epsilon$ model and the model constant C_μ must be related to the mean strain rate (Shih et al., 1995).
Allen (1968) found that the length scales within a canopy can be viewed as constant. Based on this, Sanz (2003) deduced relations to define $k = f(\gamma, C_\mu, U)$ and $\epsilon = f(C_d, \alpha, U)$ where C_d is the drag coefficient for the plant and α the leaf area density and γ is a dimensionless coefficient independent of the vegetation characteristics. This allows the estimation:

$$\eta = S\frac{k}{\epsilon} \approx \frac{2(\frac{\gamma}{2})^{2/3}}{C_\mu^{1/2}(2\gamma^2)^{1/3}} > 3.7 \tag{60}$$

According to eq. 60, it is worth applying the realizable model to this case.
The realizable $k-\epsilon$ model has a different transport equation for the dissipation ϵ (Shih et al., 1995)

$$\frac{\bar{D}\langle\epsilon\rangle}{\bar{D}t} = \frac{\partial}{\partial x_i}\left(\frac{\nu_t}{\sigma_\epsilon}\frac{\partial k}{\partial x_i}\right) + C_1 S\epsilon - C_2\frac{\epsilon^2}{k+\sqrt{\nu\epsilon}} + S_\epsilon \tag{61}$$

where $C_1 = \max\left[0.43, \frac{\eta}{\eta+5}\right]$ and $C_2 = 1.9$

9.3. New turbulence parametrization for tree stand

Other studies modelled windbreaks as a porous medium, e.g. Santiago et al. (2007). The internal structure of the vegetation has an important influence on the flow evolution (Zhou et al., 2004). The effects of vegetation can be incorporated in the CFD calculations by adding an additional source term in the governing equations (Kobayashi et al., 1994). The interaction of the vegetation canopy results in reducing momentum from the flow and production of turbulent kinetic energy (Wilson and Shaw, 1977). A source term can be formed for the RANS to model the influence of the vegetation by forming drag, thus minimizing the effect of the viscous drag:

$$S_{u,i} = \frac{1}{\rho}\frac{\partial p}{\partial x} = C_d\alpha|U|U_i \tag{62}$$

Both parameters C_d and α are dependent on the vegetation canopy. According to Green et al. (1995), trees reduce turbulent energy and following Sanz (2003), the loss in the k transport can be modelled with:

$$S_k = C_d \alpha \left[\beta_p |U_i|^3 - \beta_d k |U_i| \right] \tag{63}$$

where $\beta_p \in [0, 1]$ is the transfer coefficient of turbulent energy production by the mean velocity and β_d the coefficient for the TKE breakdown. Furthermore, the source term for the dissipation is:

$$S_\epsilon = \frac{C_d \alpha}{2} \left[C_{\epsilon 4} \beta_p \frac{\epsilon}{k} |U_i|^3 - C_{\epsilon 5} \beta_d |U_i| \epsilon \right] \tag{64}$$

Based on the relationship between k and ϵ, Sanz (2003) derived eq. 65 from the transport equation of the $k - \epsilon$ model:

$$\beta_d = C_\mu^{1/2} \left(\frac{2}{\gamma} \right)^{2/3} \beta_p + \frac{3}{\sigma_k} \tag{65}$$

$$C_{\epsilon 4} = \sigma_k \left(\frac{2}{\sigma_\epsilon} - \frac{\sqrt{C_\mu}}{6} \left(\frac{2}{\gamma} \right)^{2/3} (C_{\epsilon 2} - C_{\epsilon 1}) \right) \tag{66}$$

As the realizable $k - \epsilon$ model and equation (65) have the same transport equation for k, the relation for β_p is also the same. However, they differ in the form of the ϵ equation. Using the same derivation as Sanz (2003), the following correlation was derived for the realizable $k - \epsilon$ model:

$$C_{\epsilon 4} = \sigma_k \left[\frac{2}{\sigma_\epsilon} - \frac{C_1}{3 \cdot 2^{1/3} \cdot \gamma^{2/3}} - \frac{\sqrt{C_\mu}}{6} \left(\frac{2}{\gamma} \right)^{2/3} \frac{C_2}{1 + \sqrt{C_\mu}} \right] \tag{67}$$

Equations (66) and (67) were derived by inserting the assumption of Sanz (2003) into the transport equations (59) and (61) and using the relation equation (65), leading to $C_{\epsilon 4} = C_{\epsilon 5}$. Table 1 summarizes the constants used.

Table 1: Summary of the model constants used

$C_{\epsilon 1}$	$C_{\epsilon 2}$	C_1	C_2	β_p	β_d	std $C_{\epsilon 4/\epsilon 5}$	real $C_{\epsilon 4/\epsilon 5}$	γ
0.43	1.9	1.44	1.92	1.0	6.508	1.352	1.6502	0.05

A second common approach to modelling the influence of vegetation is the application of roughness boundary conditions, which is necessary in order to model the surrounding of the stand. Viscous effects have a minor influence in the free stream, whereas in the near-wall region, viscous effects and the wall-shear stress are important properties. These can be characterized by viscous scale quantities: the friction velocity u_τ and the wall units y^+ and u^+ (eq. 68 - 70).

$$u_\tau = \sqrt{\frac{\tau_w}{\rho}} \tag{68}$$

$$y^+ = \frac{u_\tau x_\perp}{\nu} \tag{69}$$

$$u^+ = \frac{\langle U \rangle}{u_\tau} \tag{70}$$

Treatment of flow in the near-wall region can be simplified by considering three different regions:

- viscous sublayer,
- buffer layer,
- log-law region

In the viscous sublayer, the wall unit y^+ equals u^+. In the log-law region u^+ is described by:

$$u^+ = \frac{1}{\kappa} \ln y^+ + B - \triangle B(k_s^+) = \frac{1}{\kappa} \ln E y^+ - \triangle B(k_s^+) \tag{71}$$

with the Kármán constant $\kappa = 0.41$, $E = e^{B\kappa}$, B the integration constant, which is determined numerically by DNS simulations (Pope, 2000), and $\triangle B(k_s^+)$, which holds the influence of the roughness. In engineering applications, roughness is commonly indicated by the roughness height k_s. For historical reasons (Blocken et al., 2007), the dimensionless sand-grain roughness is denoted as:

$$k_s^+ = \frac{k_s u_\tau}{\nu} \tag{72}$$

$\triangle B(k_s^+)$ has different forms depending on k_s^+. Following Blocken et al. (2007), three states are important: aerodynamically smooth ($k_s^+ < 2.25$), transitional ($2.25 \leq k_s^+ < 90$) and fully rough ($k_s^+ \geq 90$). In most atmospheric studies the flow is fully rough and the characteristics of surfaces are expressed in z_0. It is essential to know the relation between the aerodynamic roughness length z_0 and the roughness height k_s (Blocken et al., 2007). A wind profile in neutral surface layers can be expressed as (Stull, 2000):

$$U = \frac{u_\tau}{\kappa} \ln \left(\frac{x_\perp}{z_0} \right) \tag{73}$$

where z_0 is the aerodynamic roughness length. In OpenFOAM the fully rough case is given by:

$$\triangle B = \frac{1}{\kappa}\ln(1 + C_s k_s^+) \tag{74}$$

where C_s is a roughness constant depending on the type of the roughness ($C_s = 0.5$) (Blocken et al., 2007). Equation (71) can be rewritten to:

$$u^+ = \frac{1}{\kappa}\ln\left(\frac{Ey^+}{(1 + C_s k_s^+)}\right) = \frac{1}{\kappa}\ln\left(\frac{Ex_\perp u_\tau}{\nu_t(1 + C_s k_s^+)}\right) \tag{75}$$

A relation between k_s and z_0 can be found by comparing eq. 73 and eq. 75 with the assumption $C_s k_s \gg 1$ to bridge between engineering and meteorology (Blocken et al., 2007):

$$z_0 = \frac{C_s}{E}k_s \tag{76}$$

The near-wall model approach requires the use of meshes with a high mesh density in the near-wall regions. The y^+ can be used to quantify the mesh resolution in the near-wall regions.

9.4. Lagrangian particle dispersion modelling

A Lagrangian approach was applied to simulate pollen dispersion. Particles transported by air are influenced by different forces, including gravity, aerodynamic drag and lift force. Newton's Second Law postulates the following relation for a falling particle in the air (Shao, 2008):

$$\rho_p V\frac{\partial U_{i,p}}{\partial t} = -\rho_f\frac{\pi D^2}{8}C_{dp}(U_{ip} - U_i)|U_{i,p} - U_i| + Vg(\rho_p - \rho_f) \tag{77}$$

where the index p denotes particle properties, f for the gaseous fluid, $g = 9.81ms^{-2}$ the standard gravity, V the volume and D the particle diameter. Equation (77) can be rearranged to:

$$\frac{\partial U_{i,p}}{\partial t} = -\frac{U_{i,p} - U_i}{\tau_r} + F \tag{78}$$

with the particle response time τ_r (Shao, 2008):

$$\tau_r = \frac{8\rho_p V}{\pi\rho_f C_{dp} D^2|U_{i,p} - U_i|} \tag{79}$$

where F abbreviates the gravity and lift force. The particle aerodynamic drag coefficient is dependent on the particle Reynolds number Re_p (Shao, 2008) and modelled using the *SphereModel* of OpenFOAM, which incorporates the following relations:

$$Re_p = \frac{|U_{i,p} - U_i|D}{\nu_f} \ll 1 : C_{dp} = \frac{24}{Re_p} \tag{80}$$

$$Re_p < 1000 : C_{dp} = \frac{24}{Re_p}(1 + \frac{1}{6}Re_p^{2/3}) \tag{81}$$

$$Re_p > 1000 : C_{dp} = 0.424 \tag{82}$$

The trajectories of the particles (=pollen) are not only influenced by the mean velocity components U_i, but also by the turbulence behaviour of the gaseous fluid (Fritsching, 2004). The influence of the turbulence on the particle trajectories is modelled according to Sommerfeld (1992). The basic idea is that the turbulence influences the particle path during a defined time period τ_i, precisely the time the particle is influenced by one eddy, before the influence of an other eddy begins.

$$\tau_i = \frac{L}{|U_{i,p} - U_i|} \tag{83}$$

where L is the Lagrangian integral time of the turbulence according to Sommerfeld (1992)

$$L = c\frac{k}{\epsilon} \tag{84}$$

where $c = 0.3$ is an empirically derived constant. The fluctuating velocities are sampled using a Gaussian distribution with a standard deviation of an isotropic turbulence field $u_i = \sqrt{2k/3}$ (Gjesing et al., 2009). So the turbulence is included by equation:

$$U_{i,new} = U_i + U_i\mathcal{R}\sqrt{2k/3} \tag{85}$$

where $\mathcal{R}$ is the random number.

9.5. CFD setup

The domain for the calculations was 700 m long, 400 m wide and 100 m high: the stand was located 250 m from the inlet boundary condition. The mesh had a horizontal and vertical spacing of 2 m and a horizontal ratio of 1:50 to obtain a higher mesh resolution near the ground in order to achieve acceptable y^+ values. The velocity boundary condition was based on the recommended profile according to Richards and Hoxey (1993). The turbulent quantities were defined as:

$$k = \frac{3}{2}I^2U^2 \tag{86}$$

where $I = 5\%$ is the turbulence intensity and the dissipation:

$$\epsilon = \frac{k^{3/2}}{l_d} \tag{87}$$

where $l_d = 100\,\mathrm{m}$ is a length scale and set to the domain height. The aerodynamic roughness length z_0 was converted to the roughness height using eq. 76 for each ground cover (roughness) property featured in Fig. 12. The vegetation density in the windbreak was incorporated by an additional field with a defined leaf area density (α). The calculations for the velocity were steady-state, which were used as initial fields for the transient particle dispersion. Based on the small spherical particle diameter ($D = 23\,\mu m$), the particle calculations were coupled one-way: the flow field could influence the trajectories, but the particles did not influence the flow properties.

10. Observations and measurement methods

The COST Action ES0603 (*EUPOL*) is a multi-disciplinary project dedicated to the assessment of existing knowledge on allergenic pollen and the coordination of observational and modelling research on production, release, distribution and health impact of allergenic pollen in Europe. A considerable lack of knowledge still exists in the quantitative description of emission in pollen forecast systems. The experimental field study on pollen emission MicroPoem, (Michel et al., 2010), is a part of the *EUPOL* action, and was conducted by the Federal Office of Meteorology and Climatology MeteoSwiss and the Institute of Meteorology, Climatology and Remote Sensing, University of Basel, Switzerland. It combines experimental and modelling work in order to quantify the pollen released by an isolated source as a function of meteorological factors. The experimental set-up aimed at measuring the exchange conditions in a longitudinal transect and monitoring along- and cross-wind pollen concentration profiles in order to infer the absolute emission from the observed downwind concentration. As an example, birch trees were used because their pollen is among the most important allergens in Europe.

10.1. Observational setup

In-situ information on the turbulent exchange conditions and birch pollen distribution within the surface layer up- and downwind of a (wind break) birch tree stand was obtained from field measurements in Illarsaz, Switzerland in 2009 (Michel et al., 2010). The study site was located in a valley that was generally dominated by a mountain-valley wind system resulting in persistent wind directions (350° and 180° during day and nighttime, respectively). The windbreak is formed by an isolated patch of 120 birch trees (average height 20 m), covering an area of 203 m in the cross-wind direction by 30 m in the along-wind direction. The surrounding

area is mostly agricultural and yields a fetch length of at least 500 m in the upwind as well as downwind direction. The northern area was fallow during the campaign ($z_0 = 0.001$ m). The area south of the wind break was divided along the center-line of the tree patch into a pasture crop ($z_0 = 0.03$ m) in the east and a potato crop covered by acrylic sheets ($z_0 = 0.001$ m) in the west.
The instrumental set-up consisted of three micro-meteorological towers of 18 m height that were located on the along-wind center-line of the birch stand (Fig. 12). One tower (T1) was located 30 m upwind (during daytime conditions) of the wind break. Two towers (T_2 and T_3) were located 100 and 350 m, respectively, downwind (during daytime conditions) of the wind break. The towers were equipped with three (T_1 and T_3) or five (T_2) CSAT3 ultrasonic anemometers (Campbell Scientific Ltd., 20 Hz resolution).
Atmospheric pollen concentration profiles were monitored using Hirst-type (Hirst, 1952) samplers (7-day Spore Sampler, Burkard Manufacturing Co. Ltd. (Mandrioli et al., 1998) and Sporewatch, Burkard Scientific) at 2 m above the ground in a distance of 5 m from each tower. The pollen sampler next to T_1 yields the background concentration during daytime conditions.

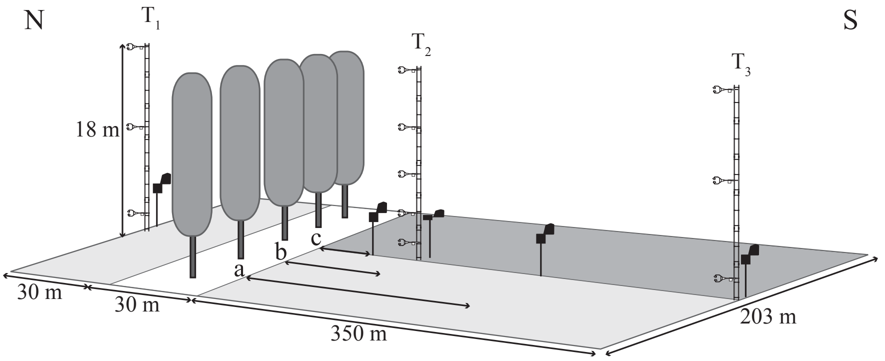

Figure 12: Set-up of sonic anemometers and bioaerosol samplers at the towers. The dark grey area south of the pollen source denotes the pasture, the light grey area denotes the acryl cover. The distances from the pollen source are a) 200 m, b) 100 m and c) 30 m.

11. Results and discussion

11.1. Observed wind profiles

The idealized flow and atmospheric characteristics (i.e. stationary and neutral conditions) were tested against the observations around the wind break by Michel et al. (2010). The mean wind profiles, measured up- and downwind of the birch stand (wind break), are shown in Fig. 13. Only cases with upvalley wind normal to the leading edge of the patch (using a threshold of ± 15°) and velocities greater than $0.8\frac{m}{s}$ were used in the analysis. The reference values were obtained from the 18 m measurements at the upwind tower. For the calculation of $\langle U \rangle$, a 60-second block averaging of the single measurements was used, since the surface layer flow conditions are assumed to be near-stationary during relatively short periods. The ideal wind profile in the neutrally stratified surface layer is logarithmic. In order to assess the sensitivity of the downwind profiles to mechanical shear induced by the wind break and buoyancy, the measurements at the individual towers were analysed for the cases of neutral as well as unstable and stable upwind conditions.

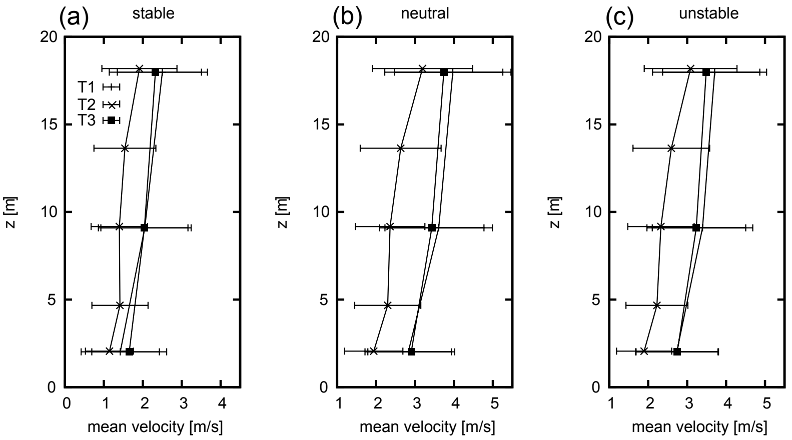

Figure 13: Velocity profiles for stability conditions (velocities > 0.8 m/s) (a) stable, (b) neutral and (c) unstable for the three towers T_1, T_2 and T_3. The selection of stability cases, velocity classes and flow conditions was based on measurement point 18.5 m above ground at tower T_1.

11.2. Effects of stability

Under neutral upwind conditions (Fig. 13b), the measurements indicated a logarithmic wind profile at the towers T_1 and T_3. The roughness length in the fetch area of both locations was less than 0.03 m. Large roughness elements (i.e. the wind break in the case of T_3) are several hundred meters away. A different wind profile was observed at T_2, which is only 100 m downwind of the wind break. The mechanical impact of the large roughness element was clearly visible within the height of the canopy layer, i.e. roughness sub-layer. Generally, the wind velocities at each height were significantly smaller, as momentum was lost due to the high roughness throughout the entire profile. The shape of the wind profile was

strongly influenced by the vertical leaf-area density profile of the wind break. The lowest wind velocities were measured closest to the surface at 2.2 m. They were strongly influenced by the surface boundary on the one hand and by the dense understorey within the birch stand on the other hand. The wind velocity still increased rather logarithmically with height within the trunk space, measured at 5 m. Within the canopy layer, however, momentum was lost significantly due to the greater leaf-surface roughness. The profile indicated a small velocity gradient between the second and the third level, measured at 9.6 m. Higher above, the wind velocity increased with height due to leeward mixing with undisturbed flow at > 20 m.
In the case of non-neutral upwind conditions, the velocity profiles measured at T_1 and T_3 deviated from the logarithmic relationship. In stable and unstable situations (Fig. 13a and c) the undisturbed profiles curved downwards and upwards, respectively. Also, the average wind velocity was generally lower than in neutral situations. The measurements at T_2, however, indicated a similar shape under non-neutral and neutral conditions within the canopy layer. Thus, the mechanical impact of the wind break on the profile was clearly visible. Thermal effects are superimposed, regardless of the atmospheric stability. The measurements indicated that, within the framework of the present study, the idealization of neutral conditions is valid in the case of the leeward profile close to the wind break, i.e. at T_2.

11.3. Observed pollen concentration

Figure 14 shows the ratio between the downwind pollen concentration and the background concentration measured at T_1.

The measurement data showed strong variances but clearly indicated a slightly higher concentration at 30 m behind the stand and then a decay to the measurement point at 200 m behind the stand. The highest concentration was found at 350 m behind the stand. Based on the data, a clear determination of the emissivity of the stand is difficult, as the background concentration and pollen from the stand cannot be distinguished by the measurements alone. In addition, the higher concentration at 350 m behind the stand needs further investigation. To address these problems, the stand was studied using CFD methods, as discussed in the next section.

11.4. Modified velocity profiles

For the following analysis, turbulent structures traveling through the wind break were monitored by relating the downwind averaging periods to the upwind time step, and by calculating the time lag with the average wind velocity. As a first approach the stand was modelled using a constant value for the leaf area density to test the performance of the standard $k-\epsilon$ and the realizable $k-\epsilon$ model. A drag

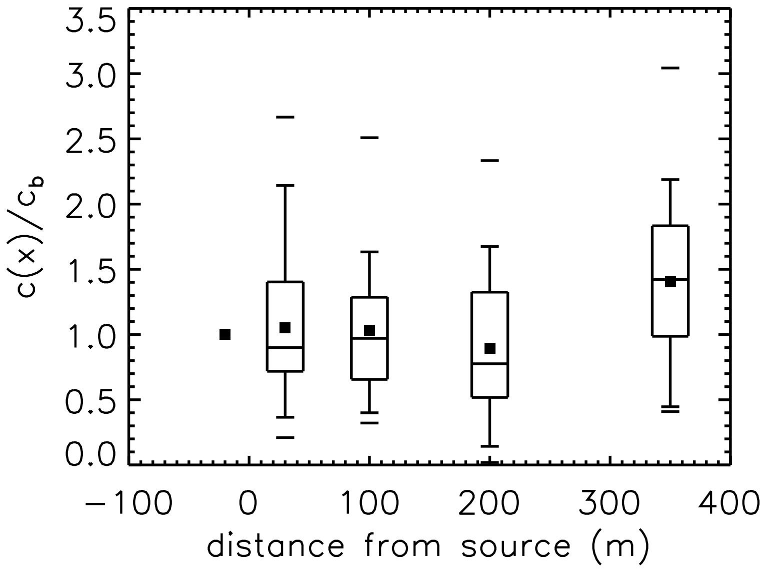

Figure 14: Normal longitudinal pollen distribution at 2 m above ground at the location indicated in Fig. 12. Rectangular inflow (±15°) and velocity $> 0.8\,\mathrm{m/s}$

coefficient of $C_{d,std} = 0.2$ following Dalpé and Masson (2009) for the standard $k-\epsilon$ model was applied. To achieve comparable results for the same source strength, respectively, an equal α value and a lower coefficient ($C_{d,real} = 0.16$) have to be used for the realizable $k-\epsilon$ model.

The velocity profiles for both models and in-situ measurements are shown in Fig. 15. The measurements have a large variance, nevertheless, both models show very good agreement with the mean properties. The realizable $k-\epsilon$ model reproduces the velocity profile in the canopy area ($8 < z < 20\,\mathrm{m}$) to fit the mean values of the velocity measurements slightly different to the standard $k-\epsilon$ model. This can be explained by the higher shear stresses in the canopy, where the standard $k-\epsilon$ shows some disadvantages (Shih et al., 1995).

To account for the varying leaf-area density in the stand, a general relation between the maximum leaf-area density α_{max} and the corresponding height was used, as suggested by Lalic and Mihailovic (2004). α_{max} is based on values suggested by Stadt and Lieffers (2000), derived from a light transmission model calculating the leaf-area densities for different tree species. Taking the date and season of the measurements into account, as well as results from test calculations, a $\alpha_{max} = 0.1$ was found to appropriately describe the stand. The high understory was incorporated using a higher leaf-area density of approximate $\alpha = 0.75$ (Fig. 16).

Three velocity classes were calculated using both models to study the influence on the particles dispersion, where V denotes the abbreviation for each class. Figure 17 shows the velocity profiles for tower T_2, 100 m behind the stand for the different

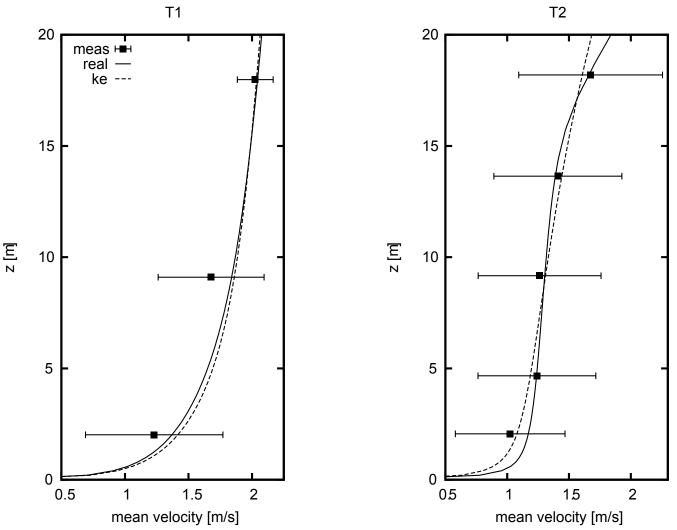

Figure 15: Velocity profiles for constant leaf-area density α for $1.25 < |U| < 1.75\,\mathrm{m/s}$ at the upwind tower T_1 and leeside T_2

velocity classes.

As can be seen for all three velocity classes, both models were able to reproduce the influence of the stand. As found in the parameter pilot-study with uniform α values, a lower drag coefficient C_d for the realizable $k-\epsilon$ model had to be adopted to achieve the same results. Furthermore, both drag coefficients for the lowest velocity class ($1.25 < |U| < 1.75$) had to be reduced by about 20%.
A large discrepancy between the models was found at tower T_3, which is located 350 m behind the stand. Both models develop a logarithmic profile, but the realizable $k-\epsilon$ model under-predicts the velocity. This effect was found for all velocity classes. Both models are within the variance of the measurement data, however, the standard $k-\epsilon$ model shows a significantly better quantily agreement with mean properties.

11.5. Modeled TKE distribution

Figure 18 shows the turbulence intensity profiles for all three towers calculated according to eq. (86). It can be seen that the standard $k-\epsilon$ model is in good accordance with the measurements, whereas the realizable $k-\epsilon$ model slightly under-predicts the turbulence kinetic energy. At tower T_1, the numerical profiles are lower than the mean measurements, but in the standard deviation of the TKE values.

The measurements show a mean turbulence intensity of $I \approx 17\%$, Fig. 18. According to Richards and Hoxey (1993) a turbulence intensity of $I = 5\%$ was applied to the inlet boundary conditions.

Figure 16: Image of stand from upwind to downwind direction during measurement campaign

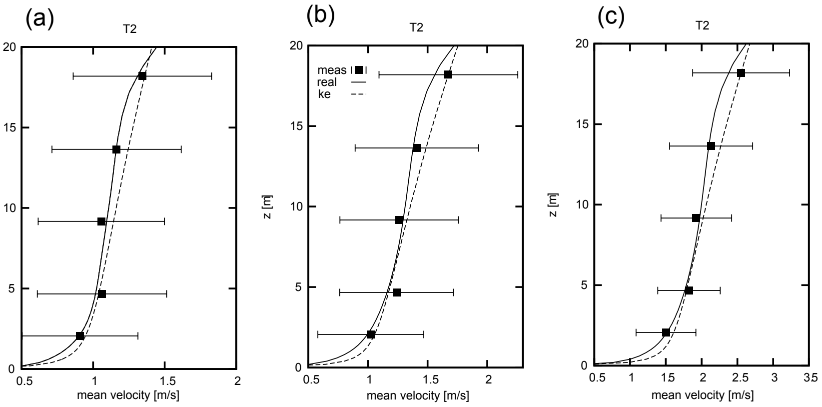

Figure 17: Velocity profiles for both models at tower T_2 for the three velocity classes: (a) $1.25 < |U| < 1.75$, (b) $1.75 < |U| < 2.25$ and (c) $2.75 < |U| < 3.25\,\mathrm{m/s}$

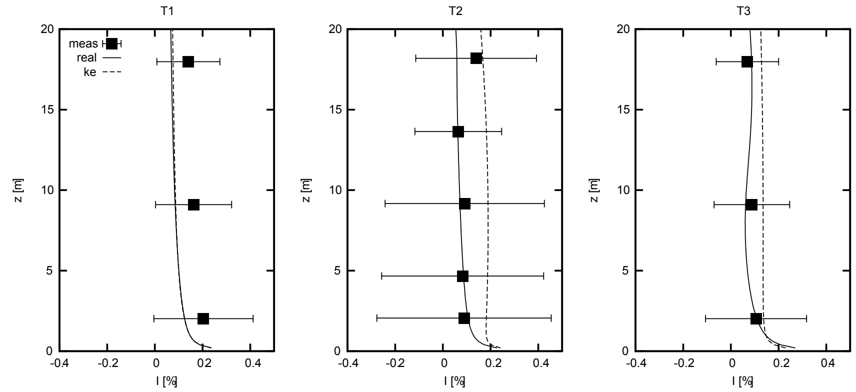

Figure 18: Turbulence intensity profiles and deviation for all three towers

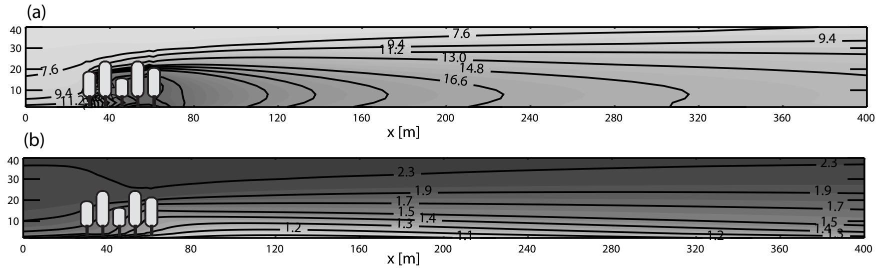

Figure 19: Cross sections for (a) turbulence intensity I and (b) velocity $|U|$ for velocity class $1.75 < |U| < 2.25\,\mathrm{m/s}$

Figure 19 shows the cross sections for the turbulence intensity I and the velocity, respectively. The stand introduces a higher turbulence level on the lee-side of the stand and the turbulence contour before the stand is raised by the stand over $z > 20\,\mathrm{m}$ and increases successively behind the stand. Under the crown area ($z \cong 7\,\mathrm{m}$), the higher intensity is transported downstream. The reduction of the mean velocity by the stand can be seen in Fig. 19b and the influence of the reduction continues to $x > 380\,\mathrm{m}$ behind the stand.

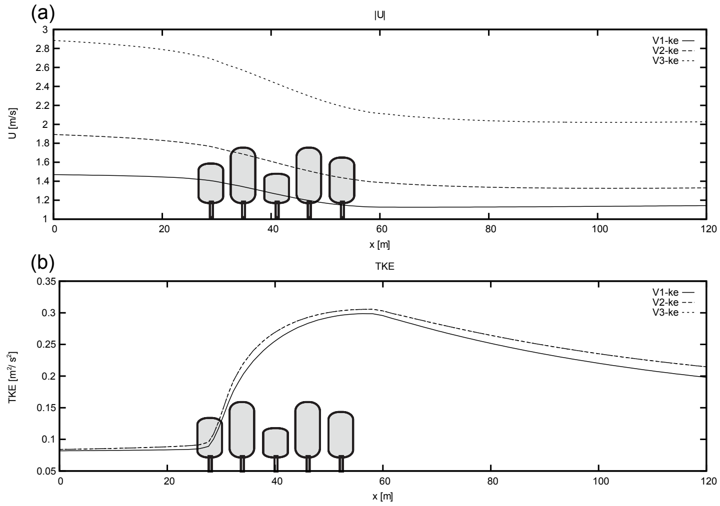

Figure 20: (a) Velocity 10 m above ground and (b) TKE

Figure 20a shows the mean velocity at 10 m above ground. All three velocity classes show the same behaviour: the stand reduces the mean velocities by approximately 30%. Figure 20b shows the influence on the TKE, where an increase in turbulence intensity I can be seen behind the stand. A significant higher ratio is found at higher velocities, which results from the definition of source strength eq. 63, where the velocity magnitude influencing in third power.

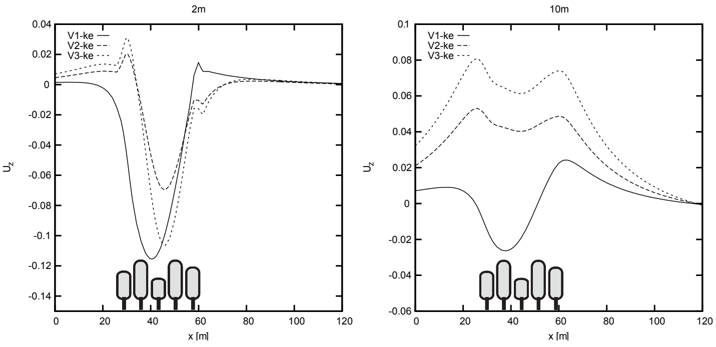

Figure 21: (a) Vertical velocity 2 m and (b) 10 m above ground from the $k - \epsilon$ model

Figure 21a shows the vertical velocities at 2 m above ground. Within and behind the stand, small negative horizontal velocity components opposite to the mean wind before the stand develop for all velocity classes. This derives from the isotropic definition of the momentum source eq. 62 and is in good accordance with other studies, e.g. Heisler and DeWalle (1988); Cleugh (1998). However, Fig. 21b shows positive horizontal velocity components developing at 10 m above ground for velocity classes V2 and V3 only. It seems that, at higher velocities, the vertical flow components arising from the resulting drag of the stand dominating at this altitude level the isotropic sources, whereas at lower velocities the influence is similar to 2 m above ground.

11.6. Pollen dispersion modelling

11.6.1. Stand and background concentration

The standard $k - \epsilon$ model was used for the particle dispersion calculations, as the realizable model led to under-prediction of the velocity at tower T_3. Two particle injection regions were defined: (1) cloud A: located at the inlet boundary condition, with a normal diameter distribution to simulate the background particle concentration; (2) cloud B: located in the tree crown. The particle injection points were distributed using a Gaussian normal distribution over the surface of the inlet boundary condition (cloud A) and within the volume of the tree crown (cloud B). The particle trajectories were calculated for a time period of 10 min with a time step of 0.5 s by injecting $n = 1000$ particles every second for each cloud, leading to a total of $n = 1.2 \cdot 10^6$ individual particles.

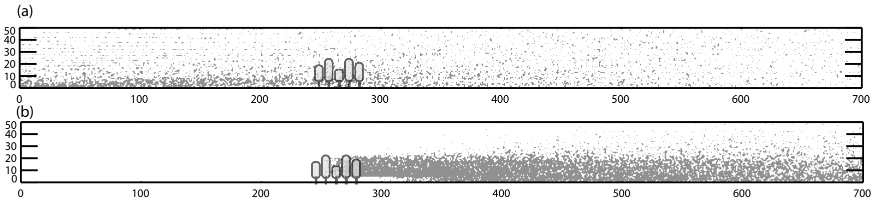

Figure 22: Cross-section of summarized particles for time steps 2, 4 ,6 and 8 min, (a) particles for injection at the inlet boundary condition and (b) for injection in the tree crown.

Figure 22a shows the particles starting from the inlet boundary conditions (cloud A) and Fig. 22b shows cloud B released from the tree crown, respectively. Particles from cloud B either settle approximately > 30 m behind the stand, are suspended in the atmosphere (defined as rise to¡ an altitude over 40 m above ground) or are transported over the outlet boundary.

The numerical results were analysed at the four measurement points (Fig. 14) 2 m above ground (Fig. 23).

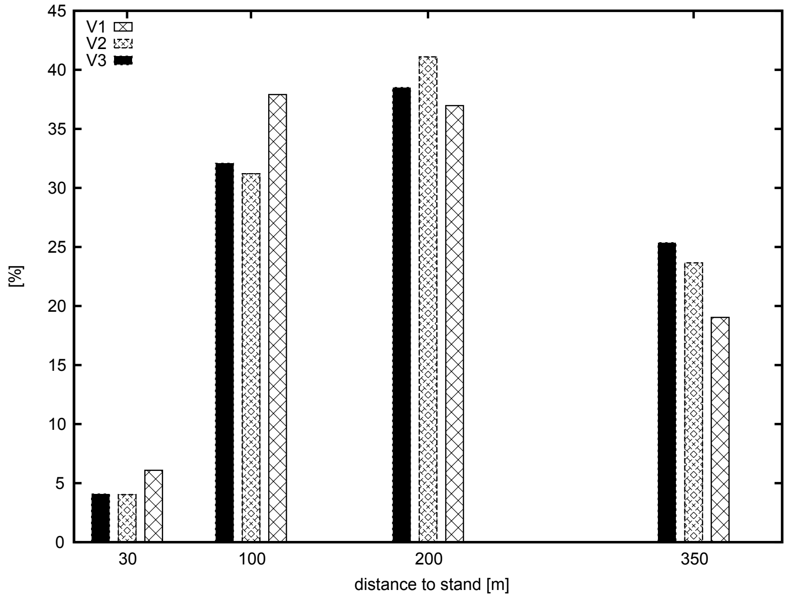

Figure 23: Distribution of modelled particles at 30, 100, 200 and 350 m behind the stand and 2 m above ground for the particle released in the stand

Velocity classes V2 and V3 show approximately the same characteristics: the peak concentration of cloud B particles was found around 200 m behind the stand. For velocity class V1, the peak concentration was found 100 m behind the stand. This discrepancy can be explained by the different velocity components found at 10 m above the ground as shown in Fig. 21b. The lowest particle concentration was found 30 m behind the stand for all velocity classes. To study the emissivity of the stand and the cause of the different concentrations in the measurements (Fig. 14), the influence of the background concentration has to be taken into account. The modelling and interpretation of the background concentration is more difficult. A uniform injection pattern was defined over the entire vertical inlet, assuming well-mixed conditions for near-ground concentrations. However, the lower velocities and higher turbulence intensities near the ground lead to a small mean velocity for particles injected near the ground and unsteady trajectories, resulting in a higher particle concentration near the ground. This artifact cannot be eliminated without synthetic inlet boundary conditions. Nevertheless, this would not guarantee a homogeneous vertical concentration near the stand due to the lower velocities near the stand, nor would give it an additional benefit.

On the other hand, the influence of the leaves, branches and trunks on the particles was not captured by the presented approach. Based on the considerations above, it becomes apparent that the derivation of the complex situation from field

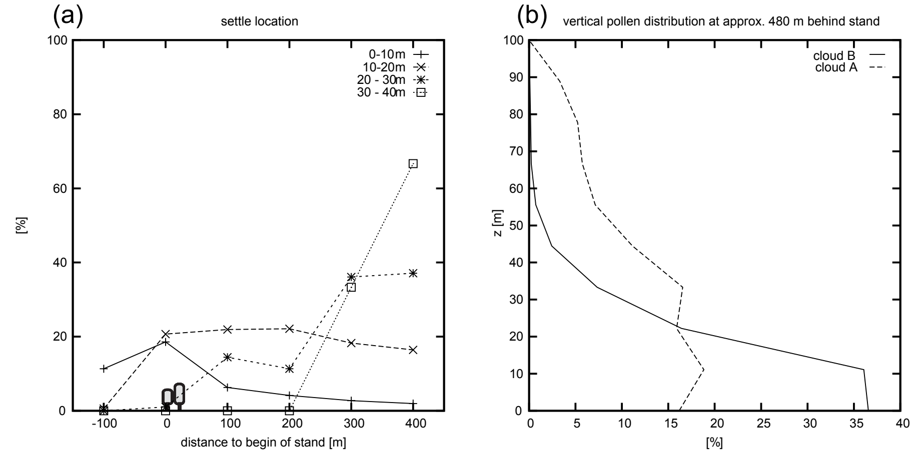

Figure 24: Percentage of longitudinal settling locations of particles (from cloud A) in dependence of the injection height (a). Vertical distribution of all particles (according to clouds) leaving the computational domain (b).

observations alone is difficult. The distribution of the vertical injection locations and the longitudinal settling points were studied to capture the influence on the measurement points of the lee-side of the stand (Fig. 24). The lower velocity before, within and on the lee-side of the stand, as shown in Fig. 19, lets the particles injected lower than 10 m above ground settle before the stand and shortly behind it (Fig. 24a). Injected particles between 10 m and 20 m above ground were spread uniformly behind the stand. These distributions have to be interpreted critically, as the trajectories pass through the crown area of the stand, whereby the influence of the leaves and branches was neglected. It is assumed, however, that a large amount of these particles are trapped in the leaves and therefore do not affect the measurements in the indicated amount. For particles entering $> 25 - 30$ m above ground, the settle location was > 200 m behind the stand. They were transported over the stand and then influenced by the curvature in the velocity profile and the higher turbulence intensity behind the stand, (Fig. 19). To summarize:

- Pollen clouds reaching trunk-height decrease in concentration during passage through the stand.
- Pollen approaching the crown region are spread (in the numerical results) over the measured area, but it can be assumed that a larger amount are trapped in the leaves and trunks and are not transported through the stand.
- Pollen approaching near the top of the stand (approx. 25 m above ground) started to settle > 50 m behind the stand with an increasing share at > 300 m.

- Pollen approaching up to twice the stand height (approx. 15 m above the top) settled > 250 m behind the stand.

Figure 24b shows the vertical particle distribution approximately 480 m behind the stand. Based on the numerical results, the observed particle concentrations shown in Fig. 14, can be attributed to particles passing through the lower, less denser trunk space and decelerated by lower velocities causing them to settle together with a small amount of particles emitted in the crown layer of the stand. The measurement points 100 m and 200 m behind the stand are mainly influenced by the stand, whereas the 350 m point was influenced by a background concentration approaching the stand at levels higher than 20 m (Fig. 24a) as well as by the particles emitted from the stand. Based on these numerical results, the measurement at 200 m behind the stand represents the concentration with the lowest influence of the background concentration. This is consistent with the observations of an additional grid of 18 pollen samplers at 2 m above the ground. The highest concentration was found at 200 m behind the stand for cases, where the wind velocity was > 3 m/s (Michel et al., 2011*a*). Higher wind velocities seem to increase the downwind settlement distance of background concentration to more than 350 m. Nevertheless, a clear and defined relation for the measured pollen at 2 m above ground is difficult to define.

11.6.2. Settlement and suspension of emitted particles

One of the advantages of the Lagrangian approach is the possibility to model the trajectories of each particle in space and time.

Figure 25a shows the distribution of the settlement distance of the particles emitted from the stand. Most particles settle between 100 m and 200 m behind the stand, with only minor differences between the velocity classes. Another interesting point is the influence of the vertical injection location within the stand on the trajectory pathways. Figure 25b shows the relation between injection point and fate, i.e. whether particles settle or remain in suspension. Most of the particles that settled, were injected in the lower area of the stand ($5 < z < 10$ m), whereas the particles that remained in suspension originated from a constant distribution over the stand with higher proportion from the top of the stand ($z \approx 20$ m). The higher probability that particles injected near the ground would settle nearer to the stand is clearly affiliated with the low velocities in this region. However, the constant regime of the suspended particles was not as clear. The cause of this phenomenon can be attributed to the lateral distribution, Fig. 26. The different roughness of the ground on the lee-side of the stand influences the flow patterns and leads to a higher turbulence and lower velocities.

The higher z_0 of the pasture crop supports the suspension of particles, whereas the lower z_0 of the acrylic sheets in the west supports settlement (Fig. 26). As a

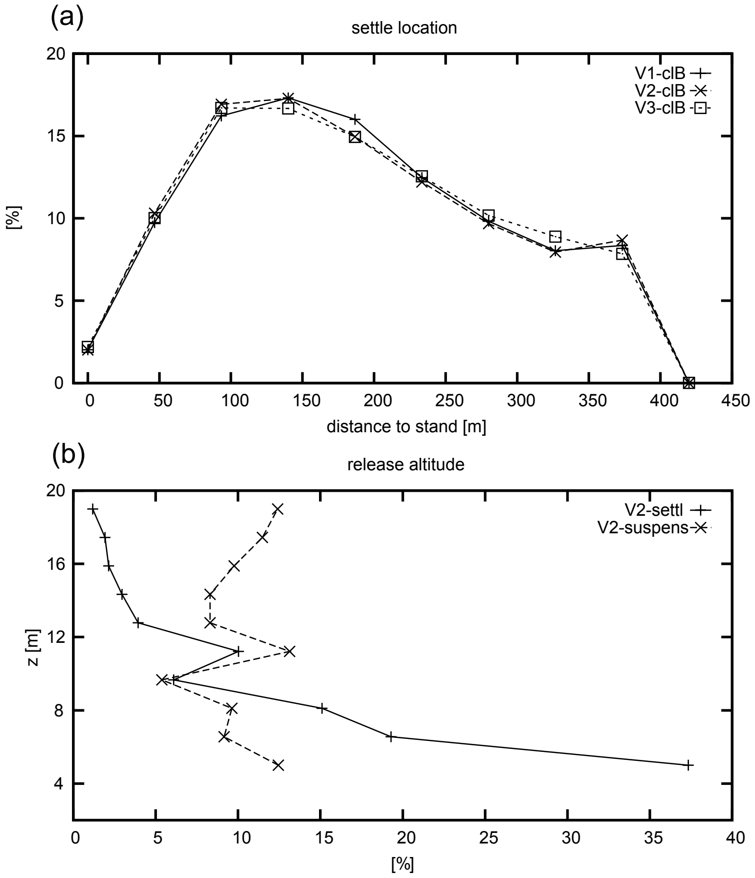

Figure 25: (a) Settlement distance from the stand for three velocity classes and (b) distribution of the injection point in relation to settlement and suspension of the particles. Histogram plot with 10 distance classes from $0 < x < 420\,\mathrm{m}$, respectivly height classes $5 < z < 20\,\mathrm{m}$

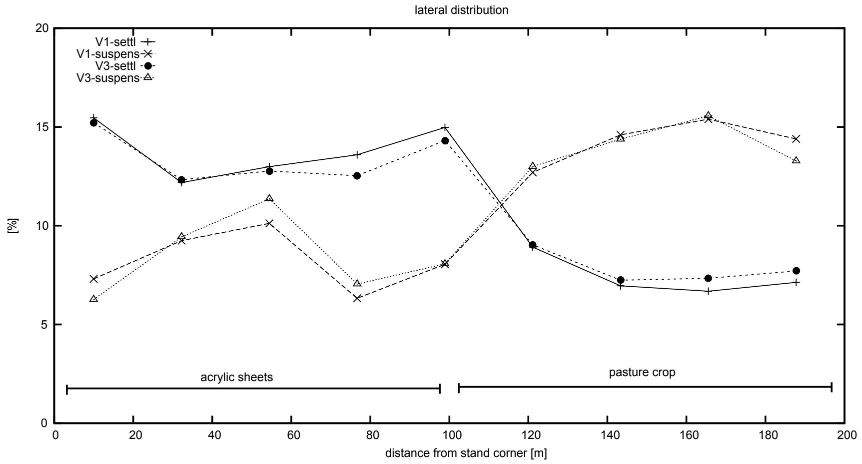

Figure 26: Lateral distribution of amount of suspended and settled particles. Histogram plot over the lateral distance ($0 < y < 200\,\mathrm{m}$)

further factor, the higher turbulence level on the lee-side strongly influences the trajectory path-lines (eq. 83 and Fig. 19a). The high turbulence values have the ability to influence the light particles and transport them from lower injection locations in the stand to above the stand.
Finally Table 2 gives an overview of the amount of particles settled (landed on ground) and suspended (left domain on a higher altitude than 40 m above ground) within the model domain. The remain is transported over the outlet boundary.

Table 2: Summary of settled and suspended particles released from the stand within the length of the computational domain for the three velocity classes

$Vel.class$	$\%_{settle}$	$\%_{susp}$
V1	6.1	3.9
V2	6.7	5.3
V3	6.6	6.9

An increase in the velocity has a minor influence on the amount of settling particles, whereas more particles are suspended. This can be explained by the fact that the turbulence has a dominating effect on the particles lee-side of the stand, which leads to longer Lagrangian integral times (eq. 84).

12. Conclusion

The assumption of neutral conditions enables some important simplifications to be made in numerical studies, mainly neglecting of thermal effects. In this study, a set of temporally and spatially highly resolved measurements was able to confirm the assumption of neutral conditions around vegetation roughness elements, such as a windbreak in the form of a stand of birch trees. The CFD method assuming neutral conditions was evaluated with very good agreement with the measurements. The experimental setup provided an ideal environment for the verification of CFD methods for canopy flows. The application studied the implementation of source terms in the governing equation to model the effect of a tree stand on flow. Two widely used turbulence models with modifications (the standard $k - \epsilon$ and realizable $k - \epsilon$ model) were compared to measured data.

The model results were in very good agreement with the mean velocity properties of the measurements. It was shown that the applied numerical approach is suitable to model the influence of vegetation objects on the flow in the atmospheric roughness layer. The comparison between the realizable and the standard $k - \epsilon$ models demonstrated a better performance of the realizable model at a measurement point 100 m downwind of the stand, but poorer results for larger distances, where in contrast, the standard $k - \epsilon$ model showed a better performance. The turbulence intensities also corresponded well with the measured intensity ranges.

A Lagrangian approach was used to model the pollen dispersion from two sources: background (inlet boundary) and emitted from the stand. The large variances in the pollen measuremens made it difficult to validate the numerical data with the measured data. Nevertheless, a conclusive explanation for the measured values could be found by analysing the trajectories of the modelled background concentration. Particles emitted from the stand settled between 100 m and 200 m behind the stand and only a small dependence on the studied velocity range from 1.25 m/s - 3.25 m/s was found. The influence of the background concentration on absolute downwind concentrations was obtained by deriving the dependency of the injection altitude at the inlet boundary condition and the longitudinal settle locations. It could be shown that the lower velocity around the stand induced near-ground background pollen to decelerate and thus to settle around the stand. Pollen injected higher than the stand altitude settled $>$ 200 m behind the stand. Thus, measurements taken further away were primarily influenced by the background concentrations, which approached the stand at up to twice the stand height. Furthermore, the trajectories were analysed by differentiating between settling particles (landing on the ground) and suspended particles (raised 40 m above the stand). The results show that most of the settled particles originated in the lower area of the stand, whereas the particles remaining in suspension originated from the whole stand. This irregularity could be assigned on the one hand to the low particle weight and therefore the high sensitivity to the high turbulence on the lee side of the stand. On the other hand, two different roughness lengths on the lee side enhance or degrade the ability for pollen to remain in suspension. In general, the tree stand introduces lower velocities and therefore supports the settlement, both of the background cloud and of the particles emitted from the lower area of the stand. In contrast, on the lee-side of the stand, the higher roughness of the pasture crop increases the amount of suspended particles.

The results from this study show the utility of numerical CFD methods to help understand complex natural phenomena. The approach used made it possible to model flow characteristics around very complex structures such as the tree formations studied here. This could be a great benefit, for example, for urban CFD calculations, which aim at assessing the influence of vegetation on the micro-meteorological conditions, which can influence the dispersion and transport of traffic emitted pollutants.

Part VI.
CFD on a neighborhood scale

13. Introduction

Parra et al. (2010) introduced a concept widely used in wind-engineering applications to the field of urban research: driving steady-state solutions with measurements in order to obtain a high-resolution temporal and spatial flow-field (pseudo-transient solution). The study used 1 h resolved concentration measurements to validate the approach. However, wind conditions can vary significantly during 1 h. In addition, as transport of pollutants and particles is determined by the flow patterns in urban areas, higher temporal resolution flow fields become even more important (Vardoulakis et al., 2003). Furthermore, Parra et al. (2010) validated the numerical data with one meteorological station in the domain. The Basel Urban Boundary Layer Experiment (BUBBLE) involves wind measurements with high temporal and vertical resolution in a deep street-canyon (Rotach et al., 2005) and thus is an ideal case that can be used to validate a numerical approach.

13.1. Study site and measurements

The study site was located in a densely built-up area of the city of Basel, Switzerland, Figure 27.

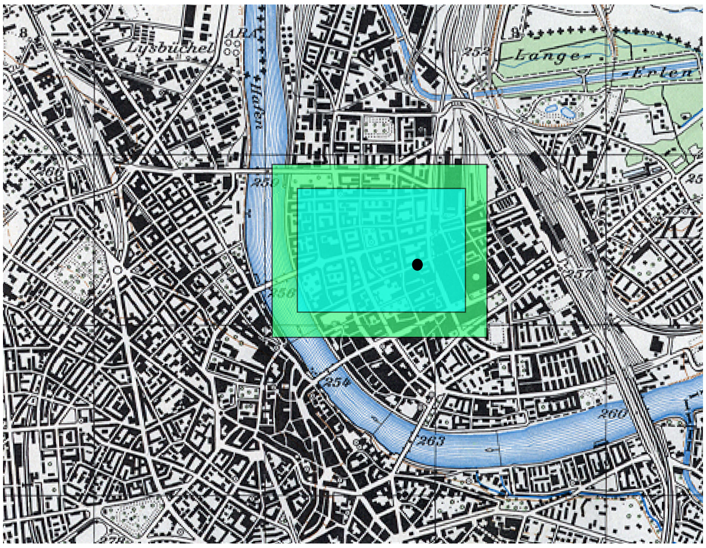

Figure 27: Map of downtown Basel. Indicated are the computational domain extend (outer bound) and the resolved buildings (inner bound), as well the measurement location (point). Base map (c) copyright GVA BS, 25102002

During the extensive BUBBLE campaign, one measurement tower was located in a street canyon ($H/W = 1$), where H is the building height and W the width of the street canyon (Rotach et al., 2005). The tower was equipped with six sonic anemometers installed between 3.6 m and 32 m above ground. The wind fields were measured with a time resolution of 20 Hz.

13.2. Inventory approach

Long transient calculations covering large spatial extents are computationally too expensive to conduct even using RANS. Parra et al. (2010) applied a common method in wind-engineering applications to an urban area: they used wind inflow classes from measurements to drive an inventory of steady-state CFD result fields. The study successfully correlated the results of transported pollutants with 1-hour measurements. Based on their results, this study compared the numerical results to vertical wind measurements in a deep street canyon and to a higher temporal resolution of 2 min mean values. The numerical inventory consists of 12 steady state calculations for 30° wind sectors ($10°, 40°, ..., 340°$). The measurement locations were positioned in SE corner of the domain, but far enough from the boundary conditions not to be directly influenced. The sensitivity on the location could also be derived by this approach, providing a further impression of the spatial significance of the results. Furthermore, the validation with the measurements within the street canyon can give a clear prediction of the quality of the numerical results in space and time. To prove the concept of driving an inventory of steady-state RANS calculations with measurements, the assumption that the response time of changes in the inflow conditions must be coherent along the vertical velocity patterns in the street canyon has to be fulfilled. This means that changes of the inflow angle or magnitude at the highest measurement point (32 m above ground), which will be used as driver, affects the conditions within the street canyon in the timescales resolved. The results of a transient run over a smaller domain around the measurement location is discussed in the section 14.1.

13.3. CFD setup and software

The open-source software package OpenFOAM (Weller et al., 1998) was used for all CFD runs. The package consists of a set of core-libraries enabling users to create applications for their specific needs. Therefore, it is one of the most advanced and readily expandable open-source packages for numerical finite methods. One of the standard solvers, *simpleFoam* (steady-state), and the *pisoFoam* (transient) solver were adapted to the needs of this study, mainly for supporting logarithmic inlet boundary conditions based on a relative altitude over ground, as the inlet conditions did not have an even altitude. The mesh for the transient runs consisted of $> 2.5 \cdot 10^6$ elements and for the inventory cases of $> 21 \cdot 10^6$. Velocity boundary conditions were based on the relation from Richards and Hoxey (1993) and the turbulent properties k were set according to Tominaga et al. (2008):

$$k = \frac{3}{2} I^2 U^2 \tag{88}$$

where $I = 5\%$ is the turbulence intensity and for the dissipation ϵ :

$$\epsilon = \frac{k^{3/2}}{L_t} \tag{89}$$

where L_t is a length scale, which was set to the domain height of 100 m. The velocity-pressure coupling in the steady-state inventory calculations was based on the SIMPLE and for the transient runs on the PISO (Versteeg and Malalasekera, 2007). Smooth wall-functions were used for the building and ground surfaces and the top boundary was set to slip conditions, which prevents fluid traveling normal to the boundary from passing through, but uses Neuman conditions for tangential velocity components. This prevents the top boundary from influencing the flow to lower altitudes. The complex geometries make it essential to create a good initial field for the transient as well as the steady-state simulations. This was achieved by applying fixed value boundary conditions for all properties (including the turbulence properties) on all boundary conditions and neglecting wall functions for the first 60 iterations. These result fields were then used to start the calculation, with appropriate pressure boundary conditions at the outlet boundaries and corresponding wall functions for the ground and building surfaces.

14. Results & Discussion

14.1. Requirements for pseudo-transient results

To drive an inventory of steady-state RANS results with measurements, the response time of flow patterns of areas not directly influenced by the boundary flow must have the same timescale as the changes at locations in the above boundary layer. A significantly shorter timescale has to be applied that the assumed steady-state from the inventory is actually present for most of the time before the forcing changes again. Note that, in an inventory simulation, these are no physically resolved transitions of direction and speeds. If the spacing between buildings is higher than a ratio of $H/W \approx 1$, the flow in the street canyon tends to decouple from the free flow, which is often referred to as skimming flow (Oke, 1988; Hunter et al., 1991). Only a small tangential influence at the top of the street canyon influences the motions within the street canyon and pressure differences lead to a vortex flow (Hunter et al., 1991).

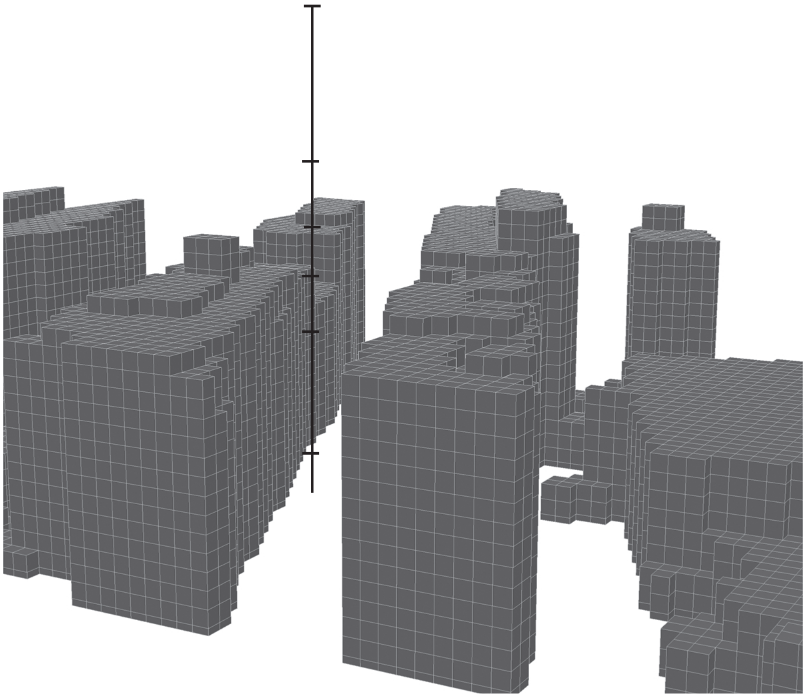

Figure 28: Image of a part of the test domain. The vertical line indicates the location of the sample points with the same altitude allocation as during the measurement campaign

In this case, the response time is assumed to be slower than in the coupled cases with $H/W < 1$. In order to lower the coupling of the free flow and the street canyon, the CAD geometry was scaled to artificially create deeper street canyon for the test case. Figure 28 shows the extent of the street canyon. A transient case was calculated by changing the inflow angles at the inlet conditions. A time-step of 15 s was used and the calculation was started from an initial field obtained from a steady-state solution with wall functions neglected and fixed values for all boundary conditions. Figure 29 shows the time starting from 550 s, at which time steady-state has developed.

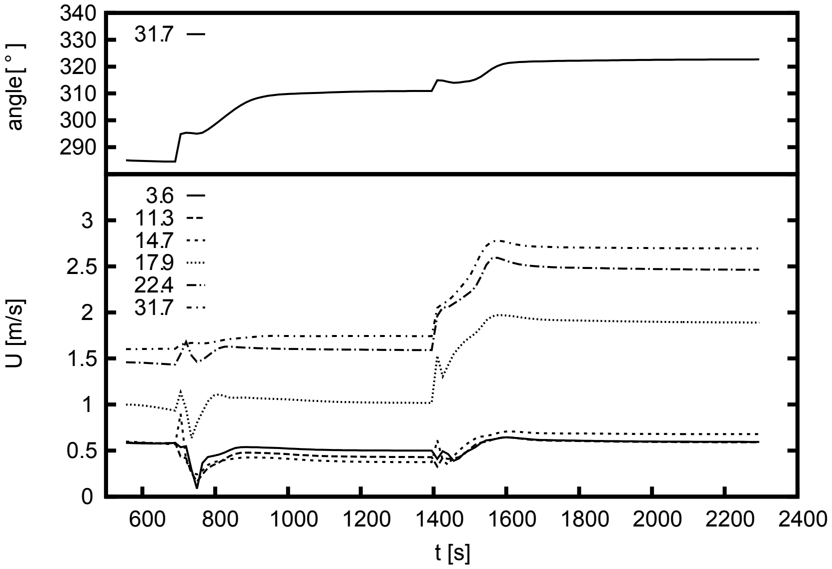

Figure 29: The upper panel shows the angle at 31.7 m above ground for sample points. The lower panel shows the velocity at the corresponding sample points.

As shown in the upper panel of Fig. 29, two changes (around $t = 600$ s and $t = 1400$ s) in the inflow angles were implemented. Changes in the inflow conditions at 31.7 m above ground result in a change in the velocity distribution within a few minutes. The jumps in the velocity curves for lower levels shown in the lower panel of Fig. 29 result from numerical artifacts. The continuous change in the wind angle arises from the fact that a new stationary flow configuration is developed after the instant change at the boundary condition. Based on these results it can be concluded that a significantly longer time period than 2 min has to be used to be on the safe side.

14.2. Results of steady-state runs and validation with measurements

Figure 30 shows the velocity distribution over the modelled area approximately 10 m above ground. The figure illustrates well the heterogeneity of the velocities. Streets oriented parallel to the inflow (inflow in SE-NW direction) have larger area and higher velocities than the street canyons rectangular to the flow. The unaligned street structure introduces a further complexity in the flow patterns that underlines the necessity for physically based and highly resolved model approaches.

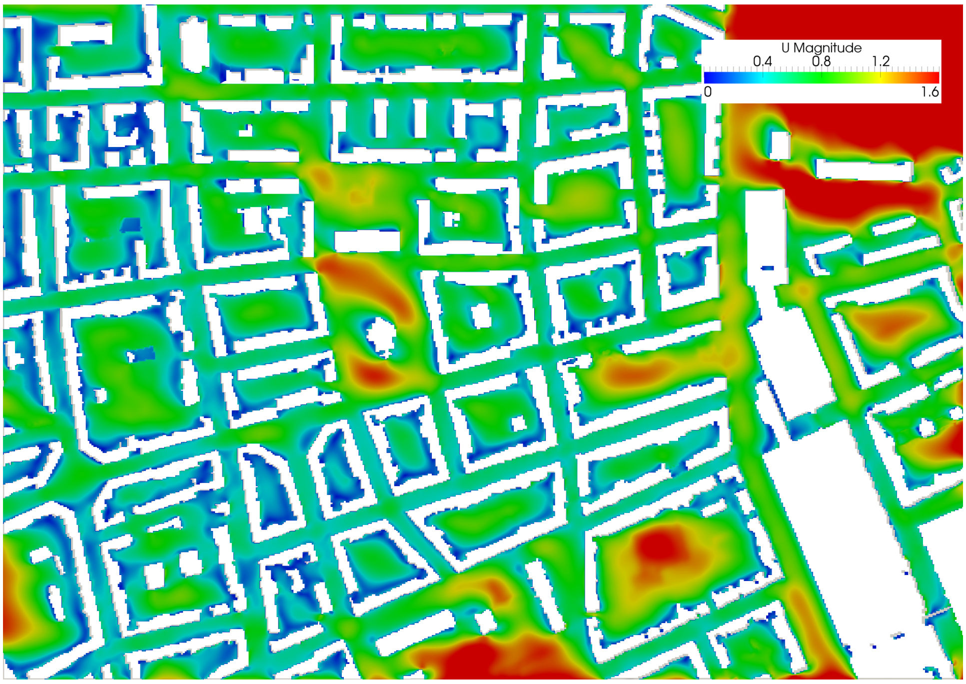

Figure 30: Velocity distribution approx. 10 m above ground over a part of the modelled area for 130° inflow conditions

The twelve steady-state results representing 30° inflow conditions were compared to one month 20 Hz data. The data were analysed by applying the Reynolds Decomposition with an average time-period of 5 min and filtering of the angles used for the numerical results (±15°) chapter IV. The main wind direction over the studied site ranges from SE (130°) to W (270°). The detailed profiles for three angles are set as follows: SE (130°) representing the main wind conditions, NE (40°) for boundary conditions closer to the evaluation location and NW (310°) for the boundary condition furthest away.

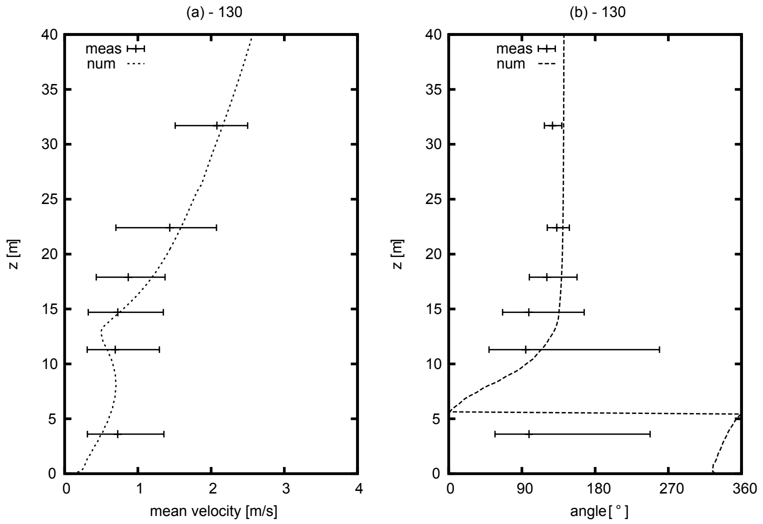

Figure 31: (a) Mean velocity for 130° inflow condition compared to the measurement levels. Error-bars indicate minimum and maximum measured values. (b) Wind angles for the levels

Figure 31a shows the mean velocity profile and Figure 31b, the corresponding angles in the street canyon during SE wind. The angles vary greatly at a height of 10 m - 17 m. The large variance is caused by the slanting roof located upwind, which changes the turbulence and vortex structure significantly (Huang et al., 2009). The mean velocities are in good accordance with the measurements, except for the lowest measurement 3.6 m above ground. In this case, the modelled data under-predicts the velocity and the resulting angle does not correspond to the measurements. However, this measurement location has to be interpreted critically, as the numerical approach did not incorporate traffic introduced velocities or turbulence.

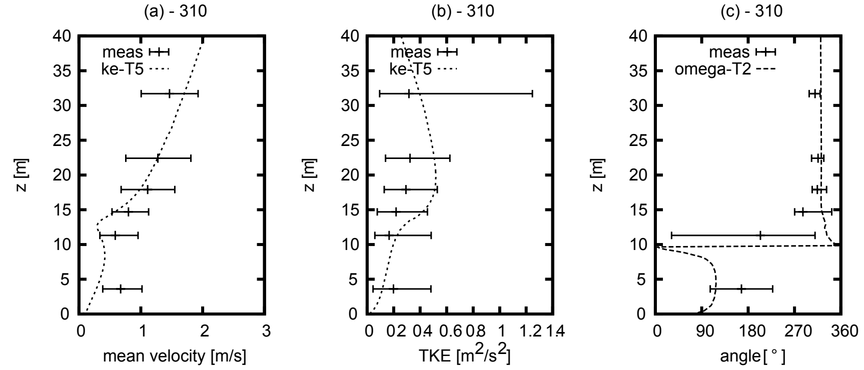

Figure 32: (a) Mean velocity for 310° inflow condition compared to the measurement levels. Error-bars indicate minimum and maximum measured values. (b) TKE (c) angles for the levels

Figure 32 shows the comparison for the NW inflow conditions and Figure 32b the TKE profile. The shape of the profile corresponds well with the measurements, but over-predicts the TKE in the region with strong shear flows (between 15 and 20 m height). This is a known problem with the $k - \epsilon$ turbulence model (Shih et al., 1995). The velocity is also under-predicted, but in this case the angle is except on the roof level adequately resolved.

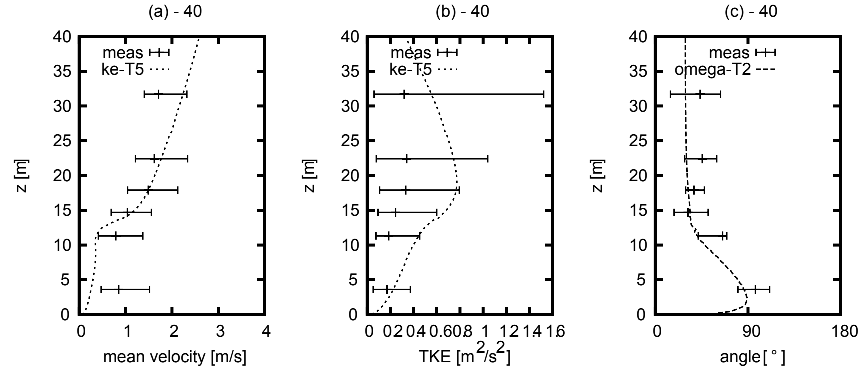

Figure 33: (a) Mean velocity for 40° inflow condition compared to the measurement levels. Error-bars indicate minimum and maximum measured values. (b) angles for the levels

Figure 33 shows the profiles for the NE inflow, where the studied location is nearer than in the NW case. The velocity profiles, TKE and angles are in good accordance, but show the same disadvantages as observed for the NW inflow conditions. Furthermore, there were no apparent differences between the conditions

(NW and NE), despite the different distance to the boundaries.
The analysis shows that the steady-state solution simulates the flow field in good accordance with the measurements, especially when it is taken into account that the measurement location was located near a building wall. Numerical flow fields near walls are influenced by the wall functions and hence more complicated to model because of the changing properties in near-wall flows. Based on this it can be assumed that the results are able to capture the main characteristics of the flow fields compared to the real conditions.

14.3. Transient approach results

To drive the inventory of steady-state flow fields, a time-step of 4 min and a randomly chosen 6 day period (2.1.2002 - 7.1.2002) were used. If direction changes significantly in one step, the 4 min period could be too short, as mentioned in section 14.1. The measurements from the highest point of the measurement tower (32.7 m above ground) were used.

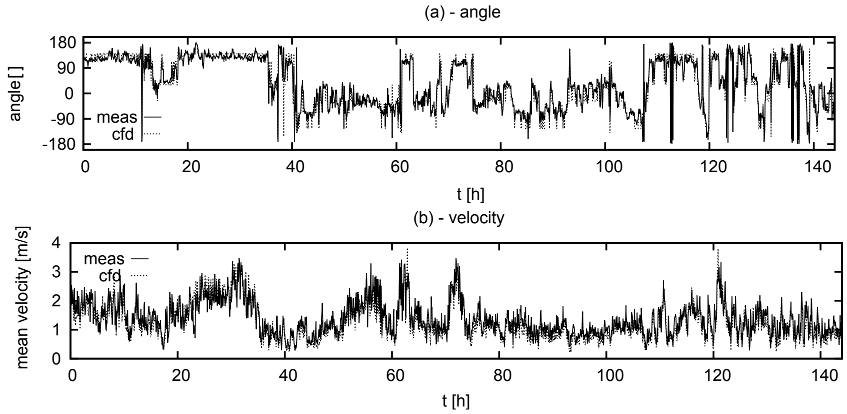

Figure 34: (a) Flow angles (b) mean velocity at 22.4 m above ground for measured and modelled time period (2.1.2002 - 7.1.2002)

The modelled and measured angles at 22.4 m above ground are shown in Figure 34a and the velocities in Figure 34b, both parameters show a good match.

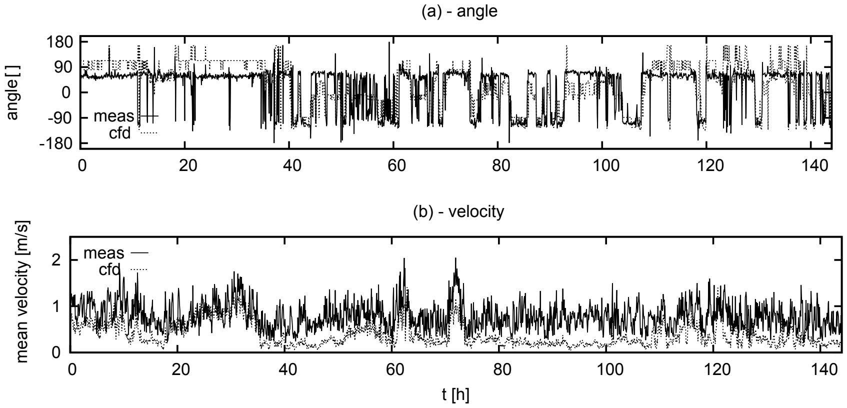

Figure 35: (a) Flow angles (b) mean velocity at 11.3 m (within the street canyon) above ground for measured and modelled time period (2.1.2002 - 7.1.2002)

Figure 35 shows the flow angles and mean velocities measured and modelled for the measurement position 11.4 m above ground, which is located in the street canyon approximately 4 m from the roof top. The velocity magnitude is underestimated (Figure 35b). Although the angle trend shows that the modelled data represents the real flow patterns very well, the offset in the angles indicates that smaller wind sectors (< 30°) should be used for further studies.

15. Conclusion

This study had the goal to show an approach to modelling flow patterns in an urban area with a large extent and a high temporal and spatial resolution. The requirements for creating a pseudo-transient flow-field were tested on a small part of the study site by using a fully resolved transient approach. It was found that changes in inflow conditions lead to changes within 2 min in the lower levels of the street canyon. Therefore, the driver of the inventory has to be significantly higher. A simple meshing technique for urban CAD data with inconsistent volumes was successfully implemented. This technique makes it possible to mesh complex urban geometries and retrieve ideal CFD meshes with hexahedral elements with higher refinement near walls. The meshes were used to model discrete steady-state wind conditions in part of the city of Basel, Switzerland, and to build an inventory of flow fields for 30° wind angles. The single steady-state solutions were validated using BUBBLE field measurements in a deep street canyon. In general, a good agreement was found between the modelled and measured values, with only the lowest measurement point showing some discrepancy for a few angles. A reason for this could be that the model did not incorporate the effect of traffic-induced velocities and traffic-related turbulence. For a future studies, the traffic could be modelled by source terms at street level. The TKE values show systematic over-prediction, which is a known artifact of the standard $k - \epsilon$ model that might be avoided by using a $k - \omega$ model in future applications (Menter, 1994).

An inventory encompassing 12 steady-state solutions was driven by experimental field measurements to create flow fields. As the flow-field inventory was constructed by joining 12 steady-state solutions, the resulting solution was termed *pseudo-transient*. One randomly chosen 6 day time-period was modelled and a very good accordance between the pseudo-transient results and the measurement data could be found with a small under-estimation of the velocity magnitudes within the street canyon. Nevertheless it is recommended for future studies to model with angle sectors smaller than 30° or interpolate in order to obtain a finer distinction in the inventory. Although the measurement tower was located near a building wall, the model was able to reproduce the measured values to a high degree.

The approach demonstrated here enables various insights in the urban meteorology: (a) (pseudo) transient results facilitate the interpretation of measurements, for example by retrieving the areas of influence or potential sources of pollutants, (b) the pseudo-transient data can also be used to calculate the transport of released fluids or particles, and (c) the small computational effort of the method to create transient flow fields with a high temporal resolution enables release studies in cases of emergency or for risk assessment purposes.

Part VII.
Conclusion and synopsis

The different study cases show the ability of CFD methods to model processes in the atmospheric roughness layer. It is shown that they can be used to support the interpretation of measurements and to derive parameters that are difficult to measure. They permit the simulation of dispersion and transport of pollutants and therefore give an insight into processes occurring in the air otherwise difficult to detect.

Derivation of parameters The combination of CFD methods and an experimental setup (part III) demonstrated the possibility to derive parameters, such as the wall shear or turbulence intensities within the experimental setup, which are otherwise difficult to obtain. The derived parameters were used to study phenomena, such as detachment of soil particles and geometry modifications of a wind-tunnel. Transported particles were measured at two shifted locations at the outlet of the wind-tunnel, whereby a skewed distribution was found. Particle detachment characteristics were obtained from the model environment and compared to measured values from which the cause of the distribution could be derived. Furthermore, the deposition characteristics (creep, saltation and suspension) were intensively studied by simulation and comparison with the measured data. The CFD approach was shown to be a good technique to derive qualitative descriptions of parameters otherwise not measurable, or only obtainable with great effort.

Cause of phenomena Measurements can show phenomena that cannot be fully explained based only on the gathered data, for example pollen distributions behind a windbreak that show a parabolic distribution on the lee-side of the windbreak (part V), strong gradients of CO_2 concentration around a building (part IV) or asymmetric particle detachment in an experimental setup (part III). Such phenomena can be explained by modelling the corresponding wind patterns. The CO_2 concentration difference between the street-side of a large building and the backyard could be associated with the wind patterns on the street side and their capabilities to transport traffic-emitted CO_2 to the measurement location (part IV). New knowledge of measured phenomena can also be obtained, as in the case of pollen distributions on the lee-side of a windbreak. By resolving the background concentration, a dependency between the settlement location and the altitude at which particles approach the stand could be derived (part V).

Bridge The history of CFD development explains the link of the methods and software solutions with engineering applications. The bridge between engineering applications and environmental flows was introduced in section 4 and critically reviewed in Blocken et al. (2007). As this thesis has shown, CFD can be employed to model environmental processes in the roughness layer, where complex topology hinders the application of meso-scale models. This enables the detection of phenomena otherwise not discernible, such as the suspension and settlement characteristics of pollen dependent on the ground texture on the lee-side of a stand (part V). Such phenomena are easiest to obtain, sometimes only obtainable, by numerical approaches, as these provide the ability to study the temporal and spatial processes in great detail.

Scales Pollutant concentrations in urban environments are not only influenced by street canyons / micro-γ scale processes, but are also subject to influences operating on larger scales. Pollutants emitted at street level can be transported to adjoining street canyons making it necessary to capture the dynamics, not only in one particular street canyon, but also on the neighborhood scale. Therefore, the modelling of large spatial extents with a high spatial and temporal resolution enables to study such phenomena. This leads to some technical difficulties, such as the generation of suitable meshes or the insufficient computational resources to study the temporal development and processes involved. Therefore, a simple and robust mesh technique was developed and implemented. The mesh technique (part 6.2.2) and an alternative approach to transient calculations (part VI) enabled the simulation over a large extent with high spatial and temporal resolution.

Assumptions The assumption of neutral conditions, neglecting thermal effects on the flow, leads to a series of simplifications in the CFD method and lower computational costs. The assumption is appropriate in urban areas (Lundquist and Chan, 2006). The study of the vertical measured velocity profiles 100 m and 350 m behind a porous windbreak showed no dependency on the stability during advection dominated flow situations, as shown in part V. This supports the assumption that neutral conditions are also suitable for vegetation roughness elements.

Validation As discussed in section 1, many studies use either experimental (e.g. from wind tunnels) or measurement data (e.g. from field campaigns) to validate simulations in environmental applications. When comparing field measurements with RANS results, it is important to select the appropriate average time-period for the Reynolds decomposition. By a detailed comparison of field measurement data with the numerical data, a recommendation could be made for the validation in urban areas. All phenomena studied in this thesis were compared with (field) measurements. The flow patterns for the case described in part IV could only indirectly be compared based on the measurement of CO_2 concentrations and an ongoing project now shows the correctness of the obtained wind fields (Lietzke, 2011).

Roughness This thesis shows the successful implementation of three types of roughness elements: *sub-grid*, *impermeable* and *porous*. Real roughness elements were used and the modelled results compared to in-situ measurements. The modelling approach involves a number of clearly defined parameters (section 4). The results show that CFD methods are able to model even complex flow patterns in good accordance with field measurements.

The free insight The numerical, three-dimensional flow-fields provide more details on the evolving processes of dispersed and transported gases or particles than other approaches. The extensive use of open-source software packages, and their parallel computing capabilities, enables this view with a comparably low cost. Furthermore, open-source codes can be modified and extended to deal with different research topics. They also permit to verify (a free view) the implementation, which is an important requirement for research applications.

15.1. Shortcomings

Due to the assumptions that had to be made, the study neglects the influence of thermal effects. This means that the applied methods will not be able to model the evolving wind patterns accurately, especially on windless days in urban environments. The steps necessary to close this gap, especially on a neighborhood scale, introduce some difficulties of their own. The influence of radiation must be incorporated by radiation models (e.g. Monte-Carlo methods or similar) or at least be parameterised. Because free convection occurs close to building walls or the ground surface, the material properties must be known over the whole extent of the city. In addition, the near-wall regions must be numerically resolved. Information on the texture of building walls is normally not obtainable from urban CAD models. These are topics dealt with in several research studies (Arnfield and Grimmond, 1998; Martilli et al., 2002; Harman and Belcher, 2006; Grimmond et al., 2010).
CFD methods, as well as most of the numerical models, have some restrictions: CFD calculations are dependent on their initial and boundary conditions, where many uncertainties exist (Blocken et al., 2007; Gorlé, 2010). The representation of atmospheric conditions with steady-state solutions is a further strong simplification, as phenomena such as gust winds, were neglected. Such effects can dominate dispersion processes significantly, such as the release and dispersion of pollen. Furthermore, the RANS approach neglects such unsteadiness, compared to LES (Xie and Castro, 2006). Furthermore, the applied eddy-viscosity turbulence model methods are based on some general assumptions, such as an isotropic turbulence (section 5.3.1). In the dispersion and transport modelling approaches, chemical processes, as well as effects of roughness elements on particles were not incorporated, this includes the effect leaves and branches have on pollen (Mckibbin, 2006).

15.2. Outlook

15.2.1. Lagrangian trajectories

The limited spatial resolution of point measurements makes the interpretation of measured pollutant concentration in urban areas complex (part IV). Knowledge of the source areas or the path-lines that show where the fluid comes from, is key to understanding not only the mechanisms for the transport, but also the interpretation of measurements in such heterogeneous areas. As suggested by Christen (2005), a backward Lagrangian approach could help to close this gap.

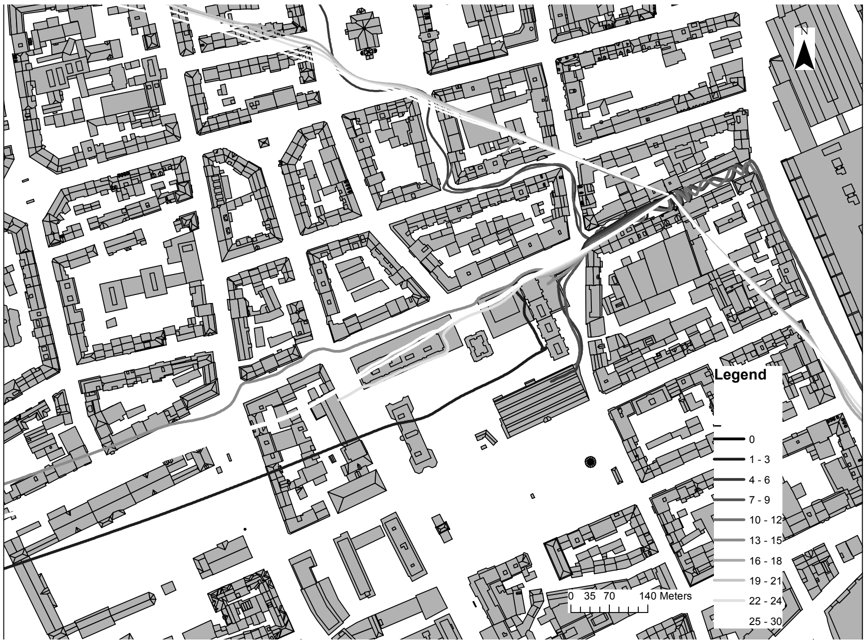

Figure 36: Backward trajectories during 280°, 250° and 130° wind for the different measurement points. The shading defines the altitude of the points (light: high, dark: low)

Figure 36 shows the backward trajectories for the measurement locations at a BUBBLE site during $280°, 250°$ and $130°$ wind conditions. The trajectories ending in points $z < 10\,\mathrm{m}$ are from fluid passing through the surrounding streets, whereas trajectories ending in higher points measure flow from above the urban canopy layer. Figure 36 also shows a vortex developed in the street canyon. Such vortices have the ability e.g. to transport the fluid trapped in the street canyon along the street whereby an enrichment of emitted pollutants from the street occurs (part IV).

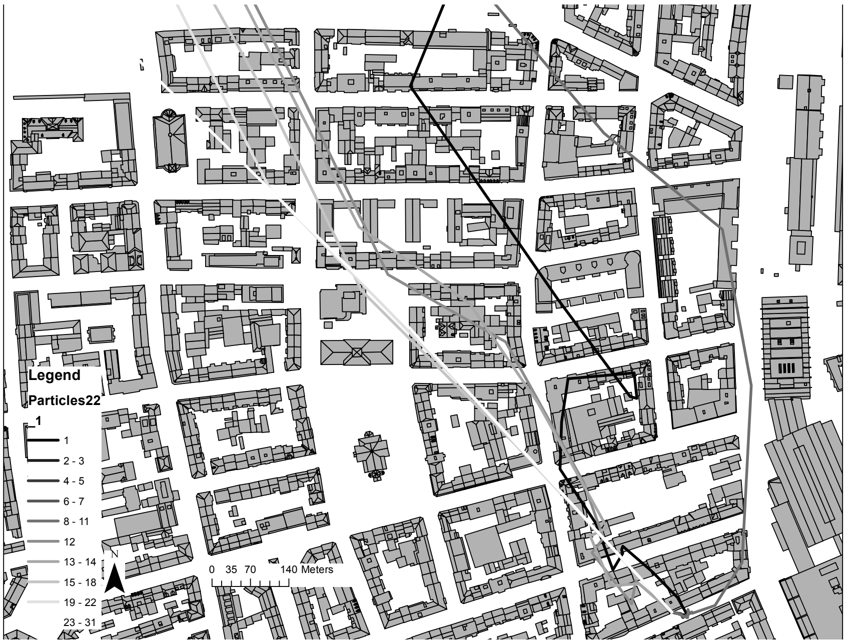

Figure 37: Backward trajectories for pseudo-transient result during a randomly chosen time period. The color defines the altitude of the points

Figure 37 shows the backward trajectories for steady-state simulations, but the pollutant transport can also be strongly influenced by the wind patterns, which develop over time. Therefore, the pseudo-transient flow-field of section (part VI) can be used to simulate the backward trajectories within a pseudo-transient flow-field. In such a way, the transient results allow to estimate the path-line of a measured pollutant concentration, resolving the necessary flow patterns.

Field measurements are essential for further improvement of numerical possibilities, therefore this thesis emphasizes the need for more field campaigns in the atmospheric roughness layer, especially in urban areas, where the flow patterns are very complex. It would be very interesting to design a field campaign based on model results, whereby the measurement locations could be placed according the obtained numerical results. As increasing computational resources in the future will provide more and more capabilities it will be feasible to model higher spatial extents, up to a neighborhood scale, and therefore close a gap between meso-scale / regional modelling and the explicit resolution of processes in the roughness layer. This thesis introduced approaches to model all three types of roughness elements and therefore enables to model the relevant, wind-induced processes in the roughness layer. The combination of the *sub-grid* and *porous* with the *impermeable* methods will enable the simulation of urban micro-meteorologic phenomena in all parts of a city, including regions with vegetation, such as alleys or parks, as well as the according dispersion and transport processes. They could be modelled over a long time and large spatial extent with a high resolution. The obtained flow patterns enable to model dispersion and transport of gaseous fluids and solid particles, e.g. dominating exhausts in urban areas, which influence our climate and health. Furthermore, other research topics or applications can use the progress in this field: dispersion assessment in sudden release of toxic exhausts, risk assessment or control of the micro-climate in cities by appropriate city development and architectural adaptions.

15.3. Conclusive remark

Each research approach conducted in the past has its limitations in the study of environmental flows in the complex roughness layer of the ABL. Each numerical approach needs to be validated with measurements, otherwise the significance of its findings is not clear. However, the combination of measurements and physically-based numerical approaches, such as CFD methods, can give new insights into the wind-related processes in the roughness layer, especially when field measurements are used for validation or as input.

16. Bibliography

Aase, J. (1974), ‘Tall wheatgrass barriers and winter wheat response’, *Agricultural Meteorology* **13**, 321–338.

Allen, L. (1968), ‘Turbulence and wind speed spectra within a Japanese larch plantation’, *Journal of Applied Meteorology* **7**, 73–78.

Andronopoulos, S., Grigoriadis, D., Robins, A., Venetsanos, A., Rafailidis, S. and Bartzis, J. (2002), ‘Three-dimensional modelling of concentration fluctuations in complicated geometry’, *Environmental Fluid Mechanics* **1**, 415–440.

ANSYS (2006), *ANSYS CFX Reference Manual*, 11.0 edn, ANSYS Inc.

Arnfield, A. and Grimmond, C. (1998), ‘An urban canyon energy budget model and its application to urban storage heat flux modeling’, *Energy and Buildings* **27**, 61–68.

Baldocchi, D., Falge, E., Gu, L., Olson, R., Hollinger, D., Running, S., Anthoni, P., Bernhofer, C., Davis, K., Evans, R., Fuentes, J., Goldstein, A., Katul, G., Law, B., Lee, X., Malhi, Y., Meyers, T., Munger, W., Oechel, W., U, K. P., Pilegaard, K., Schmid, H., Valentini, R., Verma, S., Vesala, T., Wilson, K. and Wofsy, S. (2001), ‘Fluxnet: A new tool to study the temporal and spatial variability of ecosystem-scale carbon dioxide, water vapor, and energy flux densities’, *Bulletin of the American Meteorological Society* **82**(11), 2415–2434.

Barlow, J. and Belcher, S. (2002), ‘A wind tunnel model for quantifying fluxes in the urban boundary layer’, *Boundary-Layer Meteorology* **104**, 131–150.

Blocken, B., Stathopoulos, T. and Carmeliet, J. (2007), ‘CFD simulation of the atmospheric boundary layer: wall function problems’, *Atmospheric Environment* **41**, 238–252.

Bourdin, P. and Wilson, J. (2008), ‘Windbreak aerodynamics: is computational fluid dynamics reliable?’, *Boundary-Layer Meteorology* **126**, 181–208.

Bradley, E. and Mulhearn, P. (1983), ‘Development of velocity and shear stress distribution in the wake of a porous shelter fence’, *Journal of Wind Engineering & Industrial Aerodynamics* **15**, 145–156.

Britter, R. and Hanna, S. (2003), ‘Flow and disperion in urban areas’, *Annu. Rev. Fluid Mech.* **35**, 469–496.

Brook, R. (1972), ‘The measurement of turbulence in a city environment’, *Journal of Applied Meteorology* **11**, 443–450.

Burge, A. and Rogers, C. (2000), ‘Outdoor allergens’, *Environmental Health Perspectives* **108**, 653–659.

Calhoun, R., Gouveia, F., Shinn, J., Chan, S., Stevens, D., Lee, R. and Leone, J. (2004), 'Flow around a complex building: comparison between experiments and a Reynolds-averaged Navier-Stokes approach', *Journal of Applied Meteorology* **43**, 696–710.

Carpentieri, M., Robins, A. and Baldi, S. (2009), 'Three-dimensional mapping of air flow at an urban canyon intersection', *Boundary-Layer Meteorology* **133**, 277–296.

Castro, I., Cheng, H. and Reynolds, R. (2006), 'Turbulence over urban-type roughness: deductions from wind-tunnel measurements', *Boundary-Layer Meteorology* **118**, 109–131.

Chang, C.-H. and Meroney, R. (2003), 'Concentraton and flow distributions in urban street canyons: wind tunnel and computational data', *Journal of Wind Engineering and Industrial Aerodynamics* **91**, 1141–1154.

Charlson, R., Schwartz, S., Hales, J., Cess, R., Jr., J. C., Hansen, J. and Hofmann, D. (1992), 'Climate forcing by anthropogenic aerosols', *Science* **255**(5043), 423–430.

Christen, A. (2005), Atmospheric turbulence and surface energy exchange in urban environments, Stratus 11, 2005, Institut of Meteorology, Climatology and Remote Sensing, University of Basel.

Chu, A., Kwok, R. and Yu, K. (2005), 'Study of pollution dispersion in urban areas using computational fluid dynamics (CFD) and geographic information system (GIS)', *Environmental Modelling and Software* **20**, 273–277.

Cleugh, H. (1998), 'Effects of windbreaks on airflow, microclimates and crop yields', *Agroforestry Systems* **41**, 55–84.

Coirier, W., Fricker, D., Furmanczyk, M. and Kim, S. (2005), 'A computational fluid dynamics approach for urban area transport and dispersion modeling', *Environmental Fluid Mechanics* **5**, 443–479.

Dalpé, B. and Masson, C. (2009), 'Numerical simulation of wind flow near a forest edge', *Journal of Wind Engineering and Industrial Aerodynamics* **97**, 228–241.

D'Amato, G., Liccardi, G., D'Amato, M. and Cazzola, M. (2002), 'Outdoor air pollution, climatic changes and ellergic bronchial asthma', *European Respiratory Journal* **20**, 763–776.

Davidson, M., Snyder, W., Jr, R. L. and Hunt, J. (1996), 'Wind tunnel simulations of plume dispersion through groups of obstacles', *Atmospheric Environment* **30**(22), 3715–3731.

Ecke, R. (2005), 'The turbulence problem - an experimentalist's perspective', *Los Alamos Science* (29), 124–141.

Endalew, A., Hertog, M., Delele, M., Baetens, K., Persoons, T., Baelmans, M., Ramon, H., Nicolai, B. and Verboven, P. (2009), 'CFD modelling and wind tunnel validation of airflow through plant canopies using 3d canopy architecture', *International Journal of Heat and Fluid Flow* **30**, 356–368.

Feddersen, B. (2005), Wind tunnel modelling of turbulence and dispersion above tall and highly dense urban roughness, PhD thesis, Swiss Federal Institute of Technology Zurich.

Feigenwinter, C. (1999), The vertical structure of turbulence above an urban canopy, Stratus 7, 2000, Institut of Meteorology, Climatology and Remote Sensing, University of Basel.

Finnigan, J. and Bradley, E. (1983), 'The turbulent kinetic energy budget behind a porous barrier: an analyis in streamline co-ordinates', *Journal of Wind Engineering and Industrial Aerodynamics* **15**, 157–168.

Fister, W., Iserloh, T., Ries, J. and Schmidt, R.-G. (2011), 'Comparison of rainfall characteristics of a small portable rainfall simulator and a combined portable wind and rainfall simulator', *Zeitschrift für Geomorphologie* **55**, 109–126. Zeitschrift fuer Geomorphologie.

Foken, T. and Wichura, B. (1996), 'Tools for quality assessment of surface-based flux measurements', *Agricultural and Forest Meteorology* **78**, 83–105.

Franke, J., Hirsch, C., Jensen, A., Krüs, H., Schatzmann, M., Westbury, P., Miles, S., Wisse, J. and Wright, N. (2004), Recommendations on the use of cfd in predicting pedestrian wind environment, *in* 'COST Action C14 "Impact of Wind and Storms on City Life and Built Environment" Working group 2 - CFD techniques'.

Fritsching, U. (2004), *Spray Simulation*, Cambridge University Press.

Gjesing, R., Hattel, J. and Fritsching, U. (2009), 'Coupled atomization and spray modelling in the spray forming process using openFOAM', *Engineering Applications of Computational Fluid Mechanics* **3**, 471–486.

Gorlé, C. (2010), CFD modelling of pollutant dispersion in urban environments, PhD thesis, University of Antwerp.

Grant, R. H. (1983), 'The scaling of flow in vegetative structures', *Boundary-Layer Meteorology* **27**, 171–184.

Green, S., Grace, J. and Hutchings, N. (1995), 'Observations of turbulent air flow in three stands of widely spaced sitka spruce', *Agricultural and Forest Meteorology* **74**, 205–225.

Grimmond, C., Blackett, M., Best, M., Baik, J.-J., Blecher, S., Beringern, J., Bohnenstengel, S., Calmet, I., Chen, F., Coutts, A., Dandou, A., Fortuniak, K., Gouvea, M., Hamdi, R., Hendry, M., Kanda, M., Kawai, T., Kawamoto, Y., kondo, H., Krayenhoff, E., Lee, S.-H., Loridan, T., Martilli, A., Masson, V., Mia, S., Oleson, K., Ooka, R., Pigeon, G., Porson, A., Ryu, Y.-H., Salamanca, F., Steeneveld, G., Tombrou, M., Voogt, J., Young, D. and Zhang, N. (2010), 'Initial results from phase 2 of the international urban energy balance model comparison', *International Journal of Climatology* **31**(2), 244–272.

Grimmond, C., King, T., Cropley, F., Nowak, D. and Souch, C. (2002), 'Local-scale fluxes of carbon dioxide in urban environments: methodological challenges and results from chicago', *Environmental Pollution* **116**, 243–254.

Grimmond, C. and Oke, T. (1999), 'Aerodynamic properties in urban areas derived from analysis of surface form', *Journal of Applied Meteorology* **38**, 1262–1292.

Grossman, G. and Krueger, A. (1995), 'Economic growth and the environment', *Quarterly Journal of Economics* **110**(2), 353–377.

Guilloteau, E. and Mestayer, P. (2000), 'Numerical simulations of the urban roughness sub-layer: a first attempt', *Environmental Monitoring and Assessment* **65**, 211–219.

Hagen, L., Skidmore, E., Miller, P. and Kipp, J. (1981), 'Simulation of effect of wind barriers on airflow', *Transactions of the ASAE* **24**(4), 1002–1008.

Hanna, S. R., Brown, M. J., Camelli, F. E., Chan, S. T., Coirier, W. J., Hansen, O. R., Huber, A. H., Kim, S. and Reynolds, R. M. (2006), 'Detailed simulations of atmospheric flow and dispersion in downtown manhatten - an application of five computational fluid dynamics models', *American Meteorological Society* pp. 1713–1726.

Harlow, F. H. and Welch, J. E. (1965), 'Numerical calculation of time-dependent viscous incompressible flow of fluid with free surface', *The Physics of Fluid* **8**(12), 2182–2189.

Harman, I. and Belcher, S. (2006), 'The surface energy balance and boundary layer over urban street canyons', *Quarterly Journal of the Royal Meteorological Society* **132**, 2749–2768.

Heisler, G. M. and DeWalle, D. (1988), '2. Effects of windbreak structure on wind flow', *Agricultural and Forest Meteorology* **22/23**, 41–69.

Helbig, N., Vogel, B., Vogel, H. and Fiedler, F. (2004), ‘Numerical modelling of pollen dispersion on the regional scale’, *Aerobiologia* **3**, 3–19.

Hestenes, M. R. and Stiefel, E. (1952), ‘Methods of conugate gradients for solving linear systems’, *Journal of Research of the National Bureau of Standards* **49**(6), 409–436.

Hirst, J. (1952), ‘An automatic volumetric spore trap’, *Ann. Appl. Biol.* **39**, 257–265.

Huang, Y., Hu, X. and Zeng, N. (2009), ‘Impact of wedge-shaped roofs on airflow and pollutant dispersion inside urban street canyons’, *Building and Environment* **44**, 2335–2347.

Hunter, L., Johnson, G. and Watson, I. (1992), ‘An investigation of three-dimensional characteristics of flow regimes within the urban canyon’, *Atmospheric Environment* **26B**(4), 425–432.

Hunter, L., Watson, I. and Johnson, G. (1991), ‘Modelling air flow regimes in urban canyons’, *Energy and Buildings* **15-16**, 315–324.

Incropera, F. and Witt, D. D. (2002), *Fundamentals of heat and mass transfer*, fifth edn, John Wiley and Sons.

Issa, R. (1985), ‘Solution of the implicitly discretised fluid flow equations by operator-splitting’, *Journal of Computational Physics* **62**, 40–65.

Janjic, Z., Jr., J. G. and Nickovic, S. (2001), ‘An alternative approach to nonhydrostatic modeling’, *Monthly Weather Review* **129**, 1164–1178.

Karim, A., Nolan, P. and Qubian, A. (2008), ‘Meshing effects on CFD modelling of atmospheric flow over buildings situated on ground with high terrain’, *WIT Transactions on Ecology and the Environment* **116**, 29–38.

Katul, G. G., Mahrt, L., Poggi, D. and Sanz, C. (2004), ‘One- and two-equation models for canopy turbulence’, *Boundary-Layer Meteorology* **113**, 81–109.

Kim, S.-E. and Boysan, F. (1999), ‘Application of CFD to environmental flows’, *Journal of Wind Engineering and Industrial Aerodynamics* **81**, 145–158.

Kobayashi, M., Pereira, J. and Siqueira, M. (1994), ‘Numerical study of the turbulent flow over and in a model forest on a 2d hill’, *Journal of Wind Engineering and Industrial Aerodynamics* **53**, 357–374.

Krischok, D. (2009), Kopplung eines 3D-Stadtmodell-Visualisierungssystems mit einem Finite-Elemente-Simulationssystem, Master’s thesis, Universität Potsdam Mathematisch-Naturwissenschaftliche Fakultät Hasso-Plattner-Institut für Softwaresystemtechnik.

Kundu, P. K. and Cohen, I. (2002), *Fluid Mechanics*, second edition edn, Academic Press.

Lalic, B. and Mihailovic, D. (2004), 'An emprical relation describing leaf-area density inside the forest for environmental modeling', *Journal of Applied Meteorology* **43**(4), 641–645.

Launder, B. and Spalding, D. (1974), 'The numerical computation of turbulent flows', *Computer Methods in Applied Mechanics and Engineering* **3**(2), 269–289.

Leach, M. (2005), Final report for the joint urban 2003: Atmospheric disperion study in Oklahoma City: Lawrence Livermore National Laboratory participation, Technical report, Lawrence Livermore National Laboratory.

Li, X., Liu, C., Leung, D. and Lam, K. (2006), 'Recent progress in CFD modelling of wind field and pollutant transport in street canyons', *Atmospheric Environment* **40**, 5640–5658.

Li, X.-X., Liu, C.-H. and Leung, D. (2009), 'Numerical investigation of pollutant transport characteristics inside deep urban street canyons', *Atmospheric Environment* **43**, 2410–2418.

Liang, L., Xiaofeng, L., Borong, L. and Yingxin, Z. (2006), 'Improved k-ϵ two-equation turbulence model for canopy flow', *Atmospheric Environment* **40**, 762–770.

Lietzke, B. (2011), 'Dynamik der urbanen CO_2-Verteilung - Teil 1: Messungen in einer Strassenschlucht', *Regio Basiliensis* **52**, 37–44.

Louka, P., Blecher, S. and Harrison, R. (2000), 'Coupling between air flow in streets and the well-developed boundary layer aloft', *Atmospheric Environment* **34**, 2613–2621.

Lundquist, J. and Chan, S. (2006), 'Consequences of urban stability conditions for computational fluid dynamics simulations of urban dispersion', *Journal of Applied Meteorology and Climatology* **46**, 1080–1097.

Macdonald, R., Griffiths, R. and Hall, D. (1998), 'A comparison of results from scaled field and wind tunnel modelling of dispersion in arrays of obstacles', *Atmospheric Environment* **22**, 3845–3862.

Mandrioli, P., Comtois, P. and Levizzani, V. (1998), *Methods in aerobiology*, Pitagora Editrice, Bologna, Italy.

Martilli, A., Clappier, A. and Rotach, M. (2002), 'An urban surface exchange parameterisation for mesoscale models', *Boundary-Layer Meteorology* **104**, 261–304.

Mckibbin, R. (2006), ‘Modelling pollen distribution by wind through a forest canopy’, *JSME International Journal* **49**(3), 583–589.

McNaughton, K. (1988), ‘1. Effects of windbreaks on turbulent transport and microclimate’, *Agriculture, Ecosystems and Environment* **22/23**, 17–39.

Menter, F. (1994), ‘Two-equation eddy-viscosity turbulence models for engineering applications’, *AIAA Journal* **32**(8), 1598–1605.

Michel, D., Gehrig, R., Rotach, M. and Vogt, R. (2010), MicroPoem: Experimental investigation of birch pollen emission, *in* ‘19th Symposium on Boundary Layer and Turbulence, Keystone, Colorado, 2 - 8 August’.

Michel, D., Gehrig, R., Rotach, M. and Vogt, R. (2011*a*), MicroPoem: Characteristics of birch pollen dispersion downwind of an isolated source, *in* ‘COST Action ES0603 Final Management Commitee conference, Berlin, Germany, 14 - 15 October’.

Michel, D., Gehrig, R., Rotach, M. and Vogt, R. (2011*b*), ‘MicroPoem: Experimentelle Untersuchung der mikro-meteorologischen Einflüsse auf die Birkenpollenemission im Rhonetal’, *Regio Basiliensis* **52**, 55–62.

Mockus, A., Fielding, R. and Herbsleb, J. (2002), ‘Two case studies of open source software development: Apache and Mozilla’, *ACM Transactions on Software Engineering and Methodology* **11**(3), 309–346.

Molina, M. and Molina, L. (2004), ‘Megacities and atmospheric pollution’, *Journal of the Air & Waste Management Association* **54**(6), 644–680.

Monn, C. (2001), ‘Exposure assemssment of air pollutants: a review on spatial heterogeneity and indoord/outdoor/personal exposure to suspended particulate matter, nitrogen diocide and ozone’, *Atmospheric Environment* **35**(1-32).

Moonen, P., Dorer, V. and Carmeliet, J. (2011), ‘Evaluation of the ventilation potential of courtyards and urban street canyons using RANS and LES’, *Journal of Wind Engineering and Industrial Aerodynamics* **99**, 414–423.

Murena, F., Favale, G., Vardoulakis, S. and Solazzo, E. (2009), ‘Modelling dispersion of traffic pollution in a deep street canyon: application of CFD and operational models’, *Atmospheric Environment* **43**, 2303–2311.

Neifytou, P., Venetsanos, A., Rafailidis, S. and Bartzis, J. (2006), ‘Numerical investigation of the pollution dispersion in an urban steet canyon’, *Environmental Modelling and Software* **21**, 525–531.

Oke, T. (1988), ‘Street design and urban canopy layer climate’, *Energy and Buildings* **11**, 103–113.

Oke, T. (2006), Initial guidance to obtain representative meteorological observations at urban sites, *in* 'Instruments and observing methods - Report No. 81', WMO/TD-No. 1250.

OpenFOAM (2009), *OpenFOAM The Open Source CFD Toolbox - Programmers' Guide*, version 1.6 edn, OpenCFD Ltd.

Orlanski, I. (1975), 'A rational subdivision of scales for atmospheric processes', *Bulletin of the American Meteorological Society* **56**, 527–530.

Packwood, A. (2000), 'Flow through porous fences in thick boundary layers: comparisons between laboratory and numerical experiments', *Journal of Wind Engineering and Industrial Aerodynamics* **88**, 75–90.

Paraview (2011).
URL: *http://www.paraview.org/*

Parra, M., Santiago, J., Martin, F., Martilli, A. and Santamaria, J. (2010), 'A methodology to urban air quality assessment during large time periods of winter using computational fluid daynamic models', *Atmospheric Environment* **44**, 2089–2097.

Pope, S. B. (2000), *Turbulent Flow*, Cambrige University Press.

Princevac, M., Baik, J.-J., Lie, X., Pan, H. and PARK, S.-B. (2010), 'Lateral channeling within rectangular arrays of cubical obstacles', *Journal of Wind Engineering and Industrial Aerodynamics* **98**, 377–385.

Raynor, G. (1971), 'Wind and temperature structure in a coniferous forest and contiguous field', *Forest Science* **17**(3), 350–363.

Richards, P. and Hoxey, R. (1993), 'Appropriate boundary conditions for computational wind engineering models using the k-ϵ turbulence model', *Journal of Wind Engineering and Industrial Aerodynamics* **46 and 47**, 145–153.

Richardson, L. (1922), *Weather prediction by numerical process*, Cambridge at the university press.

Richter, J. (2005), 'The Notebooks of Leonardo Da Vinci', Ebook.

Rohli, R. and Vega, A. (2008), *Climatology*, Jones and Barlett Publishers.

Rosenfeld, M., Marom, G. and Bitan, A. (2010), 'Numerical simulation of the airflow across trees in a windbreak', *Boundary-Layer Meteorology* **135**, 89–107.

Rotach, M. (1995), 'Profiles of turbulence statistics in and above an urban street canyon', *Atmospheric Environment* **29**(13), 1473–1486.

Rotach, M., Gryning, S.-E., Batchvarova, E., Christen, A. and Vogt, R. (2004), ‘Pollutant dispersion close to an urban surface - the BUBBLE tracer experiment’, *Meteorology and Atmospheric Physics* **87**, 39–56.

Rotach, M., Vogt, R., Bernhofer, C., Batchvarova, E., Christen, A., Clappier, A., Feddersen, B., Gryning, S., Martucci, G., Mayer, H., Miteva, V., Oke, T., Parlow, E., Richner, H., Roth, M., Roulet, Y., Ruffieux, D., Salmond, J., Schatzmann, M. and Voogt, J. (2005), ‘BUBBLE - an urban boundary layer meteorology project’, *Theoretical and Applied Climatology* **81**, 231–261.

Roth, M. (2000), ‘Review of atmospheric turbulence over cities’, *Quarterly Journal of the Royal Meteorological Society* **126**, 941–990.

Salim, S., Buccolieri, R., Chan, A. and Sabatino, S. D. (2011), ‘Numerical simulation of atmospheric pollutant dispersion in an urban street caynon: Comparison between RANS and LES’, *Journal of Wind Engineering and Industrial Aerodynamics* **99**, 103–113.

Santiago, J., Martin, F., Cuerva, A., Bezdenejnykh, N. and Sanz-Andrés, A. (2007), ‘Experimental and numerical study of wind flow behind windbreaks’, *Atmospheric Environment* **41**, 6406–6420.

Sanz, C. (2003), ‘A note on k-ϵ modelling of vegetation canopy air-flows’, *Boundary-Layer Meteorology* **108**, 191–197.

Schueler, S. and Schlünzen, K. (2006), ‘Modeling of oak pollen dispersal on the landscape level with a mesoscale atmospheric model’, *Environmental Model Assess* **11**, 179–194.

Shao, Y. (2008), *Physics and modelling of wind erosion*, 2nd revised and expanded edtition edn, Springer.

Shih, T.-H., Liou, W., Shabbir, A., Yang, Z. and Zhu, J. (1995), ‘A new k-ϵ eddy viscosity model for high Reynolds number turbulent flows’, *Computers Fluids* **24**(3), 227–238.

Singh, B., Hansen, B., Brown, M. and Pardyjak, E. (2008), ‘Evaluation of the QUIC-URB fast response urban wind model for a cubial building array and wide building street canyon’, *Environmental Fluid Mechanics* **8**, 281–312.

Sini, J., Anquetin, S. and Mestayer, P. G. (1996), ‘Pollutant dispersion and thermal effect in urban street canyons’, *Atmospheric Environment* **30**(15), 2659–2677.

Skjøth, C., Brandt, J., Christensen, J., Løfstrøm, P., Frohn, L., Geels, C., Hvidberg, M., Frydendall, J. and Hansen, K. (2006), THOR: An operational and integrated model system for air pollution and pollen forecasts, *in* ‘Proceedings of

8th International Congress on Aerobiology, "Towards a comprehensive vision"', Neuchâtel, Switzerland, 21-25 August 2006.

Sofiev, M., Siljamo, P., Ranta, H. and Rantio-Lehtimäki, A. (2006a), 'Towards numerical forecasting of long-range air transport of birch pollen: theoretical considerations and a feasability study', *International Journal Biometeorology* **50**, 392–402.

Sofiev, M., Siljamo, P., Valkama, I., Ilvonen, M. and Kukkonen, J. (2006b), 'A dispersion modelling system SI-LAM and its evaluation against ETEX data', *Atmospheric Environment* **40**, 674–685.

Sommerfeld, M. (1992), 'Modelling of particle-wall collisions in confined gas-particle flows', *International Journal of Multiphase Flow* **18**(6), 905–926.

Stadt, K. and Lieffers, V. (2000), 'Mixlight: a flexible light transmission model for mixed-species forest stands', *Agricultural and Forrest Meteorology* **102**, 235–252.

Stull, R. (2000), *Meteorology for Scientists and Engineers*, second edn, G. Garloson.

Tominaga, Y., Mochida, A., Yoshie, R., Kataoka, H., Nozu, T., Yoshikawa, M. and Shirasawa, T. (2008), 'Aij guidelines for practical applications of cfd to pedestrian wind environment around buildings', *Journal of Wind Engineering and Industrial Aerodynamics* **96**, 1749–1761.

Tsai, M. and Chen, K. (2004), 'Measurements and three-dimensional modeling of air pollutants dispersion in an urban street caynon', *Atmospheric Environment* **38**, 5911–5924.

Vardoulakis, S., Fisher, B. E. A., Pericleous, K. and Gonzalez-Flesca, N. (2003), 'Modelling air quality in street canyons: a review', *Atmospheric Environment* **37**, 155.182.

Venkatram, A. and Wyngaard, J. (1988), *Lectures on air pollution modeling*, American Meteorological Society, Boston.

Versteeg, H. and Malalasekera, W. (2007), *An introcudtion to Computational Fluid Dynamics*, second edn, Longman Scientific & Technical.

Vigiak, O., Sterk, G., Warren, A. and Hagen, L. (2003), 'Spatial modeling of wind speed around windbreaks', *Catena* **52**, 273–288.

Vogt, R., Eitel, J. and Parlow, E. (2006), Coupling of backyard to street canyon CO_2 concentrations, *in* '6th International Conference on Urban Climate ICUC-6', Sweden.

Voronovich, V. and Kiely, G. (2007), ‘On the gap in the spectra of surface-layer atmospheric turbulence’, *Boundary-Layer Meteorology* **122**, 67–83.

Wang, Y. and Zhang, K. (2009), ‘Modeling near-road air quality using a computational fluid dynamics model, CFD-VIT-RIT’, *Environmental Science Technology* **43**, 7778–7783.

Weber, S. and Weber, K. (2008), ‘Coupling of urban street canyon and backyard particle concentrations’, *Meteorologische Zeitschrift* **17**, 251–261.

Weller, H. G., Tabor, G., Jasak, H. and Fureby, C. (1998), ‘A tensorial approach to computational continuum mechanics using object-oriented techniques’, *Computers in Physics* **12**(6), 620–631.

Wilcox, D. C. (2000), *Basic Fluid Mechanics*, DCW Industries.

Wilson, N. R. and Shaw, R. H. (1977), ‘A higher order closure model for canopy flow’, *Journal of Applied Meteorology* pp. 1197–1205.

Xie, Z. and Castro, I. (2006), ‘LES and RANS for turbulent flow over arrays of wall-mounted obstacles’, *Flow, Turbulence and Combustion* **76**(3), 291–312.

Xie, Z. and Castro, I. P. (2009), ‘Large-eddy simulation for flow and dispersion in urban streets’, *Atmospheric Environment* **43**, 2174–2185.

Yang, Y. and Shao, Y. (2008), ‘Numerical simulations of flow and pollution dispersion in urban atmospheric boundary layers’, *Environmental Modelling and Software* **23**, 906–921.

Yassin, M., Kellnerova, R. and Janour, Z. (2009), ‘Numerical simulation on pollutant dispersion from vehicle exhaust in street configurations’, *Environmental Model Assess* **156**, 257–273.

Yeh, C.-P., Tsai, C.-H. and Yang, R.-J. (2010), ‘An investigation into the sheltering performance of porous windbreaks under various wind directions’, *Journal of Wind Engineering & Industrial Aerodynamics* **98**, 520–532.

Zhou, X., Brandle, J., Mize, C. and Takle, E. (2004), ‘Three-dimensional aerodynamic structure of a tree shelterbelt: Definition, characterization and working models’, *Agroforestry Systems* **63**, 133–147.

References of published articles not included

Part VIII.

Appendix

The attached CD contains:

- *Warm_bubble.mpg*: Short movie of a cold bubble in a neutral stratified atmosphere, cf. section 4.3.2.
- *Warm_bubble.mpg* Short movie of a warm bubble in a neutral stratified atmosphere, cf. section 4.3.2.
- *PartV_CFD_throughAtreeStand.avi*: Movie of particle dispersion behind a tree stand, cf. section V.

Comparison of CFD Results with Experimental Data within a Street Canyon: The Influence of Averaging Time

A. Gartmann, R. Vogt, M.D. Müller

Institute for Meteorology, Climatology and Remote Sensing, University of Basel, Switzerland

Motivation

- In urban areas local concentrations of pollutants are strongly influenced by flow patterns within street canyons
- Turbulent kinetic energy (TKE) plays an important role in dispersion dynamics
- Average time interval for Reynolds decomposition is a decisive parameter when comparing measurement with modelled data

Measurements

- Location: street canyon in Basel, Switzerland (Fig. 1)
- Using Basel Urban Boundary Layer Experiment data
- 3 dominating wind directions: 130°, 355° (cross canyon), 270° (along canyon)
- For each wind situation 3 velocity magnitudes low (<1 m/s), middle (1-2,5 m/s), high (> 2.5 m/s)

Assumptions

- Advection dominated flow situations (V > 0.8 m/s)
- Thermal neutral stability
- Reynolds Averaged Navier-Stokes equations apply
- Closure: two-equation model (k-epsilon, RNG k-epsilon) and Reynolds stress model (SSG)

Figure 1. Overview of street canyon with measurement tower

M. Roth

Numerics

- Mesher: ANSYS ICEM CFD, Solver: ANSYS CFX 11.1
- Geometrical representation: high resolution CAD model of buildings (Fig. 2)
- Boundary Conditions (BCs):
  > logarithmic for mean velocity
  > TKE: 1) constant shear stress
  2a) turbulence intensity 5% 2b) intensity = TKE at top of tower (31.7 m above street level)
- No significant differences between RNG k-epsilon and standard k-epsilon turbulence models
- SSG gives a good approximation for measured profiles of Reynolds stresses
- Using tetrahedral meshes with 3 prismatic layers on walls
- Average of 1 m mesh resolution (prism layer < 0.2 m resolution)

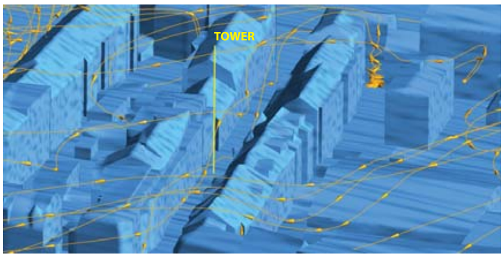

Figure 2. Streamlines and velocity vectors (130° , 2.5 m/s measured at top of tower)

Average Time Analysis

- Using 8 Δt time ranges: 1200, 600, 300, 150, 60, 30, 15, 6 s
- 80 days in analysis with floating scan interval of 30 s
- Exclude situations with trend in mean velocity
- Filter statistical stationarity situations
- No filter for other quantities, e.g. stability, frequencies

- Method to scale up the turbulence using
  a) higher intensity values for the TKE-BCs
  $I = \frac{u'}{U}$
  b) Richards & Hoxey (constant shear stress)
  $k = \frac{u_*}{\sqrt{C_\mu}}$

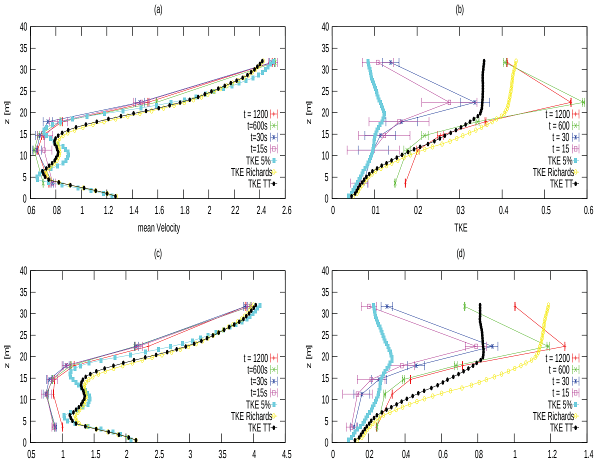

Figure 3. Profile with different BC and time average intervals. BCs with higher TKE lead to weaker correlation for mean velocity profiles

t = average time interval
TKE 5% = BC TKE intensity 5%
TKE Richards = BC TKE const. shear stress
TKE TT = BC TKE intensity @ Tower (31.7 m)

(a) mean velocity (Vmag = 2.5 m/s)
(c)mean velocity (Vmag = 4.1 m/s)
(b) TKE (Vmag = 2.5 m/s)
(d) TKE (Vmag = 4.1 m/s)

Velocity Magnitude and TKE

- Dependency between mean velocity and TKE as function of Δt
- Evolution of TKE is dependent on Δt (Fig. 4)
- statistically stationarity Δ->0: $\Delta\{\sigma_x^2(t_1....t_n)\} = \frac{\sigma_x^2}{\frac{1}{n}[\sigma_x^2(t_1)+...+\sigma_x^2(t_n)]}$

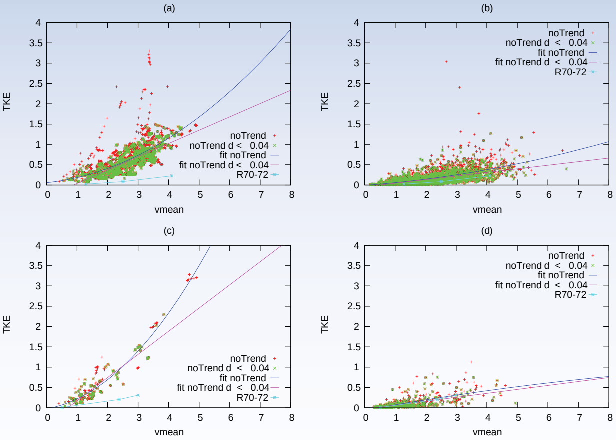

Figure 4. Mean velocities at 31.7 m above street level (a) 130° - Δt=1200s, (b) 130° - Δt=30s, (c) 355° - Δt=1200s, (d) 355° - Δt=30s; + no trend in mean velocity, x no trend in mean velocity & statistical stationary Δ->0

Flow Patterns - Cross-Sections N-S - 90° to Street Canyon

- Strong influence of wind directions on velocities and TKE profiles

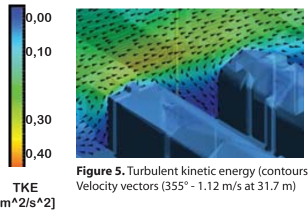

Figure 5. Turbulent kinetic energy (contours)
Velocity vectors (355° - 1.12 m/s at 31.7 m)

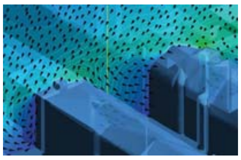

Figure 6. Turbulent kinetic energy (contours)
Velocity vectors (130° - 2.5 m/s at 31.7 m)

Relative Error (Fig. 7)

- Overall relative error is computed over all 6 levels in street canyon $r = \frac{|k_{meas} - k_{num}|}{|k_{meas}|}$
- (a) & (c): relative error for mean velocity approx. constant over average time interval variations
- (b) & (d): relative error for TKE average time range dependent

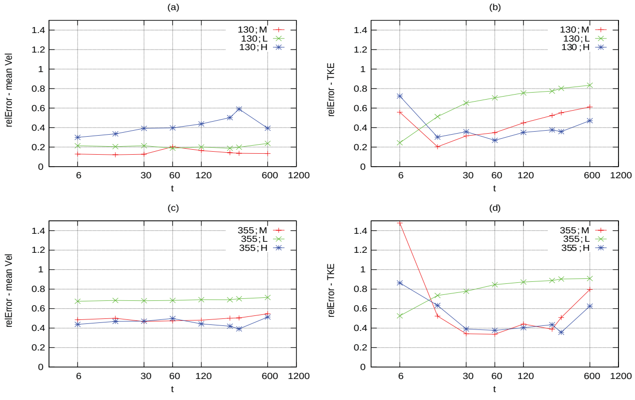

Figure 7. Overall rel error for mean velocity at 130° (a), 355°(c), rel error for TKE for 130° (b), 355° (d) for 3 different velocity magnitudes M = middle (1.5 m/s < V < 2.5m/s), L = low (V < 1.5 m/s), H = high (V > 2.5 m/s)

Conclusion

- Results show a) a strong dependence between average time intervals and TKE profiles within a street canyon and
  b) that the mean velocity part is only weakly influenced by the time average intervals
- Boundary conditions with constant TKE [1] lead to comparable results for TKE profiles of > 600 s averaged data, but to weaker correlations with corresponding mean velocity profiles
- Best results were found with intensity boundary conditions for the TKE (5%-10%) together with average time range of 15 - 60s for all studied conditions and over all levels in the street canyon
- The true TKE values in cities are difficult to determine due to problems in models and observations:
  1) observed TKE values are strongly dependent on averaging time scales, which can not be properly determined
  2) turbulence models are semi-empiric not, completely physically based

[1] Richards, P.J., Hoxey, R.P. (1993); Appropriate boundary conditions for computational wind engineering models using the k-e turbulence model; J. of Wind Engineering and Industrial Aerodynamics, 46 & 47; p. 145-153

Andres Gartmann
Institute of Meteorology, Climatology and Remote Sensing (MCR Lab)
Department of Environmental Sciences, University of Basel
Klingelbergstr. 27, CH-4056 Basel
Email: Andres.Gartmann@unibas.ch

17. Curriculum Vitae

Andres Gartmann
Date of Birth: 25 December 1980
Citizenship: Swiss (*Heimatort: Valendas GR*)

Education

2007 - present	Ph.D., Meteorology, Meteorology, Climatology and Remote Sensing (MCR), Department of Environmental Sciences, University of Basel, CH
1999 - 2006	Diploma in Mechanical Engineering, ETH Zurich, CH Diploma Thesis: *CFD Simulation of a Petcoke Reactor* Supervisors: Prof. Dr. A. Steinfeld, H. Friess Professorship of Alternative Energy Carriers Semester Thesis: *Simulation einer schwingenden Brücke mit MATLAB* Supervisors: Prof. Dr. P. Arbenz Professorship of Computational Science Semester Thesis: *Simulation of a Solzinc reactor* Supervisors: H. Friess Professorship of Alternative Energy Carriers
2000 - 2001	Earth Sciences (exchange year), University Basel, CH
1991 - 1999	Matura Typus B, *Gymnasium Leonhard*, Basel, CH

Related Work Experience

2008 - present	Head of Product Development, 50% meteoblue AG, Basel, CH
2007 - present	Assistant to *Einfürung in die Geoinformatik* (Dr. M.D. Müller) MCR Lab, University of Basel, CH
2007	Introduction to numerical urban CFD (three day course, leader) MCR Lab, University of Basel, CH
09/2007 - 09/2008	Project Scientist, 50% meteoblue AG, Basel, CH
09/2006 - 09/2007	Project Researcher MCR Lab, University of Basel, CH
05/2006 - 06/2006	Project Researcher, *CFX Simulation des PAC-Car II* ETH Zurich, CH
08/2003 - 04/2004	Freelancer, CFD Simulations Endress+Hauser Flowtec AG, Reinach BL, CH
1998 - 2006	Sales and technical PC-support The Portable Shop Schweiz AG / Dipl. Ing. Fust AG, Basel, CH

Publications

Gartmann A (2011): *Dynamik der urbanen CO_2-Verteilung-Teil 2: CFD-Simulationen in einer Strassenschlucht*, Regio Basiliensis, 52 (1), 45-54 Basel, Switzerland

Gartmann A, Fister W, Schwanghart W, Müller MD, (2011): *CFD modelling and validation of measured wind field data in a portable wind tunnel*, Aeolian Research, 3, 315-325

Gartmann A, Müller MD, Parlow E, Vogt R (2012): *Evaluation of numerical simulations of CO_2 transport in a city block with field measurements*, Environmental Fluid Mechanics, 12, 185-200